Interchange Turbulence in a Dipole-Confined Plasma

Brian Adam Grierson
Advisor Michael E. Mauel

Submitted in partial fulfillment of the
Requirements for the degree
of Doctor of Philosophy
in the Graduate School of Arts and Sciences

COLUMBIA UNIVERSITY

2009

Abstract

Interchange Turbulence in a Dipole-Confined Plasma

Brian Adam Grierson

Turbulence in fluids and plasmas is a complex phenomena which couples structures at different scales. Turbulent flows possess spectral cascades, as well as coherent structures. When a flowing system can be considered as two-dimensional, the coupling through nonlinear interaction generates large-scale structures which extend to the system size in an inverse energy cascade. Plasmas confined by the dipole magnetic configuration in the Collisionless Terrella Experiment (CTX) display two-dimensional, intense interchange-mode dynamics. The plasma fluctuations are driven by gas injection and microwave heating, which produces a plasma maintained near marginal stability. The turbulence in CTX is investigated with respect to both local and global measurements. When viewed locally, the intense fluctuations exhibit characteristics of fully developed turbulence, with a broad power-law spectrum and finite correlation length. When viewed globally, the dynamics are found to be describable by the chaotic temporal variation of a limited number of simple spatial modes. The fluctuation energy spectrum is calculated to be consistent with the power-law trends for the inverse energy cascade. Using analysis techniques for determining spectral energy flow, it is found that three-wave interaction transfers energy to low wavenumbers, as predicted for two-dimensional turbulence. A fully parallelized, self-consistent simulation including a conserving source and sink is used to test the model equations for interchange mode dynamics in a dipolar magnetic field. The model reproduces the driven fluctuations observed in CTX, producing the rotating, radially broad, large-scale structures.

Contents

List of Figures

Acknowledgements

I would like to gratefully acknowledge the support of my parents and brothers in the pursuit of this degree. They have all been an inspiration in my pursuit of higher education.

I would like to extend great thanks to Dave Maurer, Jeremy Hanson, and Matthew Worstell for their friendship and support, as well as making Columbia University's Plasma Lab one of the best work environments I have had the pleasure of knowing. I would also like to acknowledge the collaborative work with Hong Zhang of Argonne National Laboratory, and the collaboration with the LDX Team (Jay, Darren, Alex and Jen).

Most importantly, I would like thank my thesis advisor Michael Mauel. His limitless enthusiasm has inspired me throughout these years at Columbia. His conduct will always stand as a model of proper research.

My experience in the APAM department will always provide me with fond memories.

Chapter 1

Introduction

"I am an old man now, and when I die and go to heaven there are two matters on which I hope for enlightenment. One is quantum electrodynamics, and the other is the turbulent motion of fluids. And about the former I am rather optimistic."

-Sir Horace Lamb, Address to the British Association for the Advancement of Science (1932)

The turbulent motion of fluids has long been a challenge to fully describe from first principles. Turbulent flows are observable in everyday life; the flow of air over a car or an airplane, the transition from laminar to turbulent flow from a rising smoke plume, intense ocean currents, and most of the atmospheric circulation. Plasmas, which can also be describable by Navier-Stokes-like fluid theory, are another medium which display turbulent behavior remarkably similar to flowing fluids. These flows are comprised of multiscale interacting, circulating eddies. Thus turbulence in fluids and plasmas results from complex, nonlinear phenomena that couples structures at different scales. Understanding the spatial and temporal characteristics of the turbulent fluctuations remains a challenge that requires multiscale measurement, theory, and simulation. It is the study of a magnetically confined plasma exhibiting turbulent and chaotic behavior which is the focus of this thesis, with primary focus on the turbulent cascade process and the observation of quasi-coherent

structures. As well stated by Falkovich and Sreenivasan,

"Turbulent flows [have] allowed physicists to recognize and unambiguously express both the coexistence of correlated structure and randomness and the role of correlated structures in the transport of matter, heat and momentum" [29].

It is widely accepted that turbulence plays a significant role in transport, transport regulation, and generation of zonal flows [5, 25] in magnetized plasmas. Recent progress in the characterization and interpretation of plasma turbulence has been made through diagnostic improvements that allow observation of quasi-coherent structures and measurement of multipoint statistics of steady driven turbulence [24]. Progress has been especially rapid in certain types of strongly magnetized plasma and thin layers of fluid where the turbulent dynamics are nearly two-dimensional [83, 79]. Turbulence in two-dimensional systems is associated with an inverse energy cascade [51] that can generate self-organization at large scales and structures with long correlation lengths [36]. Quasi-two-dimensional turbulence appears in certain laboratory plasma devices [69, 76, 13], in the scrape-off-layers of toroidal fusion confinement devices [96], non-neutral plasmas [26], in the solar wind [80], earth's atmosphere [45] and in driven thin sheets of fluid [73].

1.1 Turbulence in Two-Dimensional Systems

In two-dimensions, the equation of motion is given by the incompressible Navier-Stokes equation. For a fluid with velocity $\mathbf{v}$ in the (x, y) plane,

$$\frac{D\mathbf{v}}{Dt} = \frac{\partial \mathbf{v}}{\partial t} + (\mathbf{v} \cdot \nabla)\mathbf{v} = -\frac{1}{\rho}\nabla p + \mathbf{f}_{ext} + \nu \nabla^2 \mathbf{v} \tag{1.1}$$

Taking the curl of this equation and eliminating $\hat{x}, \hat{y}$ (App.A), the equation for vorticity

$\omega = (\nabla \times \mathbf{v}) \cdot \hat{z}$ is obtained as

$$\frac{D\omega}{Dt} = \frac{\partial \omega}{\partial t} + (\mathbf{v} \cdot \nabla)\omega = g + \nu \nabla^2 \omega \tag{1.2}$$

If $g = (\nabla \times \mathbf{f}_{ext}) \cdot \hat{z} = 0$ and $\nu = 0$ then vorticity is conserved. In the inviscid velocity-vorticity formulation, mean energy $E = \langle \frac{1}{2} v^2 \rangle$ and enstrophy $Z = \langle \frac{1}{2} \omega^2 \rangle$ are conserved quantities, where $\langle \star \rangle = \int \star d^2\mathbf{x}$. Plasmas admit the same formulation, where the vorticity ω is also the Laplacian of the stream function, $\nabla^2 \Sigma$ [36, 41, 21]. Non-neutral plasmas are isomorphic to the Euler equations [26], inviscid Navier-Stokes flow, where the electron density is identically the charge density and serves as a proxy for vorticity. For a comprehensive review of two-dimensional turbulence, see Tabeling's monograph "Two-dimensional turbulence: a physicist approach" [83].

The turbulence that occurs in two-dimensional systems is markedly different from three-dimensional turbulence. Originally investigated as a simplification of 3D turbulence, it was found that 2D turbulent systems exhibit unique properties in direct contrast to 3D. It is well known that 3D fluid turbulence cascades energy to higher wavenumbers (smaller physical scales) in a *forward energy cascade* [54]. Energy is put into the system at the injection scale k_i, where it is transferred to higher wavenumbers until it reaches the *dissipation scale* k_d, usually a viscous dissipation scale. The energy cascade obeys a $k^{-5/3}$ power-law between the injection scale and the dissipation scale in the *inertial range* $k_i < k < k_d$. This can be seen by taking the kinetic energy $v^2 = \int S(k) dk$ in the inertial range as a function of wavenumber and dissipation rate ϵ, neglecting the viscosity ν which only affects the spectrum in the dissipation range. Thus the units of wavenumber spectrum are m^3/s^2. The units of ϵ are m^2/s^3. Therefore by dimensional arguments, for $S = S(k, \epsilon)$, the energy wavenumber spectrum must obey $S = A\epsilon^{2/3} k^{-5/3}$.

When the fluid is 2D, there are two conserved quantities: energy and enstrophy (mean-squared vorticity). The conservation of energy and enstrophy results in a *forward* enstrophy

cascade to higher k, and an *inverse* energy cascade to lower k [51]. For wavenumbers larger than the injection scale, the enstrophy is transferred to higher wavenumbers towards the enstrophy dissipation scale obeying a k^{-3} power-law. Below the injection scale, the energy is transferred to lower wavenumbers with a $k^{-5/3}$ power-law like the 3D case, but the energy flows in the opposite direction into large-scale structures (Fig.1.1).

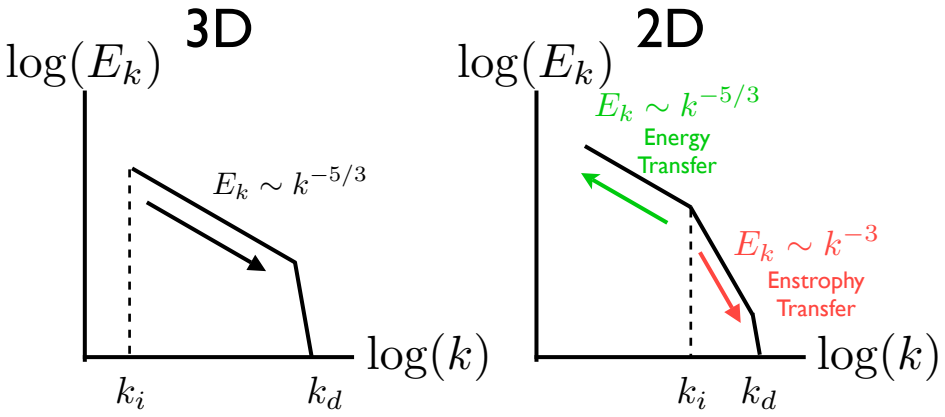

Figure 1.1: The spectral trends of energy for 3D and 2D turbulence.

When energy and enstrophy are conserved quantities, the direction of energy and enstrophy transfer can be seen by injecting energy into an arbitrary wavenumber k_2, where $k_2 = 2k_1$ and $k_3 = 3k_1$. This process can be illustrated schematically in Fig.1.2. Using $\delta E = E(k, t_2) - E(k, t_1)$ the conservation is posed as

$$\begin{aligned} \delta E_1 + \delta E_2 + \delta E_3 &= 0 \\ k_1^2 \delta E_1 + k_2^2 \delta E_2 + k_3^2 \delta E_3 &= 0 \end{aligned}$$

Solving the conservation system of two equations in three unknowns for the higher and lower wavenumber energy and enstrophy,

$$\begin{aligned} \delta E_1 &= -\frac{5}{8}\delta E_2 & \delta E_3 &= -\frac{3}{8}\delta E_2 \\ k_1^2 \delta E_1 &= -\frac{5}{32} k_2^2 \delta E_2 & k_3^2 \delta E_3 &= -\frac{27}{32} k_2^3 \delta E_2 \end{aligned}$$

Therefore net energy goes to lower wavenumbers ($\delta E_1/\delta E_3 > 1$) and net enstrophy goes to higher wavenumber ($k_3^2\delta E_3/k_1^2\delta E_1 > 1$).

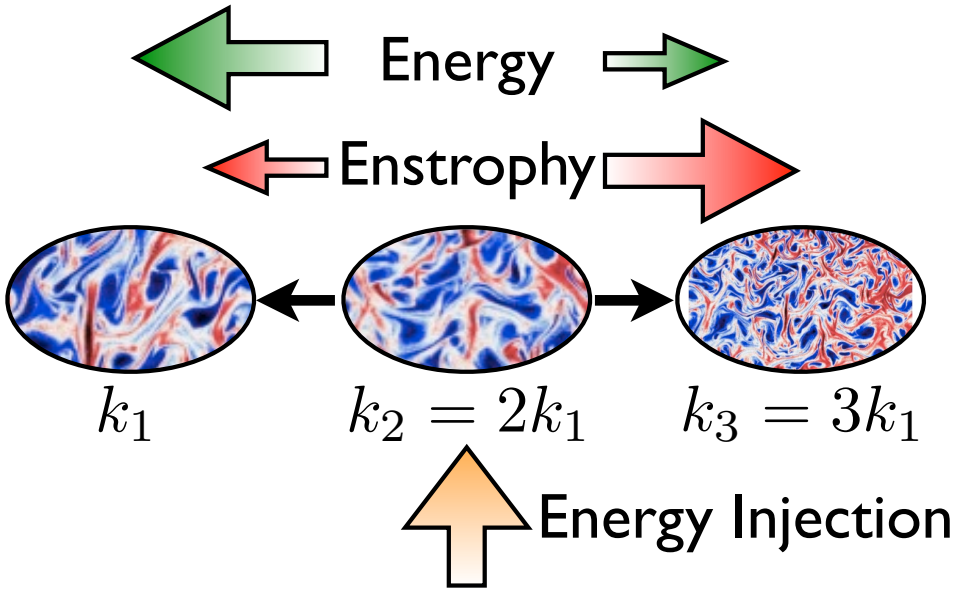

Figure 1.2: The transfer of energy and enstrophy in 2D turbulence

1.2 Turbulence in Laboratory Magnetized Plasmas

The bulk of research in laboratory plasma turbulence has been the study of drift-wave turbulence in linear plasma devices and fusion reactor tokamak configurations. Drift wave turbulence is believed to be responsible for the cross-field transport of particles and heat, which can degrade the plasma confinement in a tokamak. The generation of 'zonal flows' inside the last closed flux-surface in a tokamak can form transport barriers, enhancing the confinement of the device. An extensive review of zonal flows is given by Diamond, *et. al.* [25]. The term 'zonal flow' originates in the meteorological sciences describing the primarily west-to-east flow pattern in the Earth's latitude lines. The zonal flows in plasmas, occurring primarily in the poloidal direction, decorrelate radial structures called 'streamers' by an $\mathbf{E} \times \mathbf{B}$ shearing mechanism. This is phenomenologically similar to the

lack of extreme weather in the zonal flow bands of earth, where large cyclones are less likely to form because of high wind velocities and flow shear. Because these streamers facilitate high levels of heat and particle transport, it is the destruction of streamers which is believed to cause the transition from the low (L) to high (H) confinement mode of modern tokamaks: the aptly named H-mode operating regime. Displayed in Fig.1.3 are a series of zonal flow regions on the outboard side of a tokamak which are suppressing the radially elongated streamer structures (displayed in red and blue) [53]. The generation of zonal

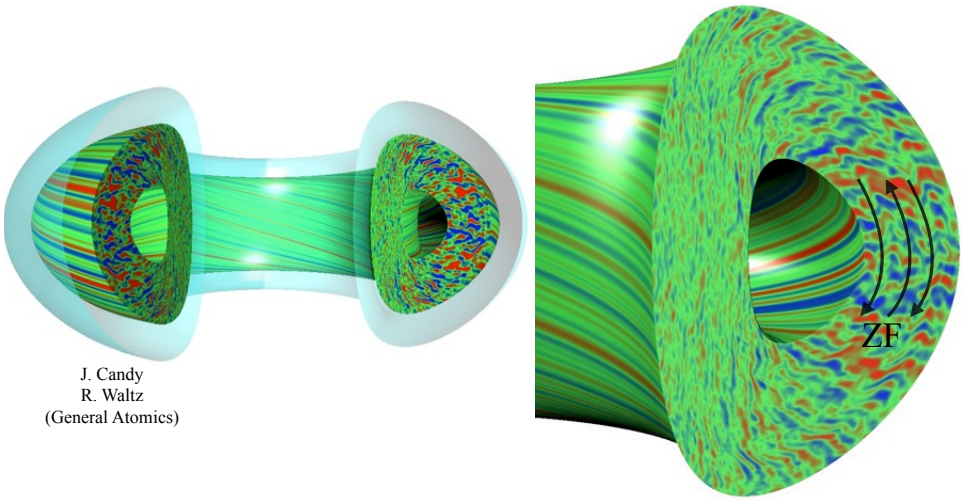

Figure 1.3: Visualization of the simulation GYRO displaying zonal flows on the outboard side of a tokamak

flows in plasmas is an active area of laboratory research, and extensive experimentation is being carried out to understand how these shearing zonal flows are generated. Zonal flow generation is primarily attributed to the Reynolds stress, which arises due to the random fluctuations in fluid momentum, and causes transport of momentum [85]. The origin of the shear flow is not entirely clear, but has an atmospheric analogy in Rossby waves [37], which emerge when there is shear in rotating fluids and observed in the atmosphere. It is also observed that zonal flow generation coincides with increases in quadratically nonlinear, three-wave interactions [13]. It is the three wave interaction and power transfer from spectral pumping at high wavenumber which may lead to the self-organized state of plasma drift-

wave turbulence [39, 86]. Recent measurements in laboratory drift wave turbulence displays the two-dimensional dual cascade, which generates large-scale structures [61, 60]. The forward enstrophy cascade is measured by density fluctuations, where both the density and vorticity fluctuations are assumed to be advected as passive scalars [14]. At the plasma edge, outside of the last closed flux surface, the plasma does not benefit from the stability of good average magnetic curvature because the field-lines intersect the diverter or confining vessel. In this region, the fluctuations take on a flute-mode, or interchange-like character. At the tokamak plasma edge, large amounts of plasma can be ejected towards the vessel wall by edge-localized modes (ELMs), relaxing the transport barrier, and causing intermittent transport events (ITEs) which can damage the material vessel. These large, coherent density perturbations (called 'blobs') are transported radially by a dipolar potential structure 90° out of phase with a density perturbation causing $\mathbf{E} \times \mathbf{B}$ motion.

As an innovative concept for a fusion reactor, the Levitated Dipole Experiment [47] located at MIT is a new investigation in to plasma confinement at high $\beta = p/(B^2/2\mu_0)$. The high β value represents good utilization of the magnetic field to contain the plasma pressure. Because the dipole magnet is levitated, the magnetic field-lines are closed and the plasma does not suffer from field-aligned losses, improving confinement. The potential tends to be constant along a field-line, so it can only vary radially and azimuthally. When the pressure gradient is marginally stable to interchange modes, convective cell generation can occur and lead to transport of particles, but not energy [46]. Because of the significant compression and expansion associated with the interchange motion, hot plasma will cool as it is transported radially outwards, and be heated as it is moved inwards. If convective cells are generated in LDX, they can serve as a means of fueling.

The laboratory dipoles of CTX and LDX thus provide a simple magnetic geometry inside a large containing vacuum vessel. The large plasma volume allows excellent diagnostic access for local and global measurement of plasma parameters and profiles.

1.2.1 Nonlinear Dynamics

Finding renewed interest in the plasma physics community is a different viewpoint on the turbulent fluctuations in plasmas: the nonlinear beating of a limited number of modes [84, 25, 92]. It has been shown in the past that the period-doubling route to chaos can produce turbulent phenomena in simple gas discharges, possessing a broad power-law potential fluctuation frequency spectrum and features describable by simple nonlinear oscillator models [50]. Reduced models of convecton such as the Lorenz model [59] display chaos of a low dimensionality. Observation of low dimensioinal chaos of vortices in plasmas has been proposed [77] and observed in laboratory devices [17, 95]. Theoretical work and review on vortex dynamics and chaos is presented by Aref [2], and a review of chaotic systems in [81]. The power-law spectra of turbulent fluctuations in plasmas are suggestive of such grand themes as self-similarity and self-organized criticality in nature [4].

1.3 The Interchange Instability in a Magnetic Dipole

Instabilities which can drive turbulent fluctuations are present in plasmas with non-uniformities in pressure and/or magnetic field. In CTX, the dominant instability is the electrostatic interchange instability [74], possessing a parallel wavenumber that is essentially zero ($\mathbf{k} \cdot \mathbf{B} = k_{\|} = 0$).

When treated as an initial-value problem, the textbook interchange instability is the plasma equivalent of the gravitational Rayleigh-Taylor instability where a heavy fluid is supported by a light fluid (Fig.1.4). In the gravitational case, instability occurs when the pressure gradient and gravity have anti-parallel components $\nabla p \cdot \mathbf{g} < 0$. Gravity is seldom of importance in the motion of plasmas created in the laboratory, but the outward magnetic curvature force from bent field-lines ($\mathbf{F}_\kappa = m v_{\|} / R_c \hat{r}$) where $\mathbf{R}_c$ is the radius of curvature vector, magnetic gradients ($\mathbf{F}_{\nabla B} = -\mu \nabla B$) where $\mu = m v_\perp^2 / 2B$ [31] and the outward centrifugal force resulting from rotation ($\mathbf{F}_\Omega = -\rho \mathbf{\Omega} \times (\mathbf{\Omega} \times \mathbf{r})$) where $\mathbf{\Omega}$ is the

angular frequency [57, 58, 55] provide effective forces that act in a similar way. The plasma equivalent to the gravitational instability occurs when the pressure gradient and magnetic radius of curvature vector have anti-parallel components $\nabla p \cdot \mathbf{R}_c < 0$, where the magnetic field is concave towards the plasma. This is known as "bad curvature" [31]. A perturbation of a plasma-vacuum interface or perturbations of an isobar can cause electrons and ions to ∇B counter-drift[1] to establish a perturbed electric field (Fig.1.4 right). The perturbed electric field causes a $\mathbf{E} \times \mathbf{B}$ drift of the plasma, amplifying the initial perturbation. From linear theory, pressure driven interchange modes are unstable for a pressure profile which varies more rapidly than $p \sim L^{-4\gamma}$ ($\gamma \approx 5/3$ is the MHD ratio of specific heat) because the flux tube volume expands as $V \sim L^4$. The parameter L is used to indicate equatorial radius. Centrifugally-driven interchange modes are unstable for $\partial N/\partial \psi > 0$ where ψ is the magnetic flux and N is the particle number per unit flux [58]. In a uniformly magnetized cylinder, this is a radial density profile with any gradient, but in a magnetic dipole this is equivalent to a density profile steeper than $n(L) \sim 1/L^4$. The stability of a finite gradient occurs because of the compression of flux-tubes associated with the interchange motion. The Earth's plasmasphere density profile is variable, but generally follows an exponential profile inside the plasmapause, and an invariant region outside of the plasmapause [15].

While the instabilities previously studied in CTX could be modeled as quasi-periodic bursts of Rayleigh-Taylor instability, the "high density regime" of a dipole confined plasma's quasi-steady convective driven interchange motion may be modeled as the plasma equivalent of driven Rayleigh-Bernard convection [77]. In Rayleigh-Bernard convection, a fluid is heated from below with gravity pointing downward (Fig.1.5). As a result of the heating, the fluid becomes lighter on the bottom, resulting in antiparallel gravity and density gradient vectors. If the temperature gradient is strong enough to overcome viscosity and thermal diffusivity limitations, driven convective motion occurs. In a plasma, a driven pressure gradient from heating and magnetic radius of curvature vector provide analogs to the driven

[1] The combination of a magnetic field gradient and magnetic curvature results in a drift velocity $v = \frac{1}{qR_c^2B^2}(2W_\parallel + W_\perp)\mathbf{R}_c \times \mathbf{B}$ where $W_\parallel, W_\perp = mv_\parallel^2/2$ and $mv_\perp^2/2$ respectively.

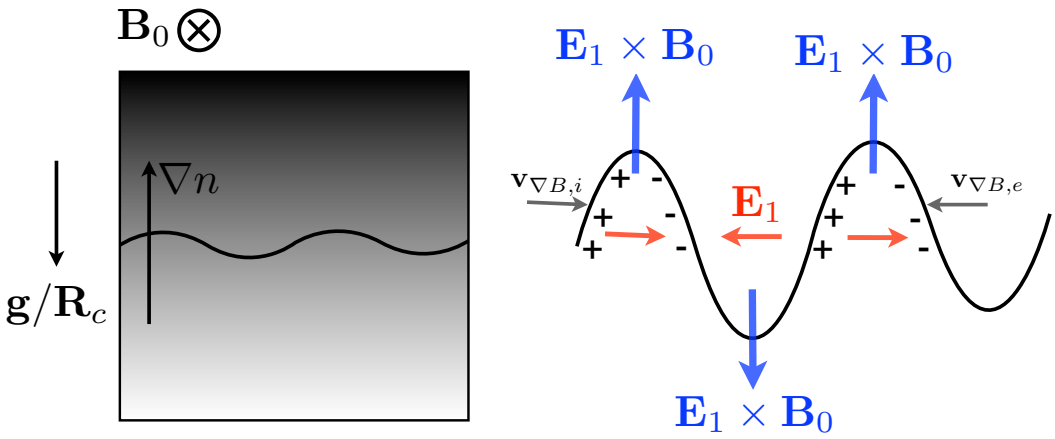

Figure 1.4: The equivalent of a Rayleigh-Taylor instability in a plasma. A perturbation of the plasma boundary grows with the positive feedback provided by $\mathbf{E}_1 \times \mathbf{B}_0$.

density gradient and gravity vector.

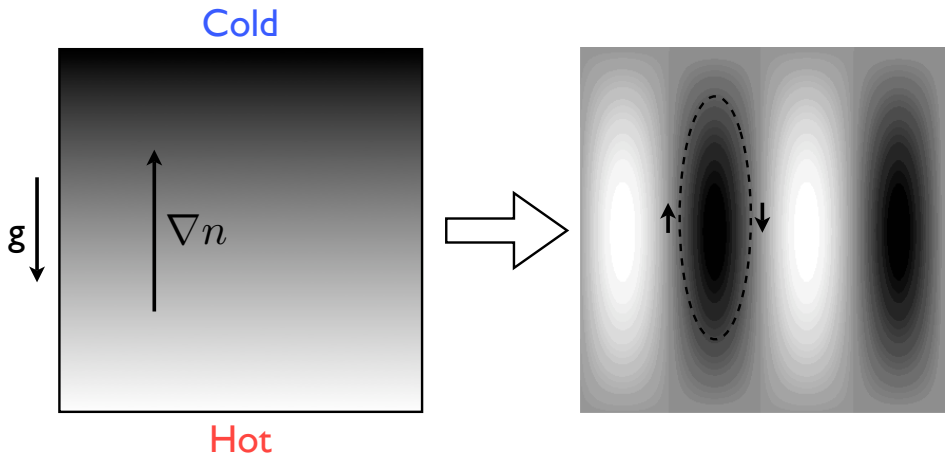

Figure 1.5: The physical configuration for exciting Rayleigh-Bernard convection in a fluid.

Drift instabilities, also called the universal instability, can exist as well. Drift instabilities do not require magnetic curvature forces to be present, but only a pressure or density gradient with a finite $k_\parallel$ for potential (non-zero parallel electric field). These drift instabilities are expected to be sub-dominant to interchange instabilities in CTX because of the strong shear-free confining field, and no experimental evidence has been shown to the contrary. Drift modes tend to saturate near the drift scale [40, 38] with $k_\perp \rho_S \leq 1$ where $\rho_S = C_S/\Omega_c$, $C_S =$

$\sqrt{T_e/m_i}$ and Ω_c is the ion cyclotron frequency. Drift modes, because of their slower growth rates, tend to have density fluctuations levels lower than interchange fluctuations [12, 38], although fluctuation levels can be high ($\tilde{n}/n_0 \leq 40$ %) near shear-flow regions or strong pressure gradients [13].

The instabilities previously investigated in CTX were the hot electron interchange (HEI) instability [65, 64, 56, 63, 62, 55] and the centrifugal instability [55, 57, 58]. The first was an interchange instability driven by hot electron pressure, and caused periodic 'bursts' of broadband fluctuations which 'chirped' in frequency and saturated nonlinearly [11]. These bursts can be modeled as an unstable initial value problem, with growing fluctuations which increased in frequency, occurring approximately every 1 ms. The centrifugal instability was driven by rapid, near-sonic rotation of the plasma, created by radial currents between the plasma boundaries. Centrifugal modes grow faster for higher azimuthal mode numbers than the HEI modes, but with much lower amplitudes [58].

The plasmas investigated in this thesis have higher densities, and differ substantially from plasmas dominated by HEI modes. When the HEI instability is suppressed by increased neutral gas fueling, the density rises by more than an order of magnitude to $n_0 \approx 10^{16}$ m^{-3}, and the fluctuations become characteristic of quasi-steady driven turbulence. No quasi-periodic bursts of hot electrons have been observed in this high density regime. The spectral trends of density and potential exhibit power-law slopes of $f^{-\alpha}$. These plasmas possess large amplitude fluctuations in density $\delta n/n_0 \sim 50\%$ and potential $e\tilde{\Phi}/T_e \sim 50\%$, and are dominated by large structures in the plasma. Large relative fluctuation amplitude and large structure size are characteristic of interchange-like fluctuations in tokamak SOL edge turbulence as well, where the plasma does not benefit from good average magnetic curvature [3].

In the assertion of the electrostatic nature of the turbulent fluctuations, one criteria to be met is the low beta case $\beta \ll m_e/m_i$, where $\beta = p/(B^2/2\mu_0)$, or $v_{Te} \ll v_A$ where v_{Te} is the electron thermal velocity and v_A is the Alfvèn velocity [34]. This criteria is not

strictly met only where the magnetic field is weakest at the equatorial plane, where it is violated by a factor of two. The electrostatic approximation is nevertheless appropriate because in the magnetic dipole geometry, the interchange instability always dominates over ballooning instabilities which perturb the confining field [33]. Furthermore, the previous experimental and computational studies of fluctuations in dipole-confined plasmas were very well described by electrostatic models in both the linear and nonlinear regimes, even though the fluctuation frequencies and betas of those plasma discharges were much higher than in the experiments in this thesis.

The magnetic dipole configuration presents a strong mirror effect to confined particles. Because the fluctuations investigated in this thesis are low frequency ($\omega \ll \Omega_i, \omega_b$) the plasma can be considered a two-dimensional system obeying the MHD equations and conserving μ and J [16]. This assumption has been shown to be accurate even for fluctuations above the ion cyclotron frequency when the basic plasma quantities are represented in a 'bounce-averaged' sense [65]. In these cases, plasma fluctuations are resonant with hot drifting particles produced by ECRH, and these fluctuations can can exceed 3 MHz.

While a fluctuation spectrum with power-law of $k^{-\alpha}$ is certainly suggestive of turbulent or chaotic processes, rigorous investigation into the correlation time and length of fluctuating plasma quantities, spectral trends, chaotic dynamics, and nonlinear mode coupling are necessary to fully understand the nature of the turbulence.

1.4 Organization

The organization of this thesis will be as follows:

In Ch.2, I will describe the experimental apparatus for investigation of dipole-confined turbulent plasmas and the basic plasma parameters and profiles. All experiments are carried out in the Collisionless Terrella Experiment at Columbia University's Plasma Physics Laboratory. The experimental apparatus, magnetic geometry, and available diagnostics will

be reviewed. Diagnostic upgrades of a fast camera, triple probe, and new amplifiers for the global polar imaging diagnostic will be described in detail. The basic plasma discharge time series and profiles of basic plasma parameters will be provided.

In Ch.3, signal analysis techniques for turbulent and chaotic fluctuations will be described. Conventions for interpreting the results from the signal analysis methods will be determined, and the qualitative and quantitative implications of these methods will be outlined. Verification and validation of the more sophisticated analysis tools will be tested on model data.

In Ch.4, comprehensive measurements of dipole-confined plasma turbulence will be presented. Investigations into the local characteristics of plasma fluctuations are performed by single probe diagnostics measuring density and potential. The global density profile and fluctuations are observed by the polar imaging diagnostic and fast camera, and the global potential structure is computed by inverting the continuity equation for plasma density. The fluctuation energy spectrum and results from quadratic nonlinear coupling analysis will be presented.

A numerical simulation for testing the model equations in the magnetic dipole geometry has been developed and the results will be detailed in Ch.5. The parallelization of the simulation code and performance results will be provided. The development of a global Fast Poisson Solver in collaboration with the MCS division of Argonne National Laboratory will be described in detail. A conserving source and sink of ion density, electron distribution function and electron energy is used to achieve a steady, driven turbulent state. Using analysis techniques developed in Ch.3, comparisons between laboratory observation and simulation results will be presented.

Chapter 2

The CTX Device

The CTX device is a mechanically supported dipole electromagnet in a 1.4 m diameter aluminum vacuum vessel. Vacuum from atmospheric pressure is achieved by a mechanical roughing pump followed by turbo molecular pumping to a pressure of $p \approx 1 \times 10^{-6}$ Torr. Once this base pressure is reached, a cryogenic pump is used to maintain a base pressure of $p \approx 1.7 \times 10^{-7}$ Torr for all experimental conditions. Plasma production is achieved through electron cyclotron resonance heating (ECRH) of 1 kW at 2.45 GHz. Neutral hydrogen is puffed into the vacuum chamber through a piezo-electric valve, typically in 1-10 μs intervals to achieve the desired plasma density.

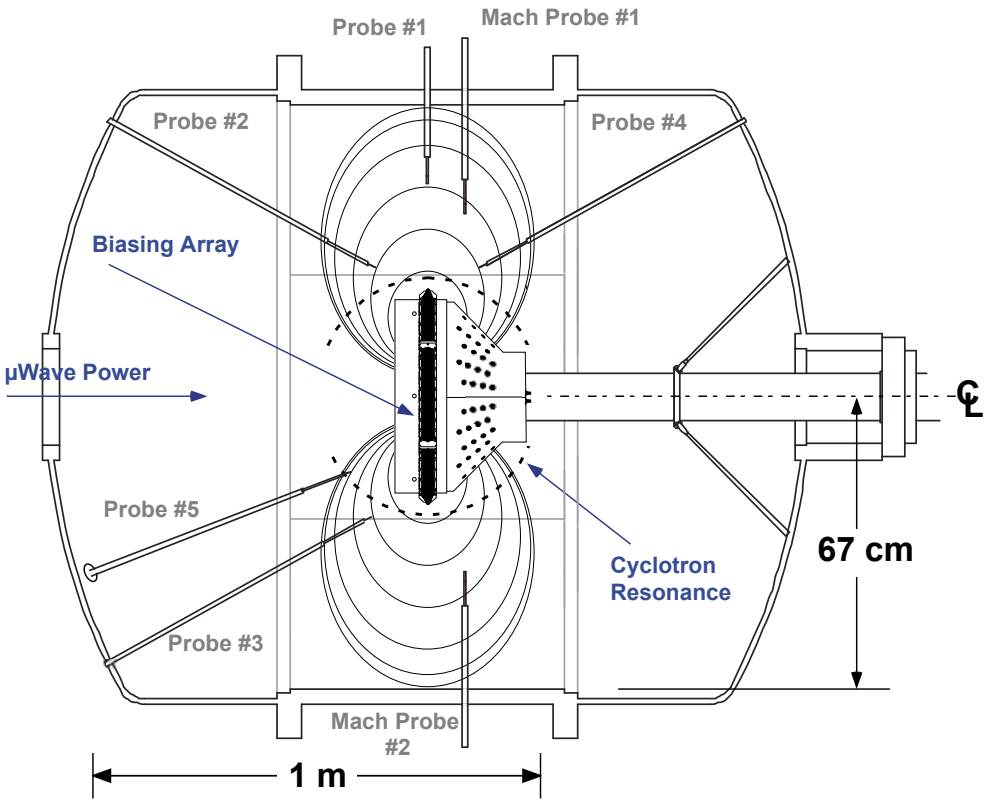

Figure 2.1: The CTX Device is a mechanically supported dipole magnet inside a vacuum vessel.

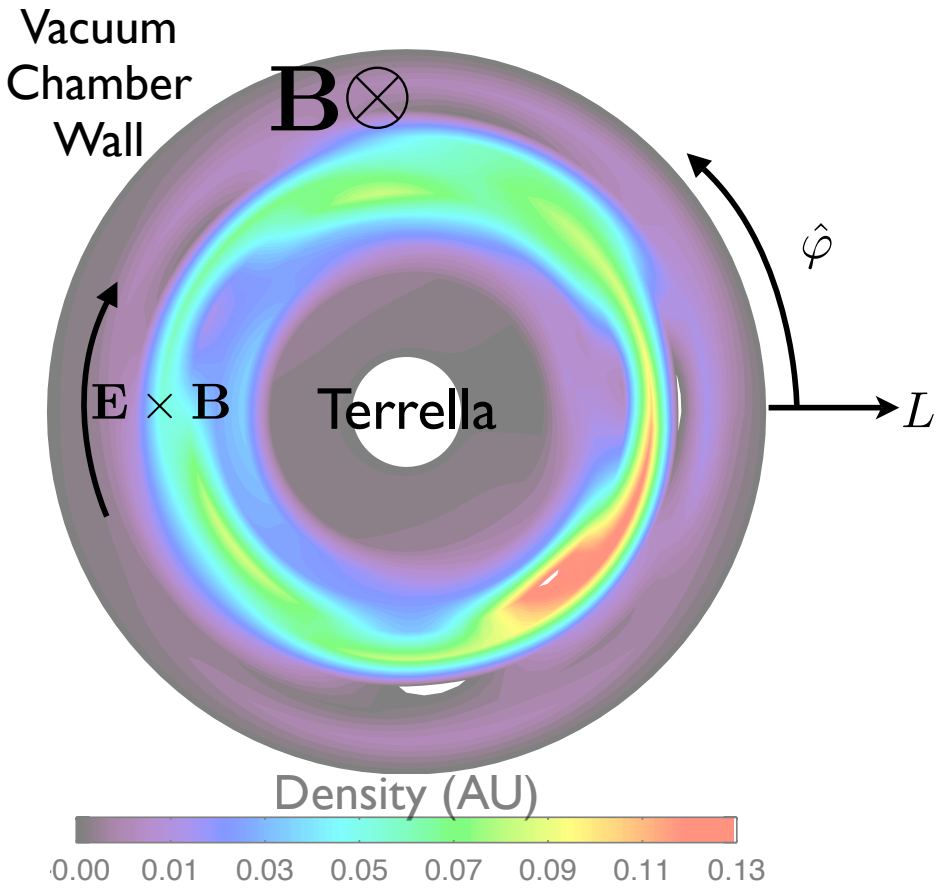

Figure 2.2: Equatorial plane of a confined plasma in a magnetic dipole. The major radius is parameterized by L when referring to equatorial values. The plasma rotation is observed to be in the $-\hat{\varphi}$ direction. (False radial spacing for illustrative purposes)

2.1 The CTX Magnetic Dipole

The CTX magnetic field can be well described by the ideal dipole approximation [55]. The ideal magnetic dipole field can be expressed in Clebsch coordinates as

$$\mathbf{B} = \nabla\varphi \times \nabla\psi = \nabla\chi \tag{2.1}$$

where $\mathbf{B}$ is the vector magnetic field, φ is the azimuthal angle, ψ is the magnetic flux, and χ is the magnetic scalar potential. In spherical coordinates, this axisymmetric field, magnetic flux and magnetic scalar potential can be written as

$$B(r,\theta) = \frac{M}{r^3}\sqrt{1+3\cos^2\theta} \quad \psi(r,\theta) = \frac{M}{r}\sin^2\theta \quad \chi = \mathbf{M}\cdot\nabla\frac{1}{r} = \frac{M}{r^2}\cos\theta \tag{2.2}$$

Quantities are often quoted in terms of equatorial radius L, where $\theta = \pi/2$. In CTX, $\mathbf{M} = B_0 L_0^3 \hat{z}$, $B_0 \approx 0.0875$ T (875 Gauss). This is the field strength at the ECRH resonance resonance for 2.45 GHz occurring at the equatorial radius of $L \approx 0.27$ m, giving $M = 0.00172$ Tm^3.

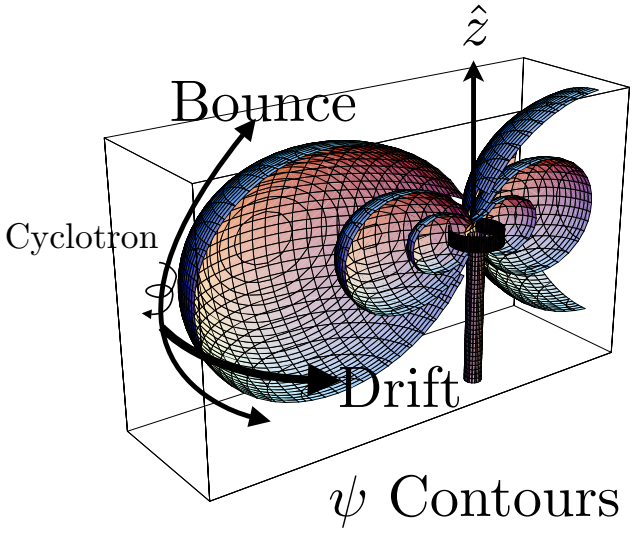

Figure 2.3: Contours of ψ=constant. Particle motion is separated into cyclotron, bounce, and drift.

There are three particle motions in the vacuum magnetic field configuration: cyclotron, bounce, and drift each with their own characteristic frequency $\omega_c \gg \omega_b \gg \omega_d$, and their own adiabatic invariant μ, J, ψ, respectively. For the third invariant, $E_\perp$ is the perpendicular energy of the particle, and the integral encloses a drift path around the dipole. The cyclotron frequencies for electrons and Hydrogen ions have been calculated and are shown in Fig. 2.5.

$$\omega_c = \frac{|q|B}{m} \qquad \mu = \frac{mv_\perp^2}{2B} \tag{2.3}$$

$$\omega_b = 2\pi\left(\int \frac{ds}{v_\parallel}\right)^{-1} \qquad J = \int_a^b mv_\parallel ds \tag{2.4}$$

$$\mathbf{u}_d = \frac{\mu}{q}\frac{\nabla B \times \mathbf{B}}{B^2} \qquad \psi = \oint mE_\perp d\varphi \tag{2.5}$$

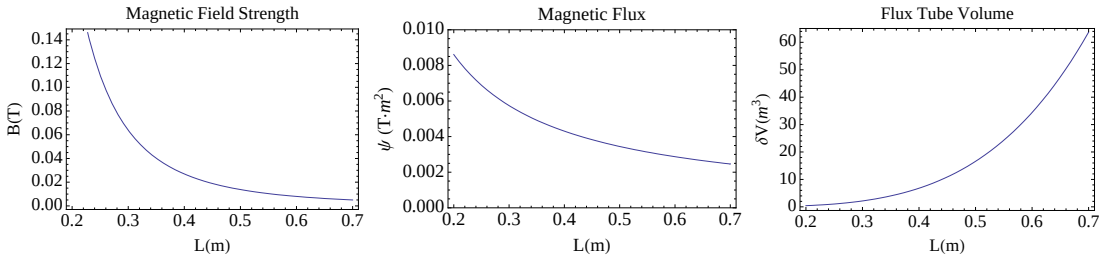

Figure 2.4: Magnetic field strength, magnetic flux and flux-tube volume per unit flux ($\delta V = \int d\chi / B^2$) as a function of L, the radial distance along the equatorial midplane of CTX.

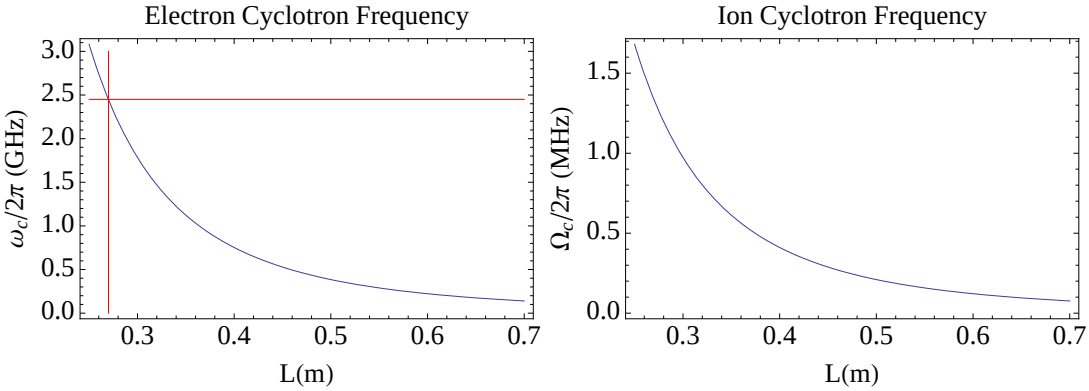

Figure 2.5: Electron and ion cyclotron frequencies in CTX on the equatorial midplane.

2.2 The Diagnostic Set

Plasma diagnostics are the means by which basic plasma parameters are measured either directly (*e.g.* probes, energy analyzers), or indirectly (*e.g.* photodiodes, fast cameras, x-ray emission). CTX is outfitted with a wide spectrum of diagnostics to measure neutral pressure, microwave forward and reflected power, density, potential, x-ray emission (hard and soft), visible light (photodiodes, fast camera), particle flux, polar current and mach number for flow measurements.

2.2.1 Basic Diagnostics

Neutral Pressure

The neutral pressure in CTX is measured by an ionization gauge. The current from the ion gauge is calibrated for Hydrogen, and stored in the data tree.

X-ray

ECRH creates high energy electrons which produce X-rays. In low density plasmas, electrons above the keV range produce hard x-rays by bremsstrahlung with cold ions or neutrals. In the high density operating regime, the plasma is more thermalized, and the production of such high energy electrons is reduced, indicated by a drop in the measured X-ray emission. In the high density regime, the soft X-ray emission from less energetic electron bremsstrahlung is observed to increase.

Photodiodes

A pair of photodiodes are used to measure the visible light intensity for high density discharges. In the high density, turbulent regime there is sufficient visible light for the

photodiode pair. The visible light signal from a plasma source [97] is given by

$$S \sim n_n f_p(n_e, T_e) A_{pq} \tag{2.6}$$

where n_n is the neutral density, f is the electron distribution function, and A_{pq} is the radiative decay rate for of the p to q transition. The neutral density is approximately constant over the timescale of fluctuations, therefore fluctuations in light intensity should follow fluctuations in density and temperature. The magnitude of visible light intensity should be proportional to neutral pressure in CTX, and this has been see experimentally (Fig.2.13). In addition, the fluctuations in visible light intensity has been correlated with fluctuations in plasma density, and the maximum correlation is found (Fig.4.17) at zero time-lag. This indicates that visible light measurements can serve as a proxy for density fluctuations.

2.2.2 Probes

Floating Potential Probes

CTX is outfitted with a number of high-impedance floating potential probes. These probes are stainless-steel wire tips with 100 kΩ resistors near the probe tip. Each probe tip is connected to a co-axial cable and run to amplifiers. The signal from the floating potential probes is digitized at rates up to 10 MHz with LeCroy TR6841 transient recorders.

The Single-Electrode Langmuir Probe

The Langmuir probe in CTX is a flat square I_{sat} probe (See B.1, B.2) with area $A = 1$ cm^2. This Langmuir probe is biased at $V_b = -100$ V $\gg T_e/e$ for the bulk electron temperature of $T_e < 10$ eV. The bias is applied through a battery pack coupled with a 0.1 μF capacitor in parallel for fast response.

Installation of New Triple Probe

A new triple probe array (See B.3, B.4) has been installed on CTX and is used to measure the edge plasma parameters of floating potential, temperature, and density (Fig.2.6). The array consists of three triple probes with radial separation of 2.54 cm between the probe sets. There is a 0.45 cm separation between the individual probe tips, which is a few times the electron Debye length $\lambda_{De} \approx 1$ mm.. The triple probe array is inserted into the CTX vacuum chamber at the equatorial midplane and is systematically adjusted to take measurements across the edge plasma radius.

The triple probe is wired with a large 10 MΩ resistor for accurately measuring the floating potential, and a 180 V supply to collect ion saturation current Fig.2.7. All of the signals are transmitted through voltage dividers to reduce the amplitude to ±5 V.

$$V_{out} = V_{in} \frac{R_2}{R_1 + R_2} \tag{2.7}$$

where R_1 is the larger resistor. The signal from the probe measuring the floating potential is then amplified because of its low signal level.

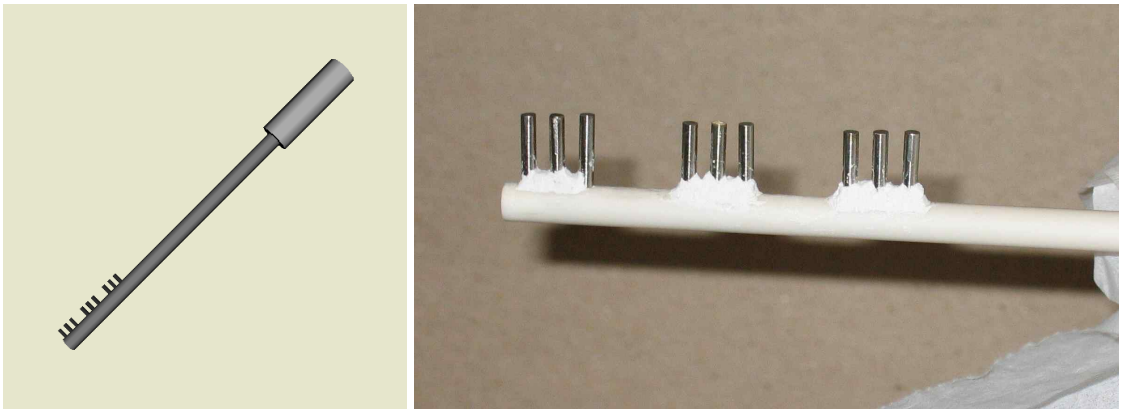

Figure 2.6: A rendering and photograph of the triple probe array installed on CTX. The array consists of three triple probes with radial separation of 2.54 cm between the probe sets. There is a 0.45 cm separation between the individual probe tips.

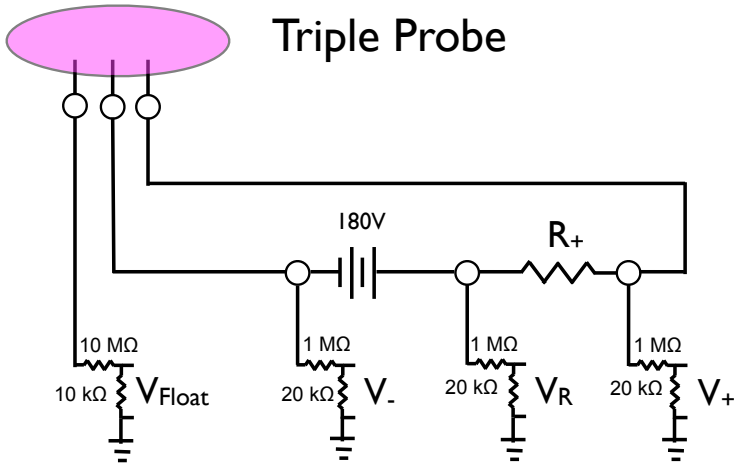

Figure 2.7: The circuit for the triple probe installed on CTX. The output from the voltage divider providing V_{Float} is then amplified before being digitized.

2.2.3 Polar Imager

The "polar imager" (Fig. 2.8) is a unique array of 96 gridded particle detectors situated at the pole of the CTX dipole magnet. The detectors are arranged uniformly in the natural magnetic flux coordinates (φ, ψ). All detectors exist at $B \approx 2$ kG, where the gyro-radius of like particles will be the same regardless of which aperature they enter. The magnetic field at the aperture of each detector is approximately the same, thus collecting current from flux tubes of equal magnetic flux. The flux tube volume $\delta V = \int d\chi / B^2 \propto L^4$ increases dramatically with increasing radius: detectors at larger radii see a much larger flux tube volume. The magnetic cap of the polar imager diagnostic is stainless steel plasma spray-coated with 12 mil thick of alumina. The spray-coated insulator prevents currents from flowing along the field lines to the magnet cap itself. Each gridded particle detector (retarding field energy analyzer) has a 1 cm^2 aperture with a series of individually biased stainless steel meshes between the aperture and the stainless steel collector plate. There are three grids used to repel electrons, ions, and a grid biased (-9 V) to suppress secondary electrons emission from the collector plate. The individual meshes can be biased to repel either electrons, ions, or both. When the detectors are un-biased the parallel current being collected is a good

approximation to the flux-tube integrated electron distribution function, F, by measuring the electron flux to the poles due to electron-neutral collisions. The net current in un-biased operation is negative, and increases in magnitude with increased fueling. Upon application of small negative bias ($|V_{bias}| < 50$ V) to the electron repeller grid, the magnitude of the polar current decreases while remaining negative. The application of voltages to the gridded polar detectors can select which species is collected, as well as determine the parallel energy of the collected species.

When viewing of the plasma density is desired, the electron grid is biased sufficiently negative to repel electrons, effectively detecting flux-tube integrated ion saturation current, $I_{polar} \propto N$. When biasing sufficiently negatively ($V_{bias} \approx -100$ V), the net polar current changes sign, becoming positive.

$$n \propto \frac{I_{polar}}{\delta V} \tag{2.8}$$

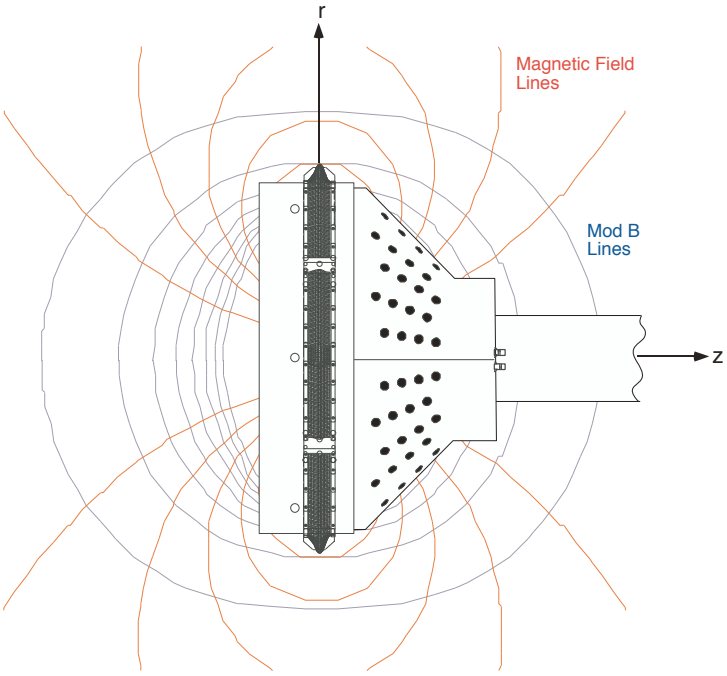

Figure 2.8: The polar imager diagnostic.

Installation of New Amplifiers

The polar imager collects a current proportional to the flux tube integrated density, and in the turbulent regime this current increases by an order of magnitude. To view the global structure and temporal variation of plasma fluctuations in the high density regime, new low-gain transimpedance amplifiers have been developed and installed on CTX to convert the collected current into a voltage. This voltage signal is recorded by Aurora A14 Module digitizers (14 bit, 128 ks/record) at rates up to 1 MHz. The amplifiers used in the low density regime are 2 MΩ transimpedance amplifiers ($|I_{polar}| < .25\ \mu$A), while the high density amplifiers have a 51 kΩ transimpedance ($|I_{polar}| < 100\ \mu$A). The field-aligned current increases by a factor of 400 from the low to high density regime, necessitating the production of low-gain amplifiers. This can be seen in Fig.2.9 where the increase in plasma density causes the polar detectors to become completely saturated. These new low-gain amplifiers allow imaging of the plasma whether the grids are biased or unbiased. When the grids are unbiased, the collected current is larger than when repelling electrons (Fig.2.10).

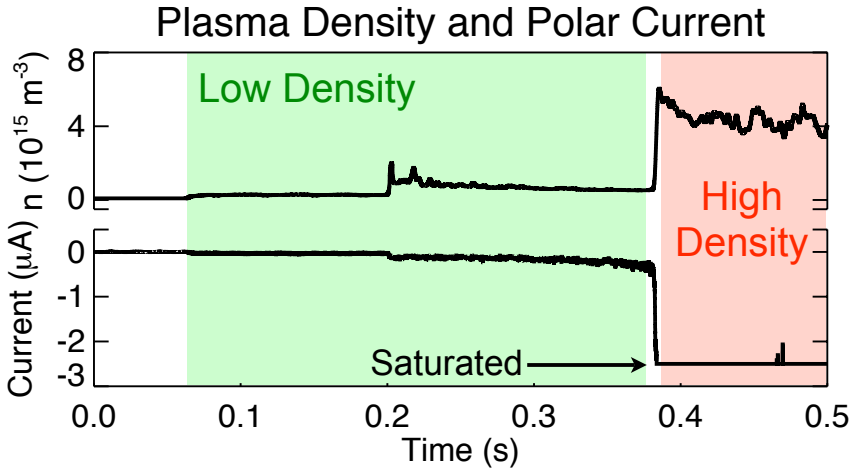

Figure 2.9: The plasma density and polar current as the gas fueling is increased displaying saturation of the polar detector. The plasma discharge is initiated near 0.5 s with a small amount of neutral H_2. A fast gas injection is triggered at 0.2 s increasing the plasma density. Another gas injection is triggered just before 0.4 s causing a transition into the high density regime.

When the grids are biased to repel electrons, the magnitude of the collected current is decreased ($|I_{polar}| < 5\ \mu$A), and the sign changes from negative to positive (Fig.2.10). It is when electrons are repelled that the polar imager records current fluctuations proportional to fluctuations in density as a Langmuir probe in the bulk plasma collecting ion saturation current (See Fig.4.9).

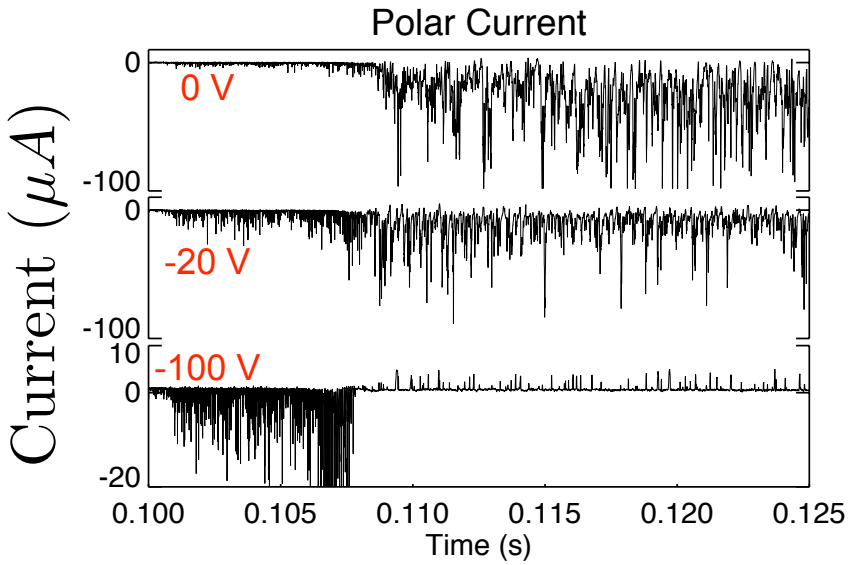

Figure 2.10: The polar current measured by a single gridded particle detector with the new low-gain amplifier as the electron repeller bias is increased from $V_{bias} = 0$ V to $V_{bias} = -100$ V. With sufficient bias, the polar detectors measure plasma density fluctuations in the high density regime.

2.2.4 Fast Camera

As a new diagnostic to CTX, a high speed digital video camera has been used to image the visible light emission during high density discharges. The Vision Research Phantom v7.1 (Fig.2.11) is a high speed CCD camera capable of frame rates above 10,000 frames per second, and uses a large aperture Sigma 30 mm f/1.4 lens. Video images of the plasma are captured through a port-hole located near the magnet vacuum feed-thru and focused at the equatorial midplane of the dipole field.

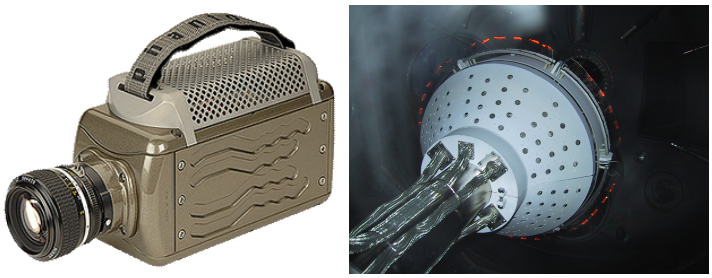

Figure 2.11: The Phantom v7.1 high speed digital video camera and the view-port through which the high-speed movies are taken (digital still photograph).

As the frame rate of the camera is increased, less light is captured within each frame. Because of the low light intensity from plasmas in CTX, frame rates greater than 10,000 fps have poor signal to noise ratios. Although this frame rate is slightly too slow to view the plasma motion of interest with $f \approx 1 - 4$ kHz, average profiles of light intensity and light fluctuation intensity can still be useful.

2.3 Producing Plasmas in CTX

Electron Cyclotron Resonance Heating (ECRH) at 1 kW is applied to neutral Hydrogen (H_2) to create the plasmas in CTX. Plasmas in CTX are categorized by 'low density' with neutral pressure $p_H < 10^{-5}$ Torr achieving plasmas around $n \approx 10^{14} - 10^{15}$ m^{-3}. In the 'high density regime' with neutral pressures $p_H > 10^{-5}$ Torr, densities can exceed $n \approx 10^{16}$ m^{-3}. The high density regime sees plasma densities approach the cutoff density $n_c \approx 7.5 \times 10^{16}$ m^{-3}. Once a low density plasma is formed, a second gas injection is triggered to cause the transition to the high density turbulent confined state.

The low density regime is characterized by quasi-periodic instabilities previously identified as the hot electron interchange (HEI) instability. When the neutral pressure is increased past the threshold level the fraction of hot to cold electrons drops. This stabilizes the hot electron interchange mode [52], and the high density, turbulence confinement regime is achieved.

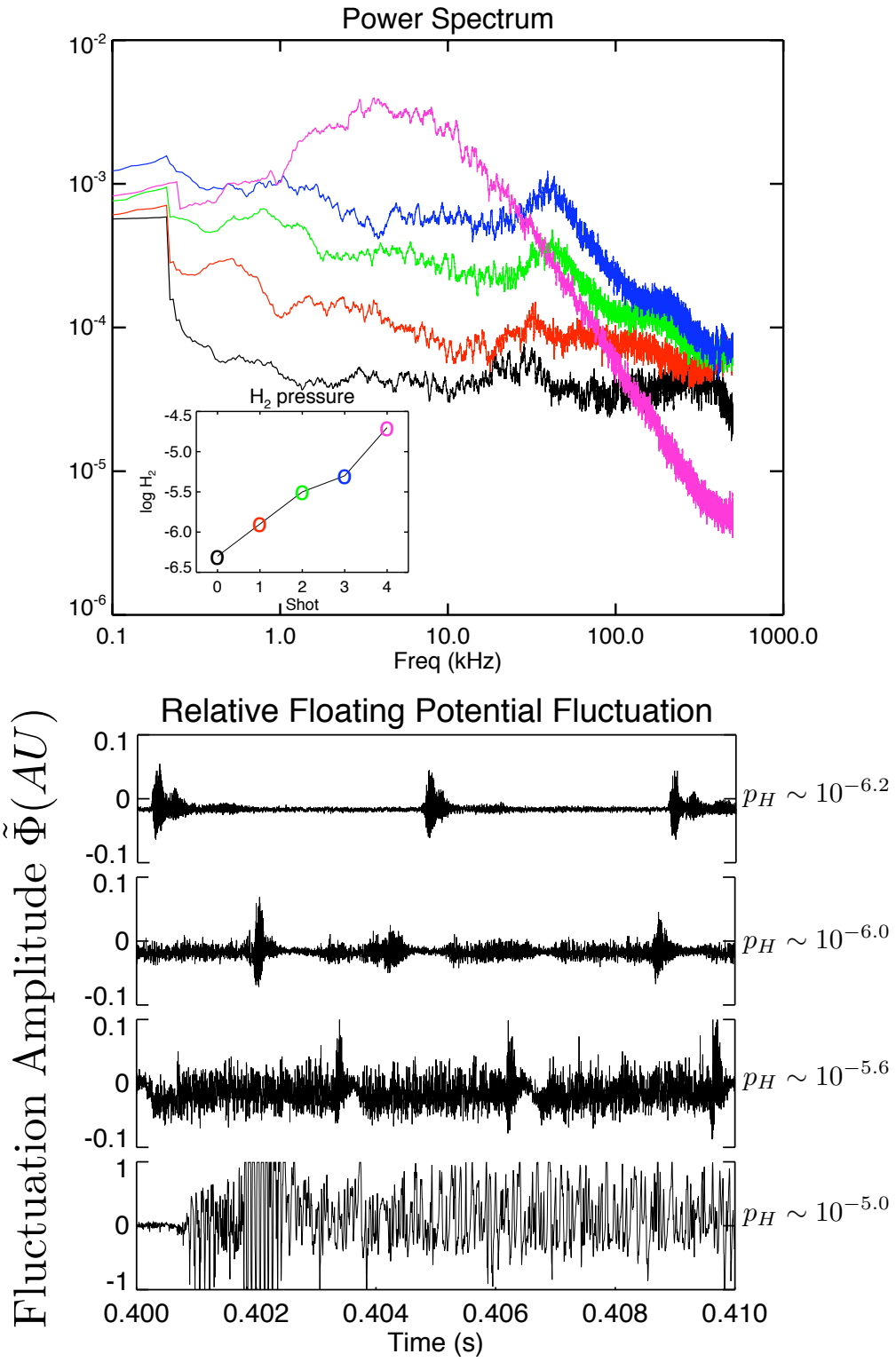

Figure 2.12: The transition to the high density, turbulent regime is achieved through increased neutral pressure. Power spectrum of floating potential fluctuations (top) and associated signal samples (bottom) for increasing neutral pressure. Once the neutral pressure exceeds $p_H \sim 10^{-5.3}$ Torr, the transition to fully developed turbulence occurs. (Note axis is $\times 10$ on bottom plot)

2.4 Basic Plasma Parameters

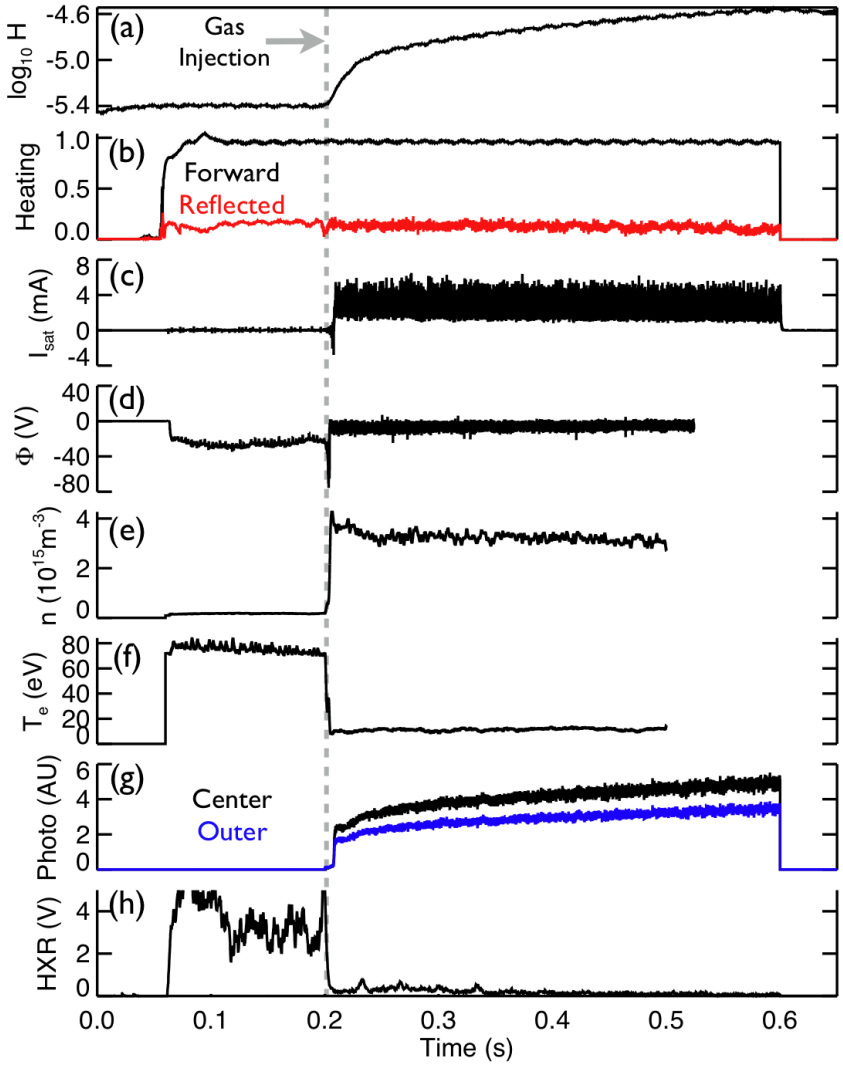

Figure 2.13: The evolution of basic plasma parameters during a discharge which enters the high density, turbulent regime at 0.2 seconds. (a) Hydrogen pressure, (b) microwave forward and reflected power, (c) edge density with an I_{sat} probe, (d-f) edge floating potential, smoothed density and smoothed temperature from a triple probe, (g) photodiodes, (h) hard x-ray emission.

2.4.1 Transition to Turbulent Regime

Upon gas injection which increases the neutral pressure above 10^{-5} Torr, a dramatic transition occurs to the high density, turbulent confined state. The transition is marked by a large amplitude, non-axisymmetric, rotating $m = 1$ potential mode with frequency near 18-20 kHz. The DC value of the potential drops to $\Phi_f < -50$, with large amplitude potential fluctuations of order $\tilde{\Phi} \sim 30$ V. The ion saturation current at the plasma edge becomes strongly modulated and negative, caused by the presence of hot electrons at the plasma edge. The hard X-ray emission drops and the soft x-ray emission rises, indicating a reduction of the highest energy hot electron production. Immediately following the transition to turbulence, the density rises dramatically, and broadband fluctuations in potential and density are observed.

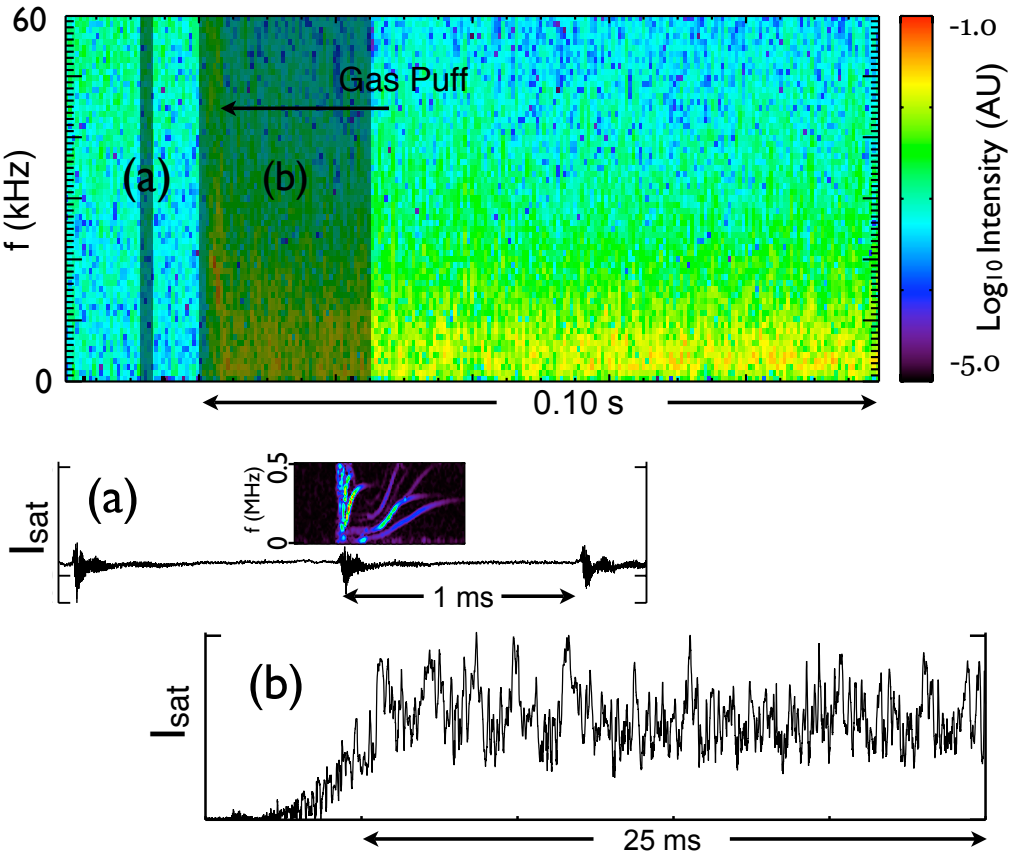

Figure 2.14: The transition from the low density regime (a) dominated by HEI to the high density turbulent regime (b).

2.4.2 Density and Potential Profile

Measurements of density profiles are obtained through a movable Langmuir probe measuring ion saturation current (proportional to density). The numerical values of density in Fig.2.16 are obtained by equating current from the I_{isat} probe and density from the triple probe at the edge of the plasma. The I_{isat} probe is then inserted into the plasma to measure the density profile, as well as relative fluctuation level (seen in Fig.2.15). The density profile is measured to be slightly steeper than $n \sim L^{-4}$. This serves as an indication that rotation may play a role in exciting fluctuations, as this is the marginally stable profile for rotationally driven interchange motion. The density fluctuation level is large across the accessible plasma radius, with peak-to-peak levels of $\delta n/n_0$ ~50% near L=50 cm where most of the fluctuation measurements are taken. The triple probe is large, and tends to perturb the plasma significantly when inserted at the equatorial midplane, and measures a profile less steep than the I_{isat} probe or radial polar loss profile.

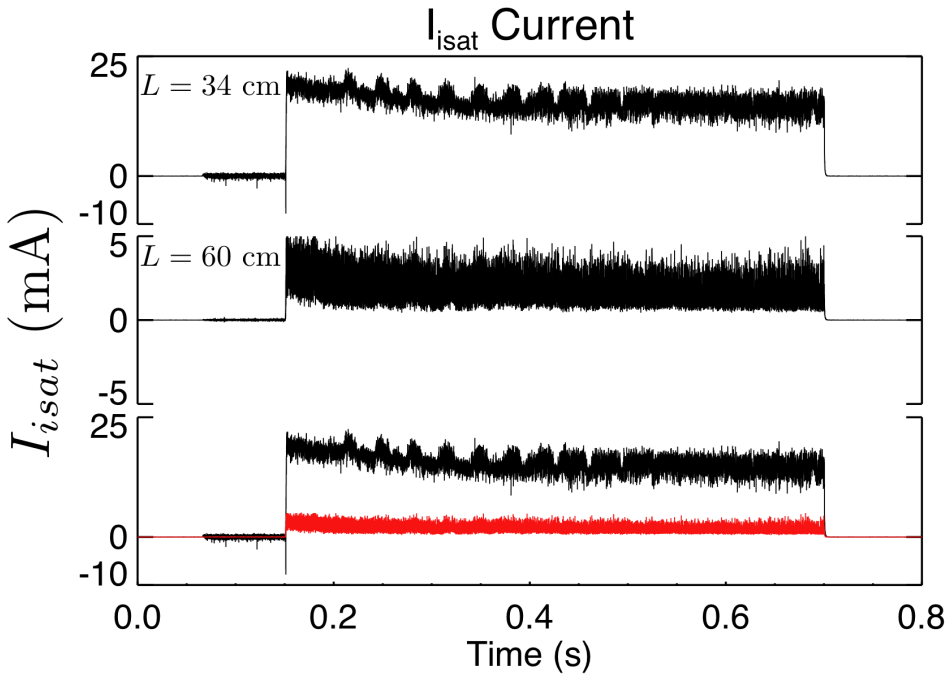

Figure 2.15: Ion saturation current ($\propto n$) measured at equatorial radius L=34 cm and L=60 cm. Both are plotted on the same scale in the bottom trace for reference. The $f \sim 30$ Hz oscillations are attributed to the magnet power supply, and not plasma dynamics.

The potential profile inside the SOL is measured to follow an approximate $1/L$ trend. This indicates approximate rigid rotation of the plasma near the edge of the device in the $-\hat{\varphi}$ direction. The edge potential profile in high density, as well as the calculated and observed rotation, are in the same azimuthal direction as the near sonic driven rotation investigated previously in CTX [57]. The time-averaged potential profile can also be calculated by inverting the continuity equation (Sec.3.34). The measured profile and calculated profile follow similar trends for $L \geq 50$ cm where the plasma is accessible with a floating potential probe.

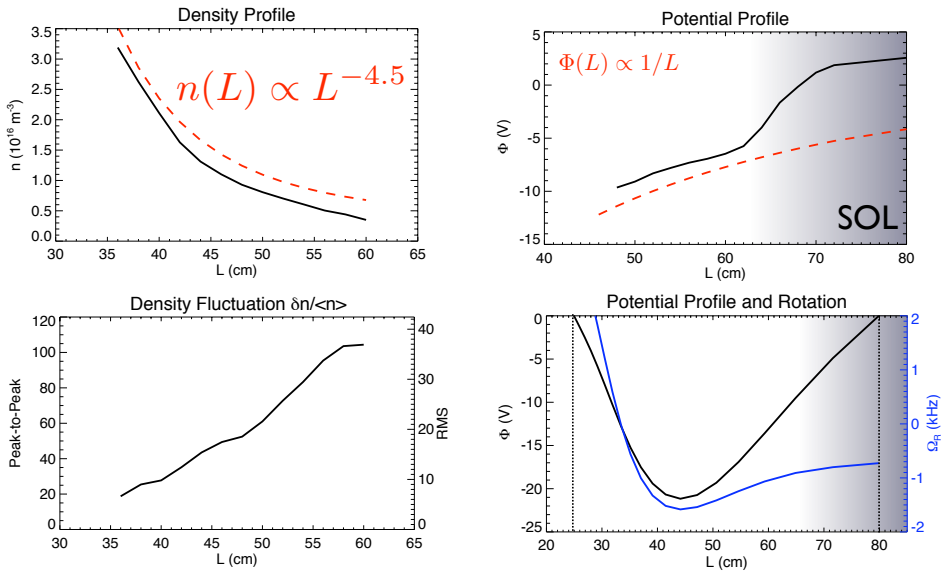

Figure 2.16: The radial profiles of density and potential. The density profile is maintained slightly steeper than the marginal profile for interchange modes, $n \propto L^{-4}$. Fluctuation intensity rises at larger radii. In the bulk plasma, the potential is measured to vary as $1/L$. The potential profile from the stream function calculation agrees with probe measurements, as well as rotation speed near 1-2 kHz at $L = 50$ cm.

2.5 Summary

The high density, turbulent plasmas which are investigated in this thesis are produced by electron cyclotron resonance heating (ECRH) of neutral hydrogen. The plasmas are stable to the hot electron interchange (HEI) mode due to an increase of colder background plasma, achieved through increased fueling. The stability to HEI modes allows the density to increase to $n \sim 10^{16}\mathrm{m}^{-3}$, with bulk electron temperatures near $T_e \sim 8 - 10$ eV. These plasmas exhibit large relative fluctuations of density and potential as they rotate in the $\mathbf{E} \times \mathbf{B}$ azimuthal direction. The density profile is measured to vary slightly steeper than $n \propto L^{-4}$ on the outboard side of the device, and the potential profile indicates approximate constant rotation for this region of $f \sim 1 - 2$ kHz.

Chapter 3

Signal Processing Techniques for Turbulent and Nonlinear Fluctuations

A time series represents a measurement, and any time series has certain intrinsic features such as mean , variance, skewness, kurtosis, and trend. The time series also has certain other features such as auto-correlation time and frequency spectrum which may reveal the underlying processes which created it. The interpretation of a measurement and relation to the medium requires data analysis techniques to determine its statistical properties. This is usually done by some type of transformation from the time to frequency domain. Other techniques which are not spectral-based can also provide valuable information, such as the empirical mode decomposition based on the Hilbert transform [42] and the bi-orthogonal decomposition based on the Singular Value Decomposition (SVD) [22]. While most of the analyses are performed on a single time series or between two time series, the bi-orthogonal decomposition is a *global* decomposition of many space-time points. The inversion of the continuity equation for calculating the stream function is another such global calculation.

This chapter reviews standard signal processing techniques and establishes conventions which will be used in the following chapters. Some of the analysis techniques used in this thesis rely heavily on numerical computation. These more sophisticated analyses

are validated on model problems with well-defined inputs and outputs for determining their accuracy, and interpret the results unambiguously. The stream function calculation is benchmarked by evolving a two-dimensional density profile in time, and using spatial and temporal finite differences for inversion of the continuity equation.

The calculation of spectral energy transfer is validated on a turbulence model dependent on a linear dispersion relation, and estimates the structure coupling between modes across the entire relevant spectral region [71]. The amplitude correlation technique is an alternative method for investigating nonlinear coupling which investigates specific bands of the turbulent spectrum [20, 68]. Both of these methods are benchmarked on analytically defined models.

3.1 The Fourier Transform

The measurements of plasma fluctuations are stored in a digitized database, and these data are subject to several of analysis procedures, typically based on the Fourier Transform. The analytical Fourier transform $\hat{\phi}(\omega)$ of a time series $\phi(t)$ is given by

$$\hat{\phi}(\omega) = \int \phi(t) e^{-i\omega t} dt \tag{3.1}$$

where t, ω denote time and frequency respectively. The Fourier spectrum is a complex quantity, consisting of real and imaginary parts. This integration determines the dominant fluctuating component in a time series. In practice, this integration is performed numerically with the *Fast Fourier Transform* (FFT). The FFT quickly transforms a signal from the time domain into the frequency domain, and returns a complex-valued array. Windowing functions [35] are used to more accurately determining the spectrum by eliminating the edge effects of a finite time realization. The Hanning window is used to compute all spectral quantities in this thesis.

3.2 Ensemble Statistics

Turbulent fluctuations are 'non-stationary', and the spectrum of these fluctuations are necessarily calculated statistically in an ensemble of equivalent time intervals. Each ensemble consists of hundreds or thousands of individual realizations of the time record. Fluctuations of potential and density in CTX have a power-law character, where a single realization of the time record is not necessarily representative of the long-time averaged spectrum. The frequency at which peak power exists can vary for any single realization of the signal, and therefore the ensemble spectrum represents the statistical nature of the fluctuations in the plasma. This defines the need for 'ensemble statistics' when describing turbulent fluctuations.

The ensemble spectrum of a time varying quantity $A(t)$ over sub-samples $A_{(i)}(t)$ is given as

$$\langle \tilde{A} \rangle \equiv \frac{1}{M} \sum_{i=1}^{M} \tilde{A}_{(i)} \tag{3.2}$$

where $\tilde{A}_{(i)}$ being the Fourier transform of $A_{(i)}$ is an array containing any number of elements. The time-series $A(t)$ is analyzed in realizations length Δt. The width of the window must be chosen to accurately capture the low frequency components of the signal. The lowest frequency able to be resolved is $1/\Delta t$, and is also the increment of the frequency axis. The highest frequency able to be resolved is the *Nyquist frequency* given by $f_d/2$, half of the digitizing frequency. The 'window' of time is then advanced with time step δt; typically $\delta t = \Delta t/2$. Decreasing δt provides better time resolution in a *spectrogram* plot of fluctuations. Increasing δt provides better frequency resolution in a spectrogram plot of fluctuations.

3.3 Auto-Correlation and Power Spectrum

3.3.1 Correlation Function

With a single time series, the auto-correlation function can be calculated as

$$C(\tau) = \frac{\int S(t)S(t-\tau)dt}{\int S(t)^2 dt} \tag{3.3}$$

and is normalized to $C(\tau) \in [-1, 1]$. The correlation time interval, τ_c, can be defined as $\tau_c = C(0)^{-1} \int C(\tau)d\tau$, or $\tau_c = \frac{1}{2}\int |C(\tau)|d\tau$ for a correlation function which is positive. A "correlation-in-time" spectrogram-like plot can be created by forming a sequence of correlation functions in a two-dimensional array

$$C(t, \tau) = [C_{(i)}(\tau), C_{(i+1)}(\tau) \ldots] \tag{3.4}$$

where each correlation function $C_{(i)}(\tau) = \int S_{(i)}(t)S_{(i)}(t-\tau)dt / \int S_{(i)}(t)^2 dt$. This can then be integrated in time to form an ensemble correlation function as

$$\langle C(\tau) \rangle = \int (C(t, \tau)dt = \frac{1}{M}\sum_{i=0}^{M-1} C_{(i)}(\tau) \tag{3.5}$$

3.3.2 Ensemble Spectrum

Utilizing the time series obtained from a single diagnostic, the ensemble spectrum can be calculated as

$$\langle |\tilde{S}(\omega)|^2 \rangle \equiv \langle \tilde{S}(\omega)\tilde{S}^*(\omega) \rangle, \tag{3.6}$$

which is the auto-spectrum, or auto-power, or auto-correlation function in the frequency domain. The asterisk (*) denotes complex conjugate. The auto-spectrum is a real quantity, and measures the relative amplitude of each frequency component in the time-series. For a single diagnostic, quantities such as ensemble fluctuation spectrum and bi-spectrum [49] are

spectral quantities which can be calculated. The bi-spectrum is a measure of the strength of quadratically nonlinear interactions in a signal and is given by

$$B(\omega_1, \omega_2) = \langle \tilde{S}(\omega_1)\tilde{S}(\omega_2)\tilde{S}^*(\omega_1 + \omega_2)\rangle \tag{3.7}$$

and is a complex quantity. The bi-coherence is a power weighted bi-spectrum, and determines

$$b^2(\omega_1, \omega_2) = \frac{|B(\omega_1, \omega_2)|^2}{\langle|\tilde{S}(\omega_1)\tilde{S}(\omega_2)|^2\rangle\langle|\tilde{S}(\omega_1 + \omega_2)|^2\rangle} \tag{3.8}$$

which is essentially a quadratic correlation coefficient.

3.4 Cross-Correlation and Fourier Statistics

3.4.1 Cross-Correlation Function

With two time series, the cross-correlation function is

$$C_{1,2}(\tau) = \frac{\int S_1(t)S_2(t-\tau)dt}{\sqrt{\int S_1(t)^2 dt \int S_2(t)^2 dt}} \tag{3.9}$$

and is normalized to $C_{1,2}(\tau) \in [-1, 1]$. This quantity is useful in calculating the 'lag-time' between two signals. The lag time, τ_{Lag}, is the value of τ at which the cross-correlation function is maximized. As an example, consider two test pulses $S_1(t) = \sin(\omega t)$, $S_2(t) = \sin(\omega t - \pi/2)$ at $2\pi f = 10$ Hz in a gaussian envelope where the second signal lags in phase by $\pi/2$ Fig. 3.1. The lagged measurement represents the recording of the same pulse at a *downstream* location, or in the direction of propagation. The cross-correlation function has a maximum at $\tau = 0.0250$ s. The phase shift between the signals in radians can be calculated by $|\alpha| = \omega\tau_{Lag} = 2\pi \times 10\text{ Hz} \times 0.0250\text{ s}$ which is equal to $\pi/2$. If the two measurements were taken by diagnostics separated by Δx, then the velocity of propagation of this pulse would be $\Delta x/\tau_{Lag}$.

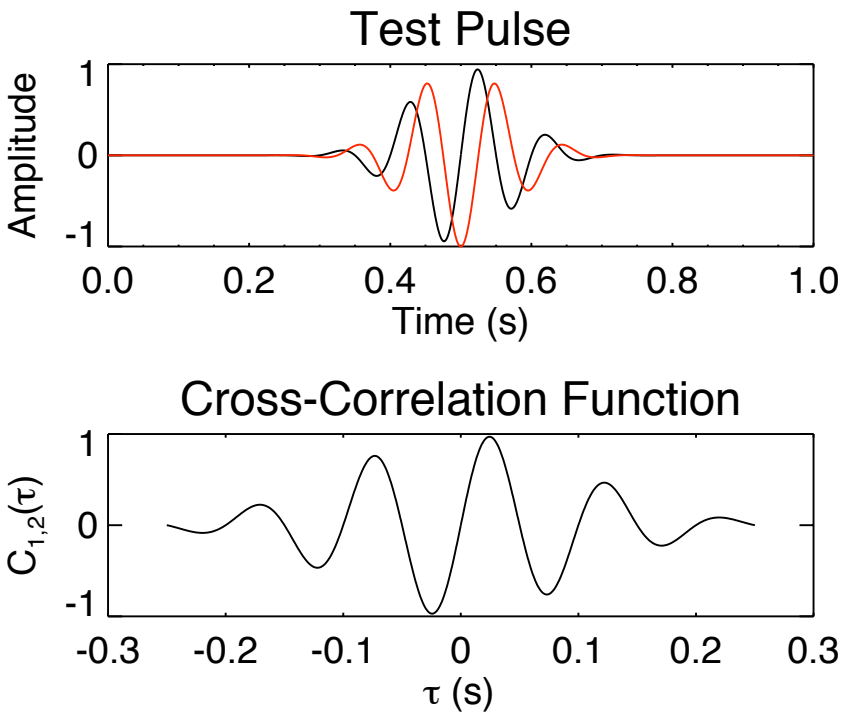

Figure 3.1: Test pulse and cross correlation function between signals 1 and 2 (red). The *positive* lag time indicates that signal 2 *lags* signal 1, or occurs at a later time.

3.4.2 Cross-Coherence and Phase

When two diagnostics are used, valuable information about the fluctuations can be obtained. The cross-power spectrum and cross-phase are the two of the most widely reported measurements in plasma physics, and are defined as

$$\begin{aligned} \langle \tilde{C}_{1,2} \rangle &\equiv \langle \tilde{S}_2 \tilde{S}_1^* \rangle \\ \langle \alpha_{1,2} \rangle &\equiv \tan^{-1}\left(\frac{\Im[\langle \tilde{C}_{1,2} \rangle]}{\Re[\langle \tilde{C}_{1,2} \rangle]} \right) \end{aligned}$$

and are also calculated in an ensemble-sense. The cross-power is a complex quantity with both real and imaginary parts. The reported value of cross-phase is the value where cross-power is maximized. There can be many peaks in the cross-power spectrum, and each peak has a phase value associated with it. The phase value where there is negligible cross-power is meaningless. A normalized cross-power is the squared cross-coherence

$$\langle \kappa_{1,2} \rangle^2 \equiv \frac{|\langle \tilde{C}_{1,2} \rangle|^2}{\langle \tilde{S}_1 \tilde{S}_1^* \rangle \langle \tilde{S}_2 \tilde{S}_2^* \rangle} \tag{3.10}$$

which is bounded by $\langle \kappa_{1,2} \rangle^2 \in [0, 1]$. A peak in the cross-coherence is considered meaningful if it is non-zero and converged. If there exists one dominant peak in the spectrum, then the integrated cross-phase can be calculated as

$$\langle \alpha_{1,2} \rangle_{\int} \equiv \frac{\int \langle \alpha_{1,2} \rangle(\omega) |\tilde{C}_{1,2}(\omega)| d\omega}{\int |\tilde{C}_{1,2}(\omega)| d\omega} \tag{3.11}$$

Two test sinusoids $\sin(\omega t), \sin(\omega t - \pi/2)$, $\omega = 2\pi \times (f_0 + \delta f)$ with $f_0 = 500$ Hz digitized at 10 kHz have been created. Each has 10% random noise on the frequency ($\delta f \in [-25, 25]$ Hz) and 20% random noise added to the amplitude. The ensemble cross-coherence, phase, and integrated cross-phase have been computed and are shown in Fig. 3.2. Without performing the appropriate ensemble averages, the cross-power and phase cannot detect the correct frequency-phase relation between the two test signals.

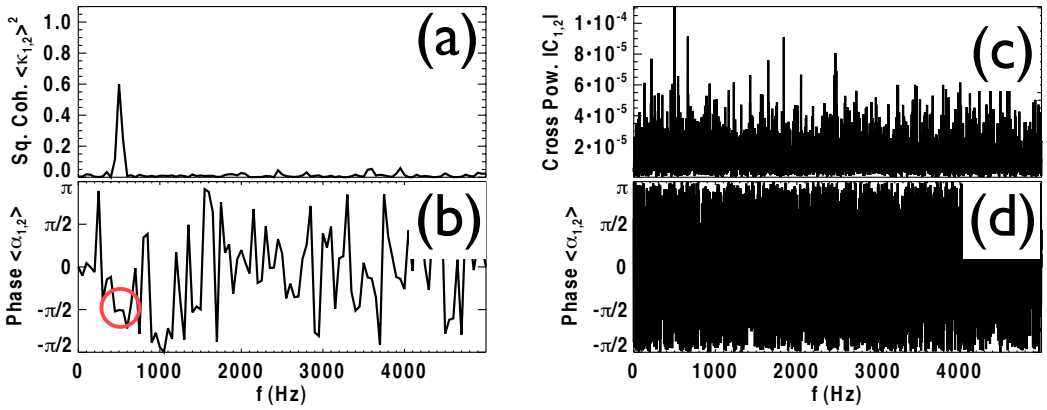

Figure 3.2: (a) Ensemble coherence and (b) phase for test signals phase shifted by $-\pi/2$. The circle indicates the phase value where there is significant coherence. The integrated cross-phase is $\langle\alpha_{1,2}\rangle_{\int}$=-1.57907 which is an error of 8%. (c) The cross-power and (d) cross phase for the same signals without performing ensembles. The integrated phase is $\langle\alpha_{1,2}\rangle_{\int}$=0.0103.

When two probes are separated by a distance Δx, the wavenumber spectrum as a function of frequency can be calculated using the relationship

$$k(\omega) = \frac{\langle\alpha_{1,2}\rangle}{\Delta x} \tag{3.12}$$

which provides information about the dispersion relation of the wave [10, 23]. When the dispersion curve is linear, one is able to relate a frequency to a wavenumber by a phase velocity, given by $v_{ph} = \omega/k$, for pure linear advection.

3.5 Hilbert Spectrum

A new method for examining nonlinear phenomena, called the Empirical Mode Decomposition [42], aims to decompose a complex time varying signal into a series of 'mode functions'. The mode functions all live at different time scales and at different amplitudes. This is an alternative to prescribing a Fourier basis and calculating the amplitude in each Fourier mode. To decompose a function is to examine the intrinsic time scales and investigate the amount of signal power which exists there.

The Hilbert Transform of a time series $X(t)$ is given by

$$Y(t) = \frac{1}{\pi} P \int_{-\infty}^{\infty} \frac{X(t')}{t - t'} dt' \tag{3.13}$$

where P indicates the Cauchy Principle Value. With this transform, we can define a new analytic function $Z(t)$ such that

$$Z(t) = X(t) + iY(t) = a(t)e^{i\theta(t)} \tag{3.14}$$

We now can extract the amplitude and the instantaneous phase via

$$a(t) = \sqrt{X(t)^2 + Y(t)^2} \quad \theta(t) = \arctan\left(\frac{Y(t)}{X(t)}\right) \tag{3.15}$$

The phase, θ, must be 'unwrapped', in order to take the time derivative, yielding the instantaneous frequency $\omega(t)$, given by

$$\omega(t) = \frac{d\theta(t)}{dt} \tag{3.16}$$

The average frequency, or slope of the phase, gives an average time scale at which the fluctuations occur.

Duffing's equation is a classic nonlinear oscillator. One form of the ODE is

$$\frac{d^2x}{dt^2} + x + \epsilon x^3 = \gamma \cos(\omega t) \tag{3.17}$$

where ϵ is the nonlinear parameter, γ is the amplitude of the driving term, and ω is the driving frequency (here $\omega_0^2 = 1$). Duffing's equation has been solved by perturbation methods with the solution as a basic frequency and all its superharmonics $x(t) = \cos \omega t + \epsilon \cos 3\omega t + \epsilon^2 \cos 6\omega t$. While that solution may be correct mathematically, it is still a sum of linear modes to represent a single nonlinear phenomena. Neither the solution or its components lend any physical insight into the full nonlinear system. If we write Eq.3.17 in the following form

$$\ddot{x} + x(1 + \epsilon x^2) = \gamma \cos \omega t \tag{3.18}$$

then we can see that this is a driven harmonic oscillator, with a nonlinear restoring force (spring constant). Alternatively, it can be viewed as a pendulum with a forcing function, but the length of the pendulum is not constant. Both of these views imply a frequency which is not constant within one period of the motion: An obvious problem for a Fourier spectral decomposition. Let us now examine Duffing's equation for $\epsilon = -3.0, \gamma = 1.5, \omega = 2.5$, shown in Fig.3.3.

The spectral treatment of Duffing's equation produces superharmonics in the frequency spectrum as expected. In order to apply the Hilbert spectrum method, the signal is required to have no positive minima or negative maxima, otherwise the instantaneous frequency will spike to infinity. Therefore, the time series needs to be *sifted* into *intrinsic mode function* (IMFs). This is done by first fitting a spline to all the maxima and minima of the function, $S_{max}(t), S_{min}(t)$. The mean of those two splines is subtracted from the time series . This process is repeated using the until the IMFs in the frequency range of interest have been extracted. The method is illustrated in Fig. 3.4. The sifting is complete in that no information about the time series is lost. The difference between the original signal and the sum of its

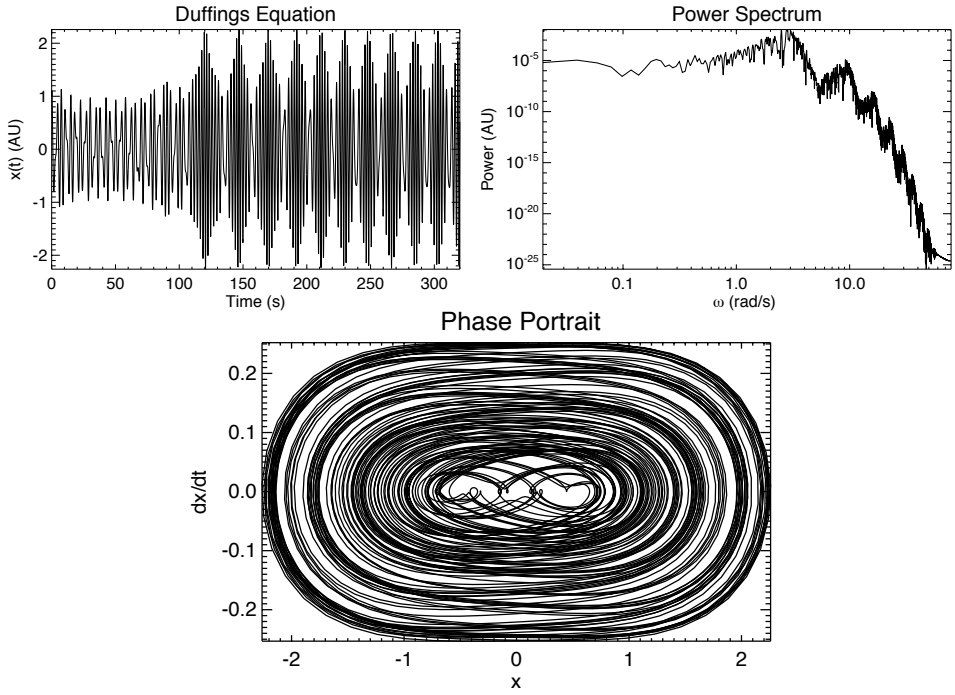

Figure 3.3: The time-integrated Duffing's equation, Fourier spectrum and phase portrait. The spectrum displays the generation of superharmonics. The phase-portrait displays the nonlinear behavior where the attractor approaches but does not remain at fixed points or in limit cycles.

mode functions is on the order of computational precision, where the example is done in single-precision arithmetic.

The sifting of the signal is thus a way of examining the different *intrinsic* frequencies of the fluctuating quantity, whereas each mode function lives near an average frequency. The IMF which is most strongly correlated with the original signal is the one which best describes the behavior.

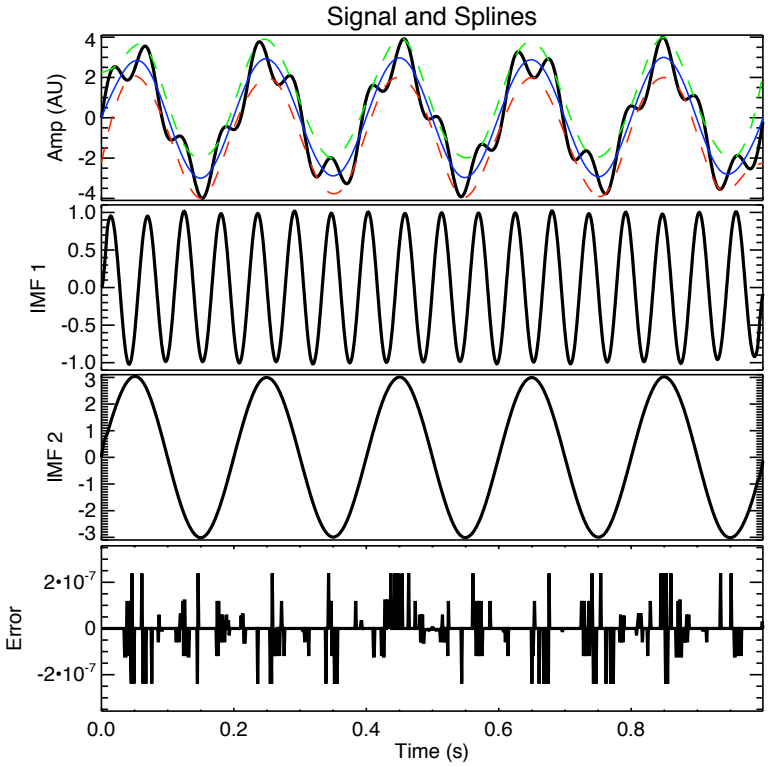

Figure 3.4: The sifting of the function $f(t) = 3\sin(2\pi f_1 t) + \sin(2\pi f_2 t)$ with $f_1, f_2 = 5, 18$ Hz. Minima, maxima and mean splines are plotted as (r,g,b). IMFs are sorted in increasing frequency, and recover the correct amplitude and frequency of the model. The error is negligible.

Taking the time series from Duffing's equation, the modal decomposition and Hilbert-Huang spectrum are displayed in Fig.3.5. The Hilbert spectrum contour is a sum of instantaneous frequencies in time, similar to a spectrogram. The 'energy' in time is calculated as

$$IE(t) = \int H(\omega, t) d\omega \tag{3.19}$$

and measures the total signal energy contribution from all spectra at a given time point.

Early in the Duffing's time series, the attractor displays asynchronous orbits near the fixed points in phase space with two characteristic frequencies when the trajectory is close and far from the fixed points. It is this time where positive minima and negative maxima exist, causing a split in the IMFs. Once the attractor enters a large-radius limit cycle, the first IMF is sufficient to describe the evolution of the attractor.

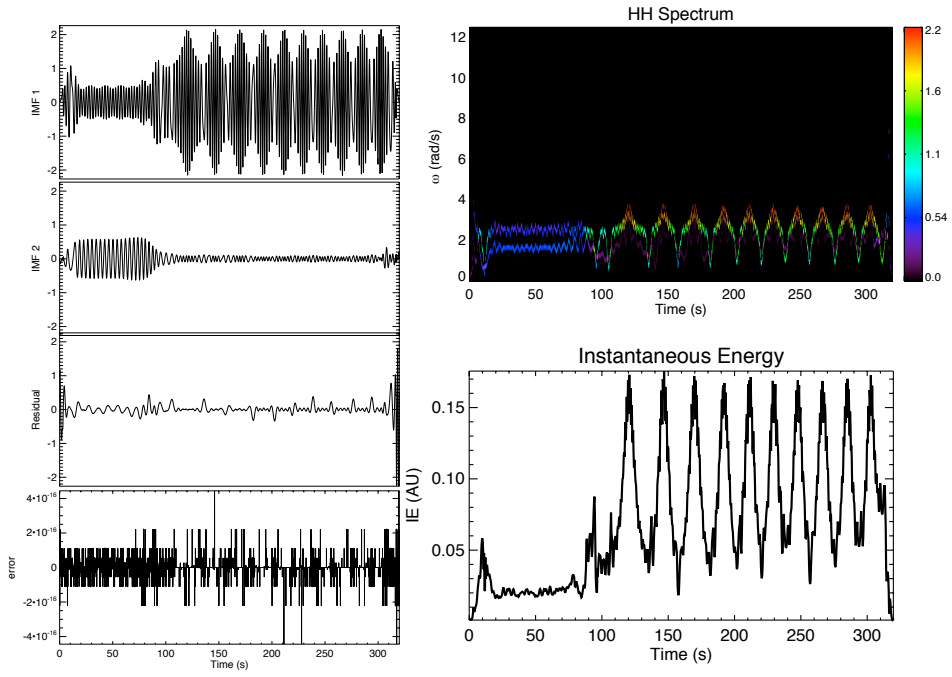

Figure 3.5: The modal decomposition of Duffing's equation.

3.6 Bi-Orthogonal Decomposition

When multiple space-time points are used for measuring fluctuations in a plasma, the observed fluctuations can be decomposed into spatial and temporal modes X_k and T_k, respectively, with the bi-orthogonal decomposition. The seminal paper on the analysis is given by Dudko de Wit *et. al.* [22], and has been used on the JET [67] and HT-7 [91]. The amplitude of each spatio-temporal mode is given by a "singular value", σ_k. Using the

bi-orthogonal decomposition Eq.3.20, the density fluctuations in CTX measured by the Polar Imager have been decomposed into mutually orthogonal spatial mode functions and their respective mutually orthogonal temporal variation.

$$n(x_j, t_i) = \sum_{k=0}^{K-1} \sigma_k X_k(x_j) T_k(t_i) \tag{3.20}$$

Here, $K = \text{Min}\{\text{M}, \text{N}\}$, where M is the number of spatial measurement points, N is the number of time points. The orthogonality relation is given as

$$\sum_{i=0}^{N-1} T_k(t_i) T_l(t_i) = \sum_{j=0}^{M-1} X_k(x_j) X_l(x_j) = \delta_{k,l} \tag{3.21}$$

The decomposition of this equation is done via

$$\mathcal{A}_X X_k = \sigma_k^2 X_k \quad , \quad \mathcal{A}_X = n^T n \tag{3.22}$$

$$\mathcal{A}_T T_k = \sigma_k^2 T_k \quad , \quad \mathcal{A}_T = n n^T \tag{3.23}$$

where the Singular Value Decomposition is used to extract the ‘eigenvalues’.

While the decomposition of Eq.3.22 solves for σ_k^2, the additional constraint on the sign of σ_k comes from the isomorphism

$$n X_k = \sigma_k T_k \tag{3.24}$$

which is necessary for the proper reconstruction of the observation.

3.7 Lyapunov Spectrum

The Lyapunov characteristic exponent of a system provides the rate of divergence of nearby trajectories in phase-space. In a dynamical system, the existence of a positive Lyapunov exponent is the hallmark of chaos [1, 81]. One of the most familiar nonlinear dynamical systems exhibiting chaos is the Lorenz system [59], which is a system of three coupled nonlinear ordinary differential equations for $(\dot{x}, \dot{y}, \dot{z})$ (Eq.3.25). The Lorenz system, existing in a three-dimensional phase space, has three Lyapunov numbers $\lambda_i = \{1.5, 0.0, -22.5\}$ obtained analytically.

$$\begin{aligned} \frac{dx(t)}{dt} &= \sigma[y(t) - x(t)] \\ \frac{dy(t)}{dt} &= -x(t)z(t) + rx(t) - y(t) \\ \frac{dz(t)}{dt} &= x(t)y(t) - bz(t) \end{aligned} \tag{3.25}$$

The Lorenz system was originally derived from a finite mode truncation of the partial differential equations describing thermal convection in the Earth's lower atmosphere. When the Lorenz system is integrated in time, the time series of one of the variables (x, y, z) can be used to numerically calculate the Lyapunov spectrum [28]. The three-dimensional phase portrait of the Lorenz attractor is provided in Fig.3.6, along with a single realization of the variable x and it's associated power spectrum. The Lorenz x time series presented here has an auto-correlation time of $\tau_c C(0)^{-1} \int C(\tau) d\tau \approx 0.3$ s, shorter than the Lyapunov time of $\lambda^{-1} \approx 0.667$s by slightly more than a factor of two. The power spectrum admits a power-law decay above $f \approx 4$ Hz. The method for calculating the Lyapunov spectrum projects the time series in a d_E dimensional space $\mathbb{R}^1 \rightarrow \mathbb{R}^{d_E}$, forming a sequence of vectors, rather than a time series. A time series $x(t) = x[i\tau]$, $\{i : i = 1, 2, \ldots, n\}$ exists in one dimension. This time series is projected by the time-lag method to create an embedded set of vectors, illustrated

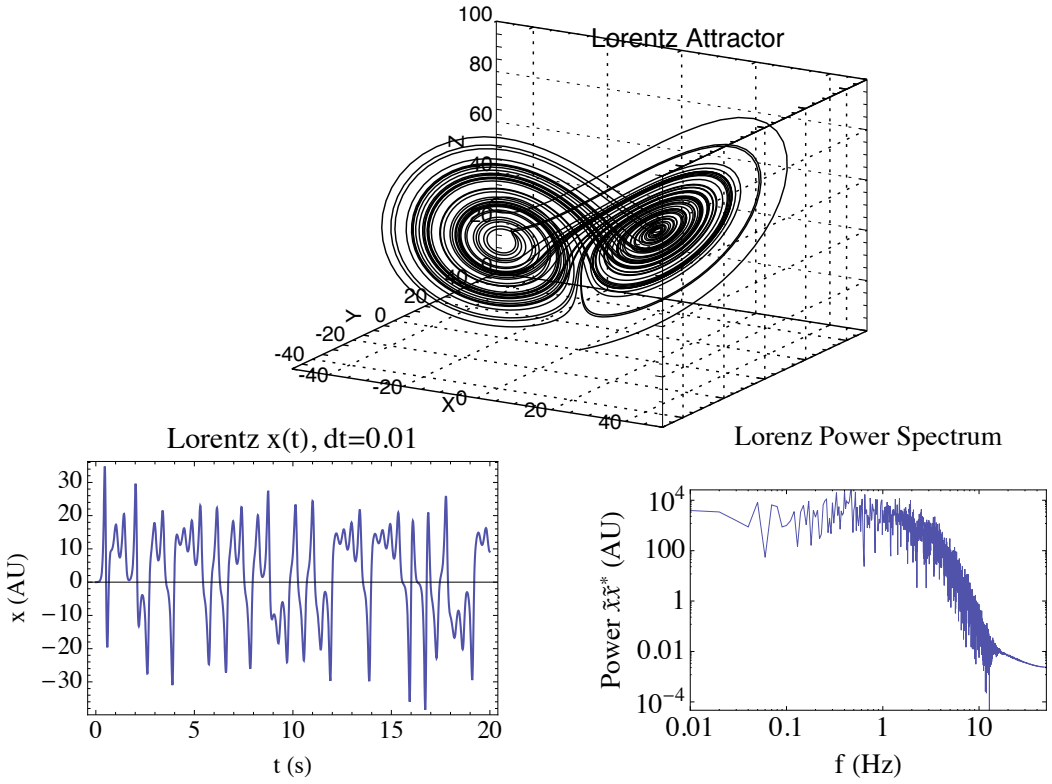

Figure 3.6: The Lorenz system (top) is a 'strange attractor'. The parameters are $r = 45.92, b = 4, \sigma = 16$. One sample time series $x(t)$ from the Lorenz system is displayed, as well as the power spectrum for a time record of 10,000 time points. The time step for Runge-Kutta integration is 0.01.

by $\mathbb{R}^1 \rightarrow \mathbb{R}^3$ as

$$\begin{array}{c} 1 \\ 2 \\ 3 \\ 4 \\ 5 \\ 6 \end{array} \quad \rightarrow \quad \begin{array}{ccc} 1 & 2 & 3 \\ 2 & 3 & 4 \\ 3 & 4 & 5 \\ 4 & 5 & 6 \end{array} \tag{3.26}$$

transforming a length n vector to a set of $n - d_E + 1$ sets of d_E coordinates. We now calculate the 'neighbors' of vector $\mathbf{x}_i$ such that the condition

$$\|\mathbf{x}_j - \mathbf{x}_i\| \leq r \tag{3.27}$$

is satisfied. Here, $\mathbf{x}_i = \{x_i, x_{i+1}, \ldots, x_{i+d_E-1}\}$ is a given set of d_E coordinates (a row in the embedded set of Eq.3.26). The embedding of the time series results in a 'recurrence plot' [27, 24, 95] for the system. This is a $(n - d_1 + 1) \times (n - d_E + 1)$ array where the j's satisfying the inequality condition are given a 1, else 0. Recurrence plots of periodic systems display long lines parallel to the diagonal (sinusoid). If there are short lines parallel to the diagonal, then in that embedded dimension a periodicity exists for a short time, and then diverges. This is true for an attractor which exists near a fixed point in phase space, and then leaves the region of that fixed point.

Once the series has been embedded, neighbor points in this space within a d_E dimensional sphere are found with a search algorithm (Appendix D), resulting in the set $S_i(r)$, which are the positions in the rows of the recurrence plot where there is a 1. We then want to determine the $d_E \times d_E$ matrix T_i which describes how time evolution sends small vectors around $\mathbf{x}_i$ to small vectors around $\mathbf{x}_{i+1}$. This is done with the matrix equation

$$T_i(\mathbf{x}_j - \mathbf{x}_i) \approx \mathbf{x}_{j+1} - \mathbf{x}_{i+1} \tag{3.28}$$

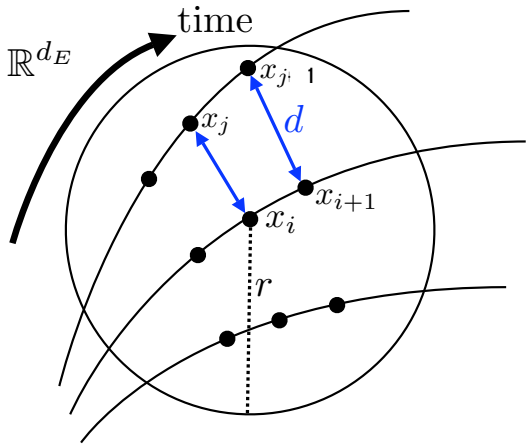

Figure 3.7: Schematic of phase space containing diverging trajectories within a $\mathbb{R}^{d_E}$ dimensional sphere of radius r.

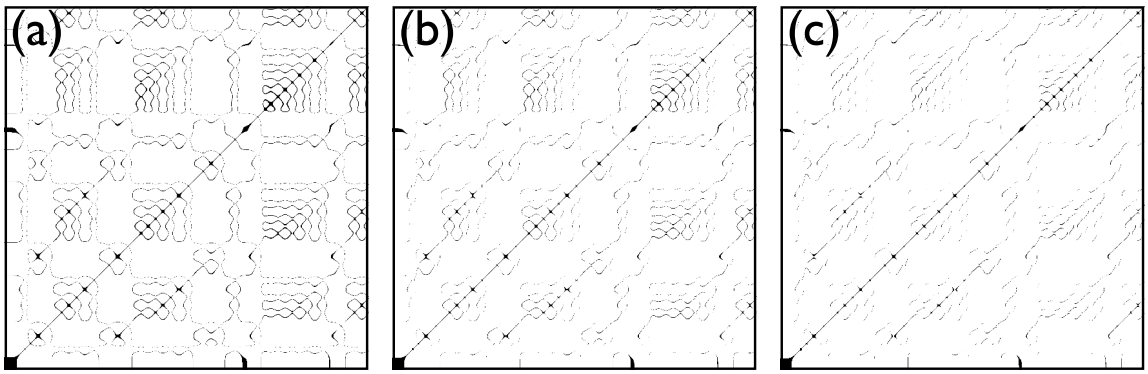

Figure 3.8: Recurrence plots for the Lorenz system embedded in 1, 2 and 3 dimensions (a-c). For embedding dimension $d_E = 1, 2$ there is a 'checkerboard' pattern. For embedding dimension $d_E = 3$, there are long lines parallel to the diagonal.

where T has the form

$$T_i = \begin{pmatrix} 0 & 1 & 0 & \dots & 0 \\ 0 & 0 & 1 & \dots & 0 \\ \vdots & \vdots & \vdots & & \vdots \\ a_1 & a_2 & a_3 & \dots & a_{d_E} \end{pmatrix}$$

where the last row is obtained from a least-squares solution

$$\sum_{j \in S_i(r)} \left[\sum_{k=0}^{d_E-1} a_{k+1}(x_{j+k} - x_{i+k}) - (x_{j+d_E} - x_{i+d_E}) \right]^2 = \min \tag{3.29}$$

This will yield a set of $T_i, T_{i+1}, \dots$ matrices. We then determine, successively, orthogonal Q_i matrices and upper-triangular matrices R_i with positive diagonal elements (making the decomposition unique), such that $Q_{(0)}$ is the unit matrix, and

$$\begin{aligned} T_1 Q_{(0)} &= Q_{(1)} R_{(1)}, \\ T_2 Q_{(1)} &= Q_{(2)} R_{(2)}, \\ &\dots, \\ T_{1+j} Q_{(j)} &= Q_{(j)} R_{(j)}, \\ &\dots \end{aligned}$$

The Lyapunov exponents are obtained by the sum of the diagonal entries in R.

$$\lambda_k = \frac{1}{\tau K} \sum_{j=0}^{K-1} \ln R_{(j)kk} \tag{3.30}$$

This analysis has been performed with one time series, representing an observed measurement, from the Lorenz system generated by fourth-order Runge-Kutta time integration. The result of the analysis, displayed in Fig.3.9, 3.10, shows the convergence of the Lorenz

system to the correct values for embedded dimension $d_E \geq 3$. When the system is embedded in four or more dimensions, spurious negative exponents are calculated, indicating that the dimensionality of the system is 3 (dashed circles Fig. 3.10). The single positive exponent is a persistent feature and a direct indication of chaos.

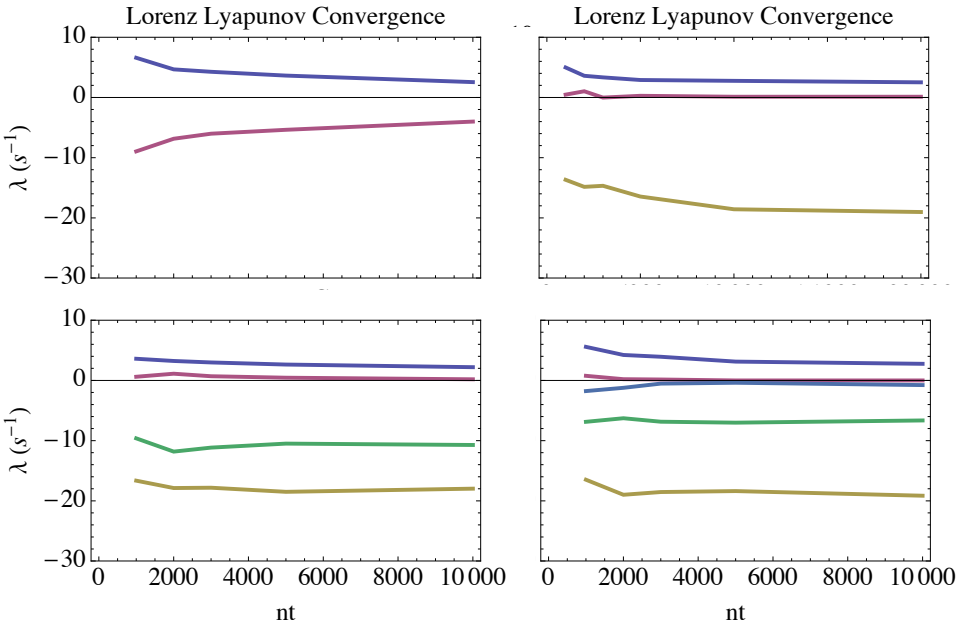

Figure 3.9: The convergence of the Lyapunov spectrum for the Lorenz system. The convergence is poor for $d_E = 2$, because the system is fundamentally three-dimensional. When $d_E > 3$, spurious negative exponents are created between the correct lowest exponent and zero.

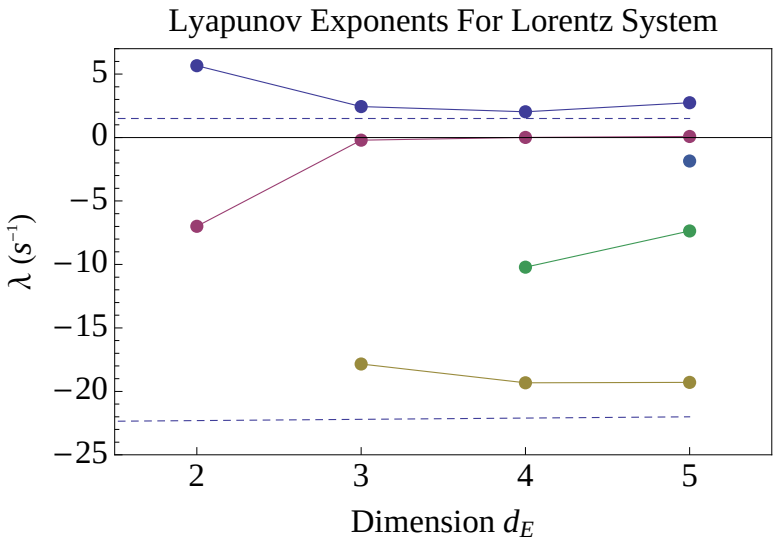

Figure 3.10: The Lyapunov spectrum for embedded dimension $d_E = [2, 5]$ for the Lorenz system.

3.8 Inverting the Continuity Equation

When density measurements are taken at multiple spatial points, the plasma flow can be determined by the time-rate of change of density and the continuity equation,

$$\frac{\partial N}{\partial t} + \nabla \cdot (N\mathbf{v}) = 0 \tag{3.31}$$

where $N = \langle n \rangle \delta V$ is the flux-tube integrated density, and $\mathbf{v} = (\mathbf{B} \times \nabla\Phi)/B^2$. The continuity equation becomes

$$\frac{\partial N}{\partial t} - \frac{\partial \Phi}{\partial \psi}\frac{\partial N}{\partial \varphi} + \frac{\partial \Phi}{\partial \varphi}\frac{\partial N}{\partial \psi} = 0 \tag{3.32}$$

The right-hand side of this equation can be supplemented with sources by ionization, as well as losses.

In CTX, the polar imager measures density $N(\varphi, \psi, t)$, and therefore the spatial and temporal derivatives of N can be easily calculated. This reduces the problem to an $\mathcal{A}\mathbf{x} = \mathbf{b}$ problem of the form

$$\left(-\frac{\partial}{\partial \psi}\frac{\partial n}{\partial \varphi} + \frac{\partial n}{\partial \psi}\frac{\partial}{\partial \varphi} \right)\Phi = -\frac{\partial N}{\partial t} \tag{3.33}$$

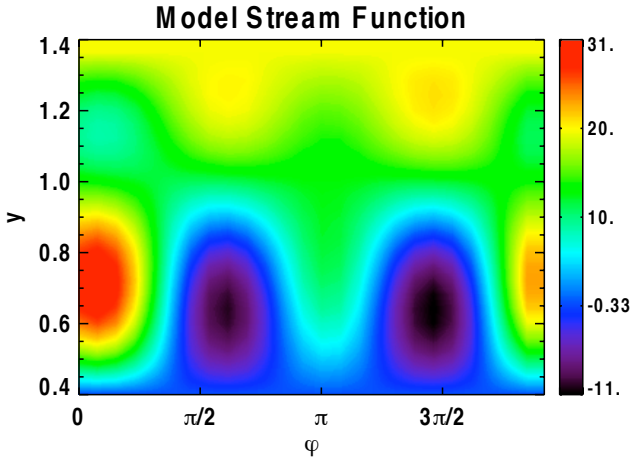

Figure 3.11: A model stream function Φ for advecting a density field. The model is defined on the domain (φ, y) where y is normalized magnetic flux $y = \psi/\psi_0$.

where the operator $(\ldots)$ needs to be inverted. This is done using a basis function expansion, and solving for $\Phi(\varphi, \psi, t)$ in a least-squares sense at each time point

$$\begin{aligned}\Phi(\varphi,\psi) &= C\frac{\psi-\psi_{min}}{\psi_{max}-\psi_{min}} + \sum_n D_n \sin\left(n\pi\frac{\psi-\psi_{min}}{\psi_{max}-\psi_{min}}\right) \\ &+ \sum_{m,n}\left[A_{m,n}\sin(m\varphi) + B_{m,n}\cos(m\varphi)\right]\sin\left(n\pi\frac{\psi-\psi_{min}}{\psi_{max}-\psi_{min}}\right) \qquad (3.34)\end{aligned}$$

with calculated coefficients $A_{m,n}, B_{m,n}$ representing convective cells and D_n, C representing zonal flow and rigid rotation, respectively. Once Φ has been calculated, the velocity which caused the motion from t to $t + \delta t$ is obtained from spatial derivatives.

As a test of the accuracy of the inversion, a model stream function has been prescribed in Fig.3.11. This stream function acts to advect a model density function $n(\varphi, \psi)$ in time. Rigid rotation is included in this model. By using the time evolution of the density (Fig.3.12), the stream function which caused that motion is obtained by inverting the continuity equation in a least-squares sense. The time-rate of change of density displays which regions in (φ, ψ) space there is a gain and loss of density. The long-time modification to the density field is shown in Fig.3.13 where the effects of the flow field can be easily seen.

By inverting the continuity equation for Φ, the model stream function, solution, and

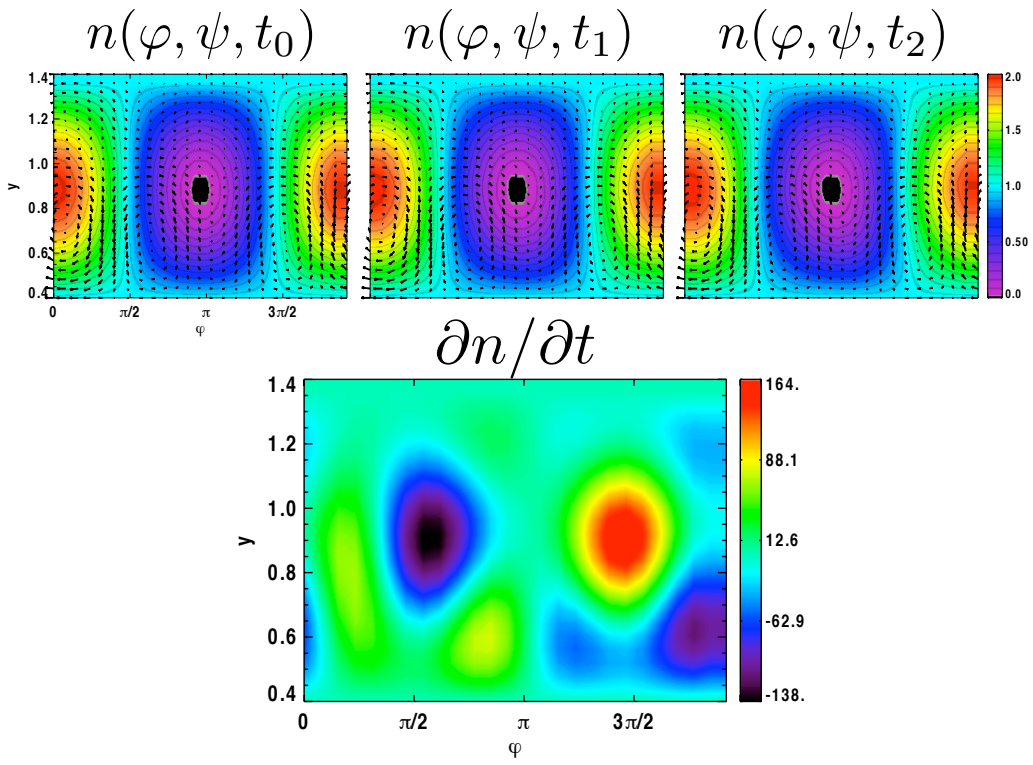

Figure 3.12: Three time steps of the advection of the density field. Vector flow fields are overplotting to indicate the direction of motion. The approximate time-rate of change of density from the time-centered finite difference.

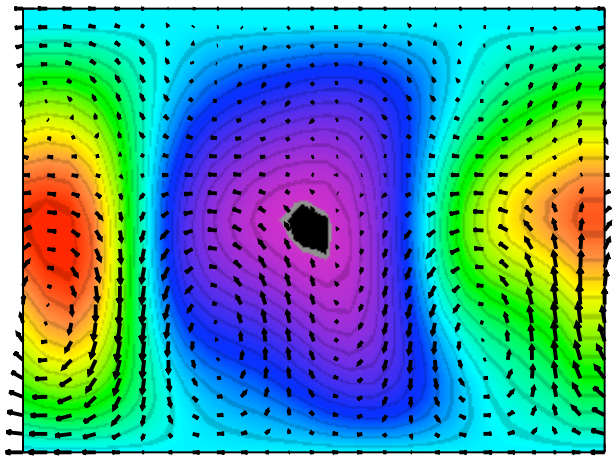

Figure 3.13: The density field after 10 time-steps of advection.

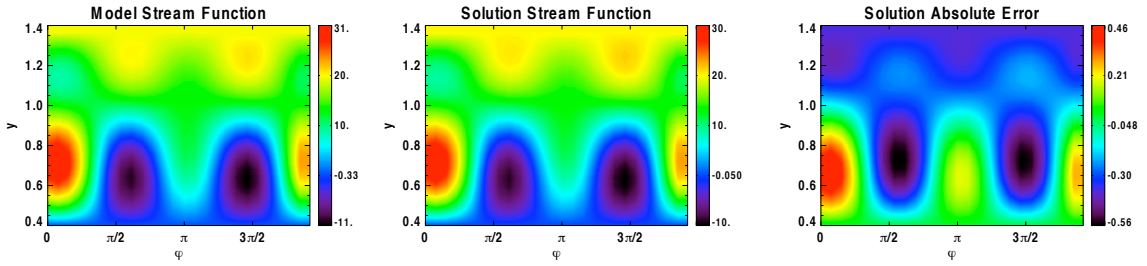

Figure 3.14: The model, solution, and absolute error for the inversion of the continuity equation. The relative 2-norm error integrated over the domain is about 2%.

error between the model and solution are shown in Fig.3.14. The absolute point-wise error is relatively small, having amplitude 0.1 on a stream function with amplitude 40. The relative 2-norm error $\sum_{i,j} |\Phi - \hat{\Phi}|/|\Phi|$ is typically 2-5%, showing good agreement between the model and the solution. When using real data, it is necessary to low-pass filter the time records to eliminate the jitter associated with high frequency noise. The high frequency noise corrupts the time-rate of change of density, leading to a large $\partial N/\partial t$ not arising from cross-field motion.

3.9 Spectral Energy Transfer

In a rotating plasma, as in CTX, the direction of spectral energy flow can be calculated from two closely spaced probes separated in an upstream/downstream orientation [71, 72]. This method and modifications of this method [48, 9] have been used in toroidal devices [89, 90, 61, 70] for investigating the direction of nonlinear energy transfer. The model equation for the dynamics is given as a simple wave equation

$$\frac{\partial \phi(k,t)}{\partial t} = \Lambda_L(k)\phi(k,t) + \frac{1}{2}\sum_{\substack{k_1,k_2 \\ k=k_1+k_2}} \Lambda_Q(k_1,k_2)\phi(k_1,t)\phi(k_2,t) \tag{3.35}$$

$$\Lambda_L(k) = \gamma(k) + i\omega(k) \tag{3.36}$$

where the linear coefficient Λ_L represents the growth and advection of the wave, and Λ_Q is the quadratic coupling coefficient. We would like to extract the linear and nonlinear coefficients, and this will be done by a finite-difference approximation for the time derivative. We represent $\phi(k,t)$ by a amplitude and phase

$$\phi(k,t) = |\phi(k,t)|e^{i\Theta(k,t)} \tag{3.37}$$

and

$$\frac{\partial \phi(k,t)}{\partial t} = \lim_{\tau\to 0}\left(\frac{|\phi(k,t+\tau)| - |\phi(k,t)|}{\tau}\frac{1}{|\phi(k,t)|} + i\frac{\Theta(k,t+\tau)-\Theta(k,t)}{\tau}\right)\phi(k,t) \tag{3.38}$$

Using Eq.3.37 in Eq.3.38, we have

$$\phi(k,t+\tau) = \frac{\Lambda_k^L\tau + 1 - i[\Theta(k,t+\tau)-\Theta(k,t)]}{e^{-i[\Theta(k,t+\tau)-\Theta(k,t)]}}\phi(k,t) + \frac{1}{2}\sum_{\substack{k_1,k_2 \\ k=k_1+k_2}} \frac{\Lambda_k^Q(k_1,k_2)\tau}{e^{-i[\Theta(k,t+\tau)-\Theta(k,t)]}} \times \phi(k_1,t)\phi(k_2,t) \tag{3.39}$$

It is Eq.3.39 which is modeled in Fourier space as a 'black-box' nonlinear system. The input $\phi(k,t)$ and output $\phi(k,t+\tau)$ represent spatially varying functions measured at two

different times, where τ is the small time change between the measurements. To see how this equation is derived, see Appendix C.

To simplify, and put a general mathematical context, we redefine

$$\begin{aligned} X_k &= \phi(k,t) \quad Y_k = \phi(k,t+\tau), \\ L_k &= \frac{\Lambda_k^L \tau + 1 - i[\Theta(k,t+\tau) - \Theta(k,t)]}{e^{-i[\Theta(k,t+\tau)-\Theta(k,t)]}}, \\ Q_k^{k_1,k_2} &= \frac{\Lambda_k^Q(k_1,k_2)\tau}{e^{-i[\Theta(k,t+\tau)-\Theta(k,t)]}} \end{aligned} \tag{3.40}$$

where $k = k_1 + k_2$. The equation Eq.3.39, using the symmetry relation can now be written as[1].

$$Y_k = L_k X_k + \sum_{k_1 \geq k_2} Q_k^{k_1,k_2} X_{k_1} X_{k_2} \tag{3.41}$$

The terms L_k and $Q_k^{k_1,k_2}$ are called the *linear* and *quadratic transfer functions*. Remember that Y_k represents X_k after X_k has been 'evolved' through a system with linear evolution and nonlinear mixing of spectral components. By multiplying Eq.3.41 by X_k^* and ensemble averaging, we get

$$\langle Y_k X_k^* \rangle = L_k \langle X_k X_k^* \rangle + \sum_{k_1 \geq k_2} Q_k^{k_1,k_2} \langle X_k^* X_{k_1} X_{k_2} \rangle \tag{3.42}$$

and by multiplying by $X_{k_1'}^* X_{k_2'}^*$ we get

$$\langle Y_k X_{k_1'}^* X_{k_2'}^* \rangle = L_k \langle X_k X_{k_1'}^* X_{k_2'}^* \rangle + \sum_{k_1 \geq k_2} Q_k^{k_1,k_2} \langle X_{k_1} X_{k_2} X_{k_1'}^* X_{k_2'}^* \rangle \tag{3.43}$$

The final term (fourth order moment) can be approximated as $\langle |X_{k_1} X_{k_2}|^2 \rangle$ by neglecting components with $(k_1, k_2) \neq (k_1', k_2')$. This is referred to the as the Millionshchikov hypothesis. It is widely used in weak and strong turbulence, but is only valid when the fluctuations are close to a Gaussian distribution. In CTX, the floating potential fluctuations are close to

[1] It is only necessary to compute these quantities for $k \geq 0$ and replace $\frac{1}{2}\sum_{k_1,k_2}$ with $\sum_{k_1 \geq k_2}$ due to the symmetry $Q_k^{k_1,k_2} = Q_k^{k_2,k_1}$. It is also sufficient to compute on a restricted domain due to the symmetry relations $X_k = X_{-k}*$ and $Q_k^{k_1,k_2} = [Q_{-k}^{-k_1,-k_2}]^*$.

Gaussian, with skewness ≤ 0.25, making this a valid approximation.

The linear and quadratic transfer functions can now be solved for, since

$$L_k = \frac{\langle Y_k X_k^* \rangle - \sum_{k_1 \geq k_2} Q_k^{k_1,k_2} \langle X_k^* X_{k_1} X_{k_2} \rangle}{\langle X_k X_k^* \rangle} \tag{3.44}$$

and

$$Q_k^{k_1,k_2} = \frac{\langle Y_k X_{k_1}^* X_{k_2}^* \rangle - L_k \langle X_k X_{k_1}^* X_{k_2}^* \rangle}{\langle |X_{k_1} X_{k_2}|^2 \rangle} \tag{3.45}$$

This represents two equations and two unknowns, which is solved for iteratively. The initial guess on the first iteration is Eq.3.44 neglecting the quadratic term. Once the solution is converged, the linear and quadratic coupling coefficients are given by Eq.3.42 where $e^{i[\Theta(k,t+\tau)-\Theta(k,t)]} \approx \langle Y_k X_k^* \rangle / |\langle Y_k X_k^* \rangle|$

As a test of the method, we define a linear and quadratic transfer function

$$\begin{aligned} L_k &= 1 - 4\frac{k^2}{k_N^2} + i0.8\frac{k}{k_N} \\ Q_k(k_1, k_2) &= \frac{i}{5k_N^4} \frac{k_1 k_2 (k_2^2 - k_1^2)}{1 + k^2/k_N^2} \end{aligned} \tag{3.46}$$

where $k = k_1 + k_2$, k_N is the Nyquist frequency, and $i = \sqrt{-1}$ shown in Fig.3.15. These model transfer functions represent the linear dispersion of a wave, and nonlinear coupling coefficient of the same form as the Hasegawa-Mima equation where high-k modes are coupled more strongly than low-k. A gaussian input signal of 150,000 points is passed through a black box five times using the output of the j^{th} box as the input to the $j + 1^{st}$ box, creating a non-Gaussian signal which has been evolved linearly and nonlinearly. We use X_k and Y_k as the input and output of the 5^{th} box. The method to solve for L_k and $Q_k^{k_1,k_2}$ outlined above has been used to solve for the transfer functions. The convergence of $Q_k^{k_1,k_2}$ is shown in Fig.3.16, and the results are shown in Fig.3.17.

Although the equation is given as a rate of change in time, we will be switching $\partial/\partial t \rightarrow \partial/\partial x$, or $\tau \rightarrow \Delta x$, and calculating the temporal growth and dispersion as a function

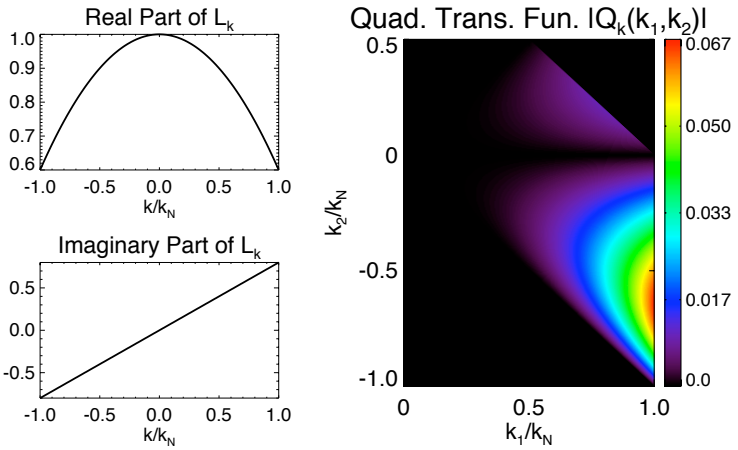

Figure 3.15: The model linear and quadratic transfer functions.

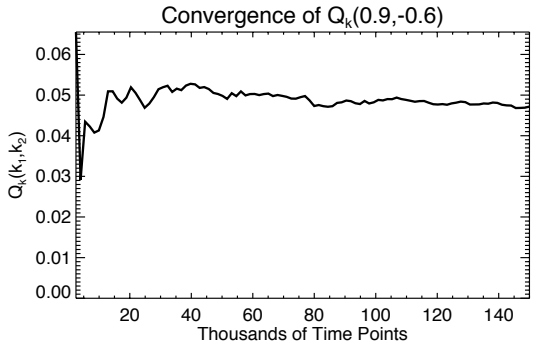

Figure 3.16: The convergence of the quadratic transfer function estimate.

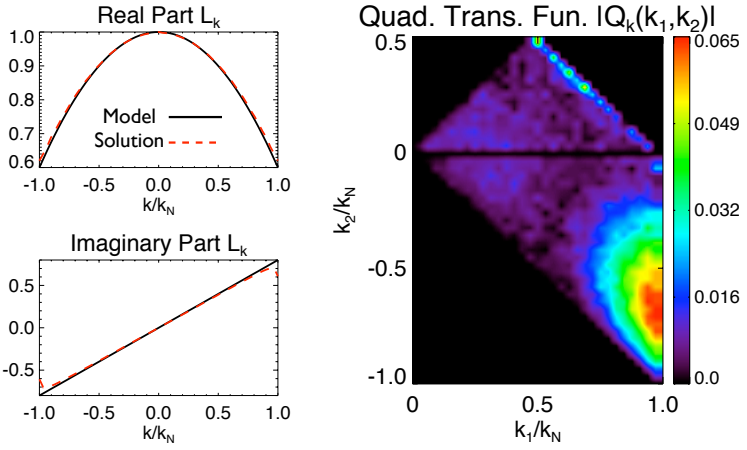

Figure 3.17: The model and converged solution functions L_k and $Q_k^{k_1,k_2}$. Good agreement is found between the model transfer functions and those calculated by the method.

of frequency. In other words, rather than using a diagnostic with high spatial resolution and comparing the fluctuating field at two times, we use two diagnostics with high temporal resolution, and compare the fluctuating signal at two points. This is valid when the wave dispersion $k(\omega)$ is approximately linear, and an *increasing* function of frequency.

3.10 Amplitude Correlation

The method for determining spectral energy transfer calculates the net transfer of spectral energy over the entire spectral region where there is significant power. Another method, the "amplitude-correlation" technique [20], allows selection of power bands of interest to investigate nonlinear coupling between portions of a turbulent spectrum. The concept is simple in that fluctuations are assumed to posses a time-evolving waveform which either increases or decreases in frequency or wavenumber. We will use a superposition of wave pulses to conduct a Monte Carlo simulation to determine in an average sense if a high or low frequency wave lags or leads a low frequency wave [68] (i.e. if an injection pulse evolves to a higher or lower frequency).

Consider the model pulse

$$\Psi(t) = \frac{1}{2}\sin(\omega_1 t)e^{-[(t-\zeta)/\Delta]^2} + \frac{1}{2}\sin(\omega_2 t)e^{-[(t+\zeta)/\Delta]^2} \tag{3.47}$$

and a time series which places this model pulse at time t_k where t_k is a uniformly distributed random time

$$\Phi(t) = \sum_{k=0}^{N-1} a\Psi(t - t_k) \tag{3.48}$$

where $N = \mu(t_{max} - t_{min})/nt$ and μ specifies the 'pulse density'. An example pulse for $a = 1,\ \zeta = -25,\ \Delta = 20,\ \mu = 0.1$ is shown in Fig.3.18 and displays a low to high frequency evolving pulse.

We wish to determine which frequency pulse happens first by selecting bands in the

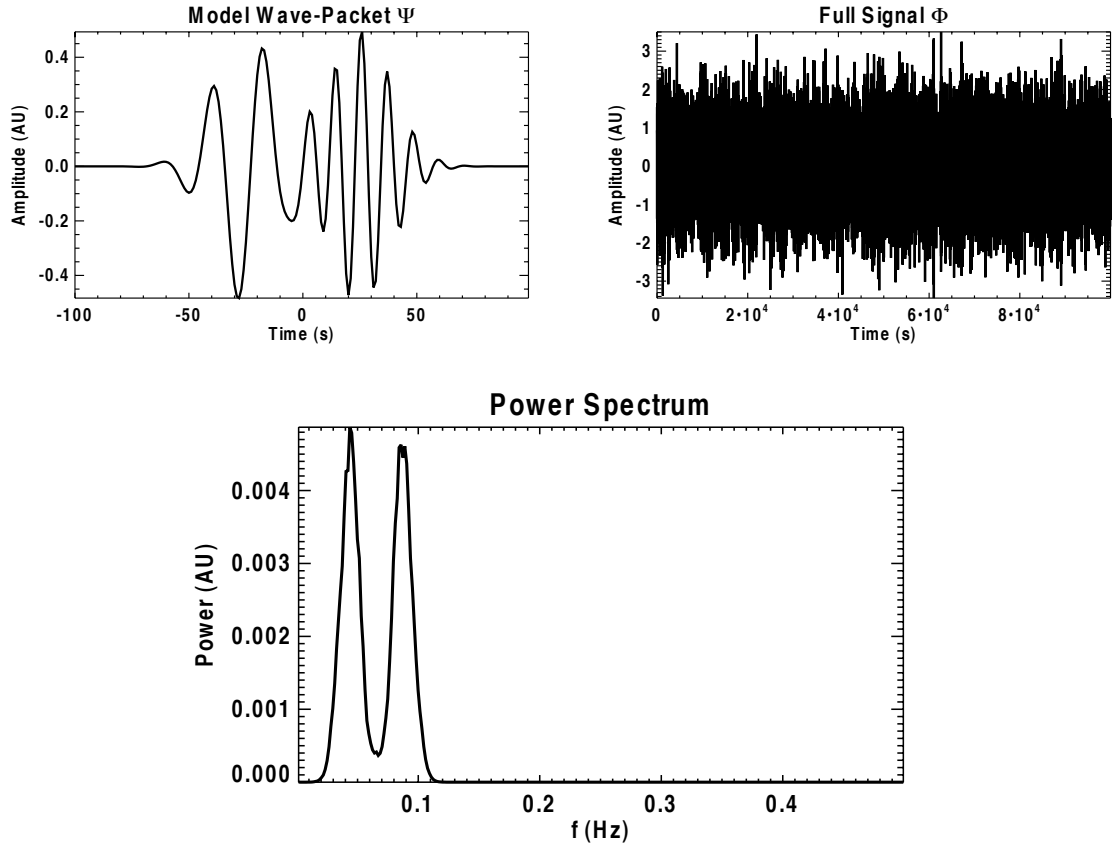

Figure 3.18: The model pulse which increases in frequency, full signal, and associated ensemble power spectrum. The model pulse has the low frequency leading the high frequency.

spectrum, and comparing the two signals associated with those bands. Once the model pulse has been created, a moving window of realizations of $\Phi(t)$ are compared. This is done by first band-passing the realization into two frequency domains of interest, here being bands labeled as dark and light grey (a),(b) in fig 3.20. Each individual realization is band-passed selecting the bands of interest and then back-transformed to the time domain, creating two time series from the realization. Then, the signals associated with those bands are low-pass filtered to extract the slowly varying amplitude information (see Fig.3.19). Those low-passed signals are cross-correlated. This is done for each realization of the time series Φ, and the ensemble cross-correlation function determines which band lags the other.

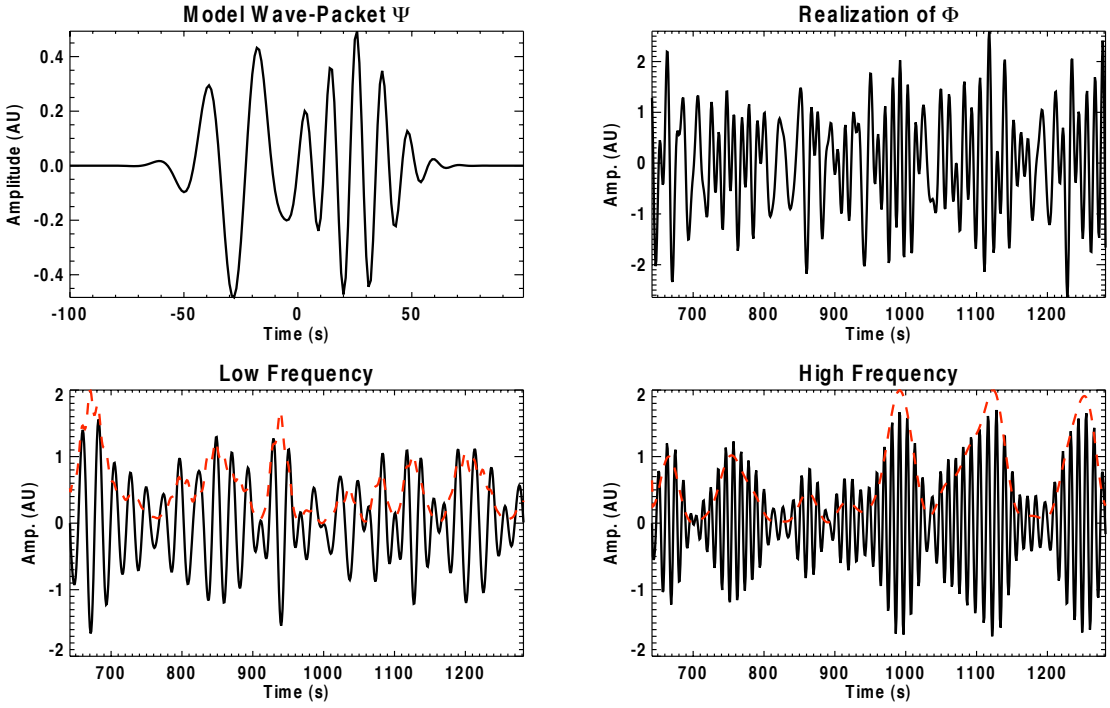

Figure 3.19: The model pulse Ψ and one realization $\Phi_{(i)}$ of the full signal $\Phi(t)$. The band-passed components of the realization are shown, as well as the low frequency amplitude variation (dashed red).

The results of the amplitude correlation analysis on the model pulse shown in Fig.3.18 are presented in Fig.3.20. The method accurately predicts the lag between pulses ($2\zeta = 50$), where cross-correlation between high and low frequency components $\langle C_{H-L}(\tau)\rangle$ having a *negative lag* correctly indicates that low frequency *leads* high frequency. The amplitude is

also quite near the predicted value of the cross-correlation amplitude of max[⟨ C_{H-L} ⟩] = 0.153] in Ref. [68].

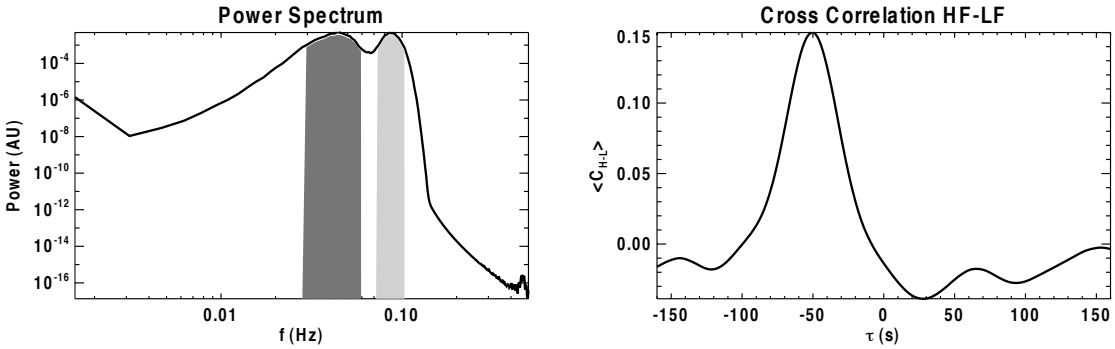

Figure 3.20: The frequency bands of interest and the high-low ensemble cross-correlation function. The high-low correlation function having a *negative lag* time indicates that the low frequency *leads* the high frequency.

A simple test of the validity of this result is to switch which frequency leads. The result from the same analysis is shown in Fig.3.21. Here, a different random number generation 'seed' has been used, otherwise the cross-correlation function will be a mirror image of that in Fig.3.18.

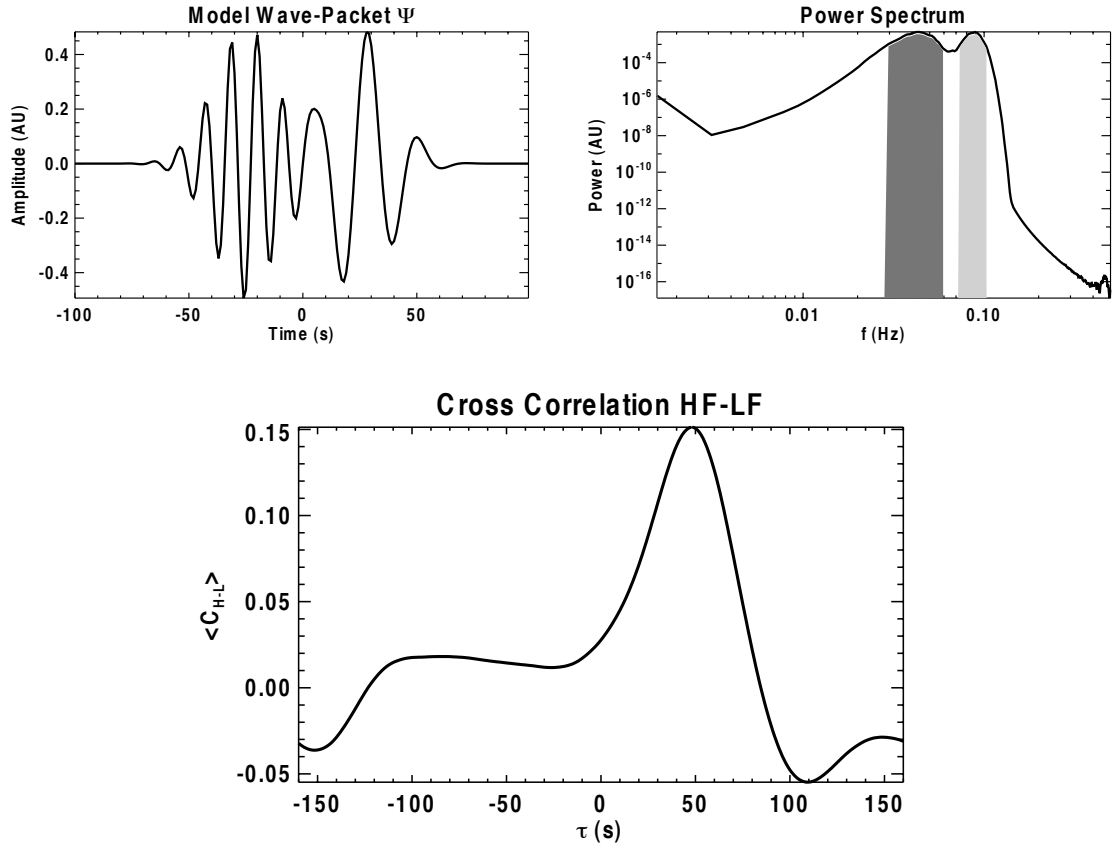

Figure 3.21: The reverse of the model pulse with the low frequency lagging the high frequency and associated spectrum. The cross-correlation function now displays a *positive lag* time at indicating that the low frequency *lags* the high frequency in time.

Chapter 4

Observation and Characterization of Turbulence in CTX

High density, turbulent plasma discharges in CTX are created in the manner of Ch.2 and analyzed by the methods detailed in Ch.3. The turbulent fluctuations are investigated with respect to both local and global paradigms. Locally, single-point measurements of potential and density provide the time series for auto-correlation analysis and ensemble spectra. Two-point measurements are used to measure the parallel wavenumber along a magnetic field line, as well as the azimuthal mode numbers of the spatial structure of the turbulence. The analysis of density fluctuations measured by the polar imager is done with the bi-orthogonal decomposition, and describes the structure and dynamics of the plasma on the global scale. The stream function, which determines the flow of plasma, uses spatial and temporal derivatives of density measurements obtained by the polar imager, and determines the global structure of the potential. The Lyapunov exponent analysis performed on density fluctuations investigates the chaotic nature of the temporal variation of the global structures in the plasma. Finally, the analyses for nonlinear mode interaction and power transfer are performed on turbulence measurements in CTX.

4.1 Single-Point Measurements

Using a movable probe, single-point measurements of density and potential have been taken across the accessible radius of CTX. Turbulence measurements motivate statistics which are "ensemble averaged" over a time where the basic plasma parameters and profiles are relatively stationary. Because of the high reproducibility of plasma discharges in CTX ensemble averages of fluctuations can be calculated over an entire discharge (~0.7 s) and over multiple discharges, creating well-converged statistics.

4.1.1 Auto-Correlation Function

The auto-correlation function in time for density fluctuations, and its associated ensemble are displayed in Fig.4.1. The function $\langle C(\tau)\rangle$ is seen to decay quickly, reducing in amplitude to half in approximately 20 microseconds. Note that the function is not purely decaying, and reverses sign twice within a lag time of 200 microseconds. This sign reversal is a first indication of periodicity, or quasi-coherence in the time series. The ensemble auto-correlation for potential is also displayed in Fig.4.1, and displays a stronger periodic character, indicating that the potential fluctuations may be more coherent, with a more pronounced spectral peak. The auto-correlation time τ_c for density and potential are approximately 50 μs and 60 μs, respectively. The auto-correlation function for potential fluctuations measured across the plasma radius is shown in Fig.4.2, and computed over a much longer time window, extending the τ-axis. The variation in the auto-correlation function across the accessible plasma radius indicates two modes at a high and low frequency with *long-range* correlation. The low frequency mode which exists near $1/\tau \sim 1.6$ kHz is most strongly correlated closer to the center of the plasma where the heating resonance exists. The higher frequency mode near $1/\tau \sim 2.5 - 3$ kHz is more strongly correlated at the plasma edge. The high frequency mode has a radial dependence on its frequency near the edge of the device ($L > 57$ cm), indicating a slight shear in the rotation.

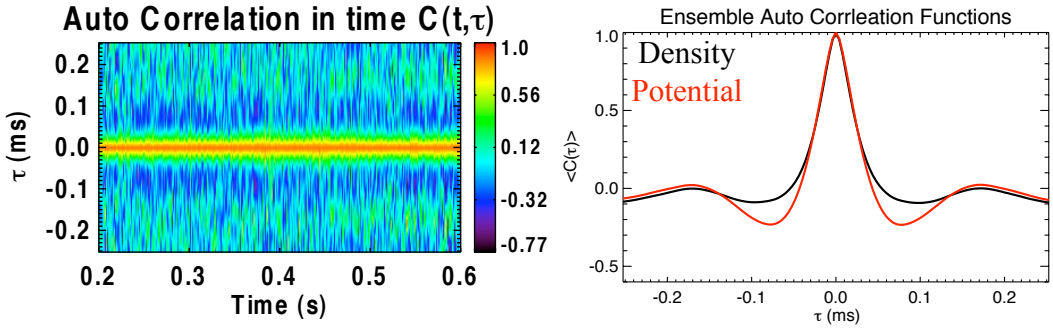

Figure 4.1: The auto-correlation function in time, and the time-integrated (ensemble) auto-correlation function for density and potential fluctuations. The potential displays more periodic behavior.

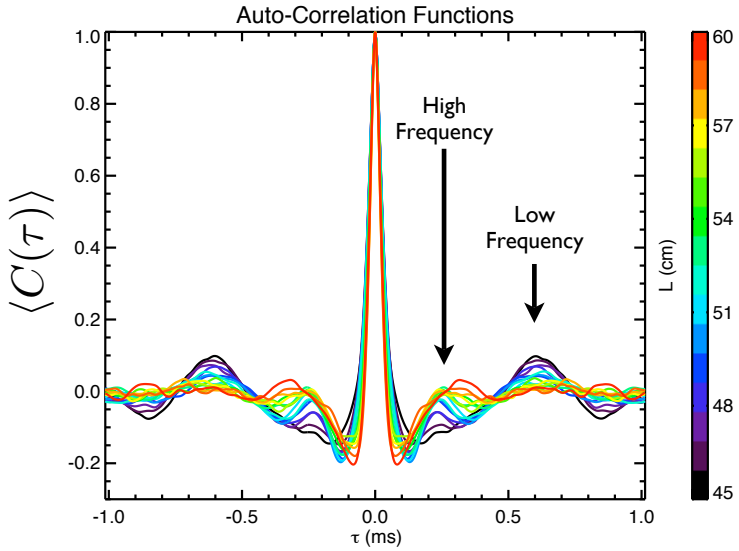

Figure 4.2: The auto-correlation function across the accessible plasma radius indicating two modes at a high and low frequency with long-range correlation. The low frequency mode is most correlated closer to the heating location. The high frequency mode is more strongly correlated at the plasma edge. The high frequency mode has a radial dependence.

4.1.2 Ensemble Spectrum

Using a single floating potential probe, and systematically inserting the probe from the plasma edge closer to the heating location, the ensemble spectrum of the fluctuating potential is measured. The ensemble spectra of potential across the plasma radius from $L = 44$ to 58 cm is given in Fig. 4.3, where each spectral trace represents an ensemble over hundreds to thousands of realization and converged over multiple plasma discharges. The spectrum can be seen to follow a power-law for $f \geq 10$ kHz with a trend approximated by f^{-5}. There also exist spectral peaks in the ranges $f \sim 1-2$ kHz and $f \sim 4-6$ kHz, which will later be identified as quasi-coherent $m = 1, 2$ modes, respectively, where m is the azimuthal mode number of potential fluctuations.

The spectra of density fluctuations are also measured by the same single-probe technique. Although both the potential and density exhibit power-law trends, the density follows a more shallow trend of f^{-3}. The interpretation of these differing power-law slopes will be discussed in Sec.4.8

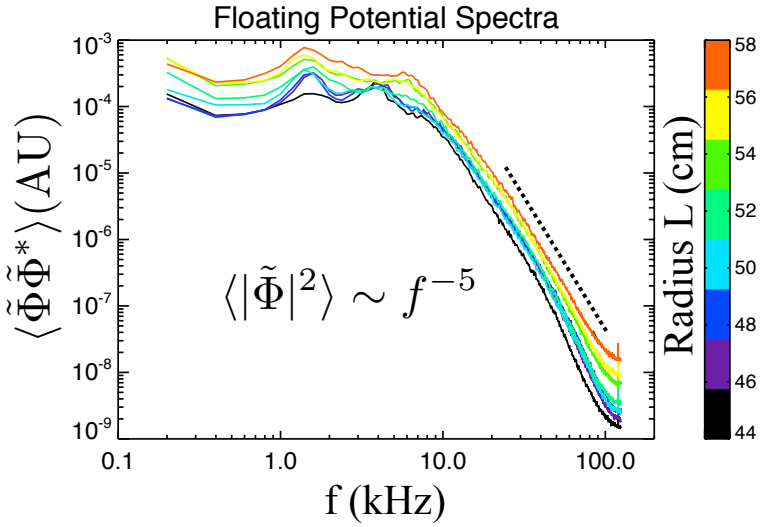

Figure 4.3: The ensemble-averaged floating potential spectra taken across the plasma radius, L. The dashed line indicates f^{-5} for reference.

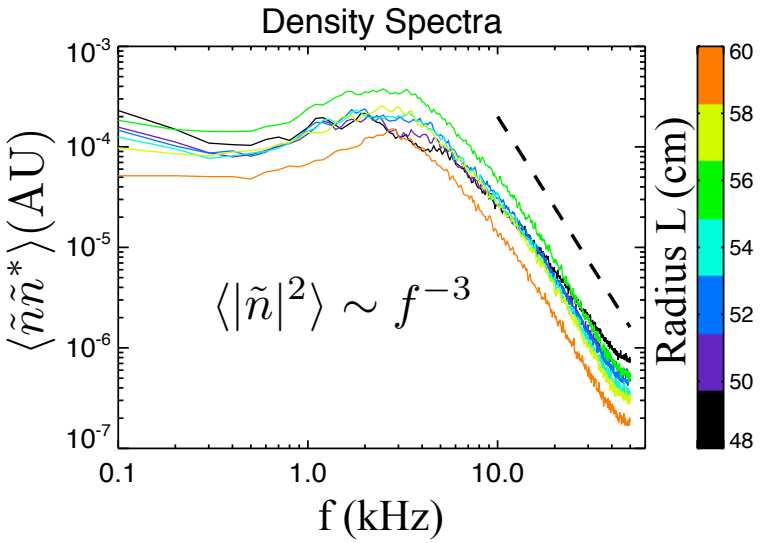

Figure 4.4: The ensemble-averaged density spectra taken across the plasma radius, L, by a Langmuir probe. The dashed line indicates f^{-3} for reference.

4.2 Two-Point Measurements

Using two or more diagnostics, cross-correlation, coherence and phase are the statistical tools for determining the correlation length and time of the fluctuations, as well as the coherence and spatial structure of quasi-coherent modes. The spatial structure interpretation is dependent on the distance, or periodic angle difference, between the probes. The phase shift in radians satisfies $\alpha = k\Delta x$, where k is the wavenumber, and Δx is the distance separating the probes. When azimuthal mode number m is used to describe a mode, then that mode posses a $\sin(m\varphi)$, periodic structure.

4.2.1 Parallel Wavenumber

When two diagnostics are positioned on a field-line, the parallel wavenumber can be measured by computing the phase shift, and the frequency integrated cross-phase. Two probes are used separated by $\Delta s \approx 35$ cm, the separation on a field line. One probe is fixed at $L = 50$ cm, and another probe moves radially from $L = 60$ cm to L =45 cm ($\Delta L = [10 \rightarrow -5]$ cm). Examination of floating potential fluctuations when two diagnostics

are aligned along the field shows very little difference between the signals themselves, the signals have a zero-lag. There is significant cross-coherence up to 40 kHz Fig.4.5. Although the signals may appear identical, the cross-phase and frequency-integrated cross-phase are still necessarily calculated. The integrated cross-phase weights the phase function to the coherence, providing a more accurate average cross-phase over the entire spectrum. The mean cross-phase is taken at the maximum cross-coherence. The integrated cross-phase $\langle \alpha_{1,2} \rangle_{\int} = k_{\parallel} \Delta s$ between these two diagnostics has been calculated over the duration of each discharge, and displays $k_{\parallel} \approx 0$. The cross-phase at maximum coherence also confirms $k_{\parallel} \approx 0$, but does display some phase shift when $\Delta L \neq 0$. The phase shift for determining $k_{\parallel}$ is displayed in Fig.4.6.

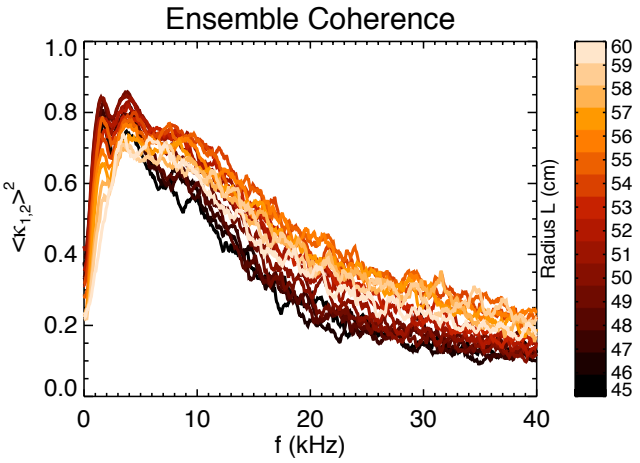

Figure 4.5: The ensemble cross-coherence for diagnostics positioned near the same field-line. The color indicates the radial location of the moving probe.

4.2.2 Correlation Length

Using probe pairs separated by a distance Δx, cross-correlation of fluctuations in a rotating plasma can yield the correlation length in the laboratory frame. The cross-correlation function is illustrated in Fig.3.1. The cross-correlation function for probes separated by $\Delta\varphi = 9°$ ($\Delta x \approx 8$ cm) is shown in Fig.4.7. There is very strong correlation $\langle C_{1,2} \rangle \geq 90\%$.

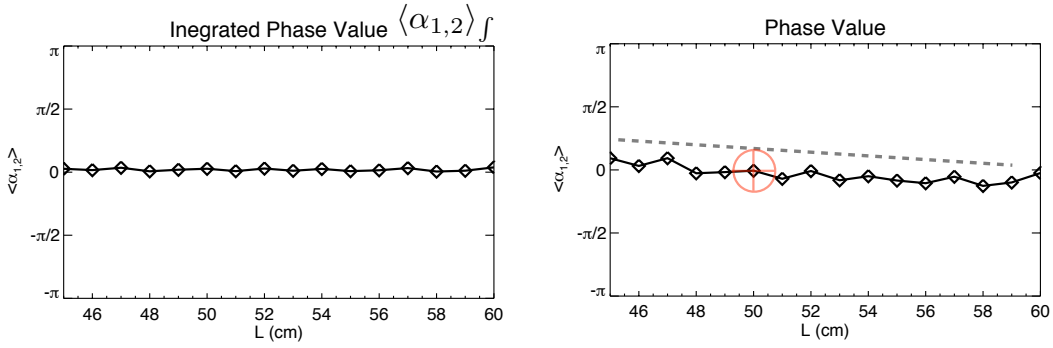

Figure 4.6: The parallel phase shift $\langle\alpha_{1,2}\rangle_\int = k_\parallel \Delta s$ across the accessible plasma radius is essentially zero, as expected from interchange modes. The mean cross-phase shows that the phase shift is zero for $\Delta L = 0$ at L=50 cm.

The lag time is $\tau_{Lag} \approx 15\ \mu$s, indicating the fluctuations propagate at $v_\varphi \approx 6$ km/s. The strong correlation indicates that very little turbulence exists on these spatial scales to decorrelate the structures passing between the probes.

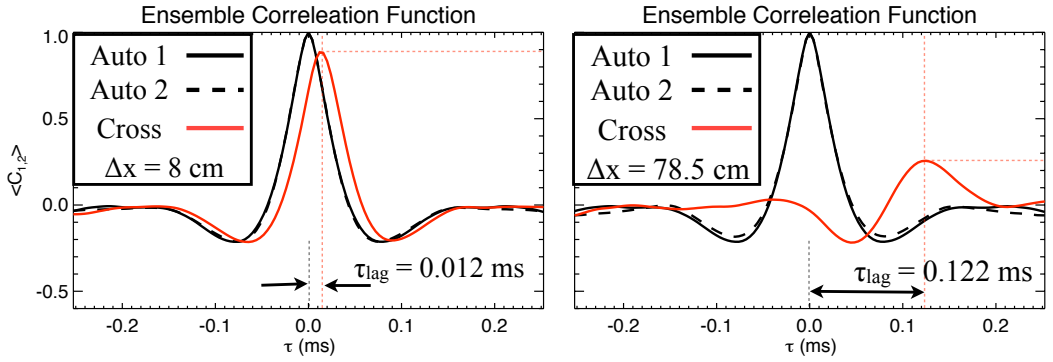

Figure 4.7: The ensemble auto-correlation functions and cross-correlation between probes separated by $\Delta x = 8$ cm and $\Delta x = 78.5$ cm. The auto-correlation functions are essentially identical. Strong correlation is found at $\Delta x = 8$ cm, indicating that very little turbulence exists on this spatial scale. The lag time increases in proportion to spatial separation indicating rigid rotation at radius $L = 50$ cm.

Using probes separated by $\Delta\varphi = 9°, 90°, 180°$, the correlation length of fluctuations has been measured. As the probe separation is increased, the lag time τ_{lag} increases in proportion (Fig.4.7), representing a constant azimuthal propagation speed of $v_\varphi \approx 6$ km/s. The correlation amplitude of the fluctuations decreases with probe separation as $\exp(-\Delta x/\lambda_c)$, where

λ_c ~45 cm, or 14% of the device circumference. The short correlation length relative to circumference represents the incoherent structures evolving quickly compared to a rotation period around the device. These incoherent structures decorrelate in a time approximately $\lambda_c/v_\varphi \approx 75\ \mu s$.

4.2.3 Azimuthal Mode Structure

When probes are separated azimuthally by $\Delta\varphi$, azimuthal modes can be identified by their phase shifts satisfying $\langle\alpha_{1,2}\rangle \sim m\Delta\varphi$ for $m = 1, 2, \ldots$. The results of cross-coherence and phase are shown in Fig.4.8. One potential probe was fixed at $L = 50$cm, and probes situated at azimuthal separations $\Delta\varphi = \pi/2,\ \pi$ were inserted into the plasma ($\Delta\varphi = \pi/2$ shown). The color of the trace indicates the location of the moving probe. The azimuthal coherence, calculated over thousands of realizations of each signal, reveals two quasi-coherent modes in the plasma. The dominant mode is found to have $m \sim 1$, as indicated by the value of the cross-phase where there is significant coherence. There also exists a sub-dominant $m \sim 2$ mode with weaker coherence. The variation in cross phase with radial position is indicative of a 'spiral' character to the mode structure and this feature can also be seen in the spatial mode structure returned by the bi-orthogonal decomposition of density fluctuations in Sec.4.6. It is significant that with probe separation of $\Delta\varphi = \pi/2$ ($\Delta x \sim 80$ cm) there is essentially zero coherence above $f \sim 6 - 8$ kHz. The turbulent structures at this frequency have completely de-correlated, and it is above this frequency range where the power spectrum assumes a full power-law decay.

The polar imager can be used to measure density fluctuations when the repeller grids are biased negatively to repel electrons (Sec 2.2.3). With repeller voltages exceeding ~ -80 V, the density fluctuations in the bulk plasma and the fluctuations of the polar current are strongly correlated (Fig.4.9). When the Langmuir probe and a polar detector are on the same field-line, the ensemble cross-correlation function is peaked at a zero-lag, with amplitude $\langle C_{\tilde{n},I_{polar}}\rangle \approx 50\%$. Detectors separated azimuthally are also correlated, but with a lag time

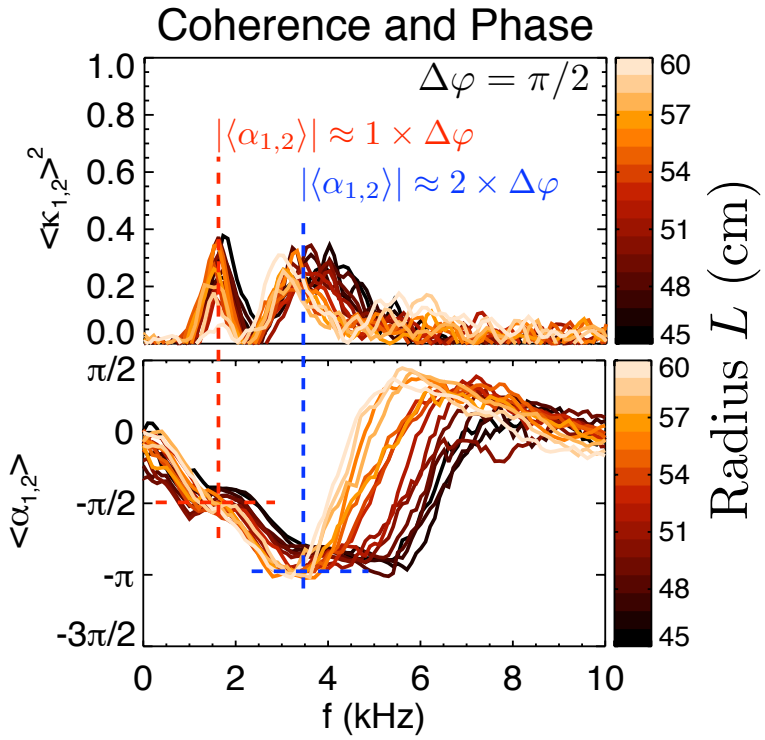

Figure 4.8: Structure of potential fluctuations displaying $m = 1$ and $m = 2$ azimuthal modes. Here the phase shift of $-\pi/2$ just below 2 kHz indicates an $m = 1$ mode. The phase shift of π near 3-4 kHz indicates $m = 2$. The probes are oriented in such a way that a negative phase shift indicates propagation in the $-\hat{\varphi}$ direction.

proportional to the azimuthal separation. Furthermore, the correlation amplitude decreases with azimuthal separation, as expected in a turbulent plasma. Therefore, when biased negatively, the polar imager can be used to image the density fluctuations in the entire plasma with good spatial resolution and excellent temporal resolution.

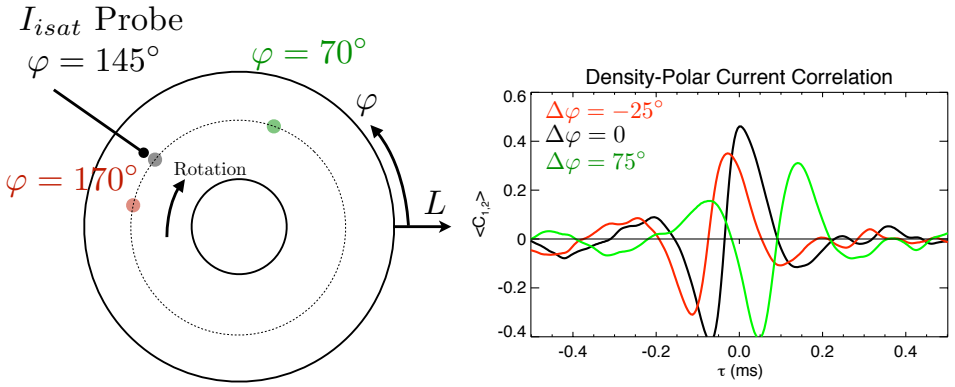

Figure 4.9: Experimental configuration and ensemble cross-correlation functions between density measured in the bulk plasma and polar current biased to measure density.

The correlation of density fluctuations at the pole between detectors is provided in Fig.4.10. The cross-correlation of density fluctuations reveals that plasma rotation occurs in the $-\hat{\varphi}$ direction, as indicated by the positive lag time for a detector situated at $\varphi < \varphi_{ref}$. By plotting the lag time as a function of detector separation $\Delta x = L\Delta\varphi$, the rotation velocity is given as the inverse of the slope. It is seen that the velocity increases with increasing radius, with the frequency $f = v/2\pi L$ nearly constant around 1.5 kHz.

To view the structure of the density fluctuations, 11 polar detectors at one radial location have been selected and plotted as a contour in time and azimuthal angle shown in Fig.4.11(a). The contour plot readily displays the plasma rotation in the $-\hat{\varphi}$ direction. The angled 'stripes' represent coherent rotating structures, and the slope of the stripe is the rotation rate, here approximately 2 kHz. When the stripes are singly-periodic in angle, then the mode structure is $m = 1$, the lowest mode number in the periodic system. In Fig.4.11, a strongly coherent $m = 1$ mode is seen at time $t = 0.133$ s. At other times, higher mode structures are dominant. Fourier wavenumber analysis determines the dominant azimuthal mode number at each time

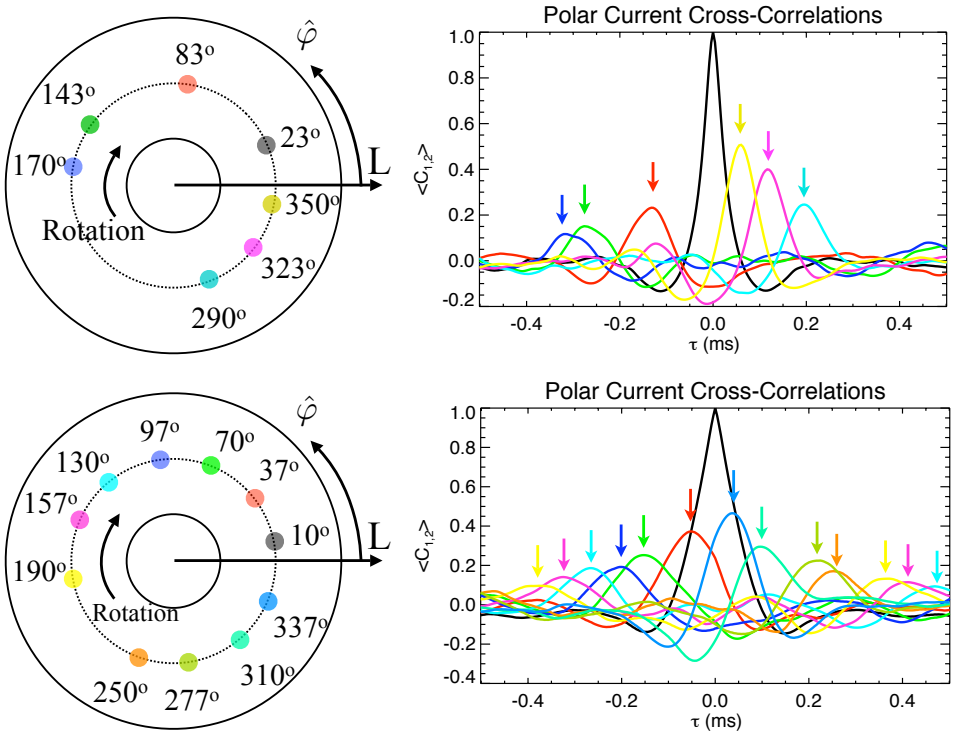

Figure 4.10: Experimental configuration and ensemble cross-correlation functions between density measured at multiple points from the polar imager at $L = 30, 35$ cm. The correlation amplitude decreases with separation of diagnostics. The positive lag between the reference detector and the others at decreasing angle indicates rotation in the $-\hat{\varphi}$ direction. The velocity is faster on the outboard side, giving a broad rotation rate near 1.5 kHz.

point, displayed in Fig.4.11(b). Modes number as high as $m = 5$ can be dominant, but the higher mode numbers are dominant for shorter durations. The variation in the dominant azimuthal mode number represents the merging (m decreasing) and splitting (m increasing) of coherent structures, or vortices, of plasma density.

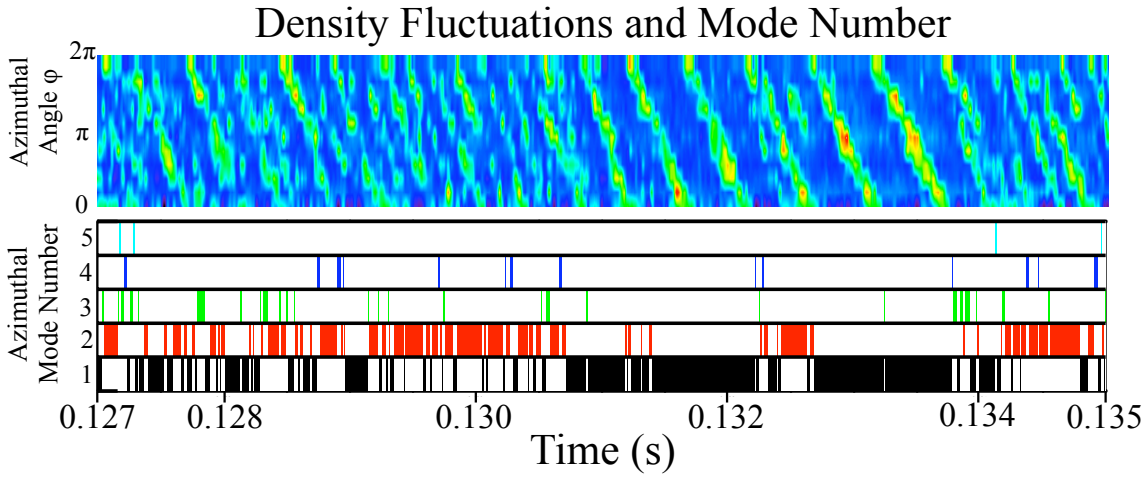

Figure 4.11: (a) Measurements of plasma density in time and azimuthal angle as well as (b) the dominant azimuthal mode number m. The angular stripes show plasma rotation at $f \approx 2$ kHz.

4.2.4 Comment on Transport

The measurements of auto- and cross-correlation functions and azimuthal mode structure are ensemble quantities, converged over the entire duration of a discharge. One may ask, what is the relationship between the fluctuations in potential and plasma density? This question addresses the fluctuation-induced particle flux caused by $\mathbf{E} \times \mathbf{B}$ motion [75, 13]. The radial $\mathbf{E} \times \mathbf{B}$ particle flux is[1]

$$\Gamma_r = \tilde{n}\tilde{v}_r = \tilde{n}\frac{\tilde{E}_\varphi}{B} = -\frac{1}{B}\tilde{n}\tilde{\Phi}k_\varphi \kappa_{\tilde{n},\tilde{\Phi}} \sin(\alpha_{\tilde{n},\tilde{\Phi}}) \tag{4.1}$$

[1] In these references the cross-phase convention switched conjugate, hence the negative sign.

which depends on the RMS values of fluctuating density and potential, the potential wavenumber $\tilde{E}_\varphi = -\nabla\tilde{\Phi} = ik_\varphi\tilde{\Phi}$, mutual coherence $\kappa_{\tilde{n},\tilde{\Phi}}$, and sine of the angle. These quantities are calculated in an ensemble sense. Therefore, when a positively going density fluctuation is followed by a positively going potential fluctuation where $-\pi/2 < \alpha_{\tilde{n},\tilde{\Phi}} < 0$, the radial flux Γ_r is positive and the density fluctuation is transported to the outboard, low-field side of CTX (Fig.4.12). Using reasonable parameters[2] at $L = 50$ cm, the numerical radial particle flux is near $10^{17}m^{-2}s^{-1}$, which is below typical measurements in TCV [32] ($\Gamma_r \sim 10^{20}m^{-2}s^{-1}$) which has much higher density, but nearer TORPEX [30] ($\Gamma_r \sim 10^{18}m^{-2}s^{-1}$), which has a radial variation in the sign of the flux.

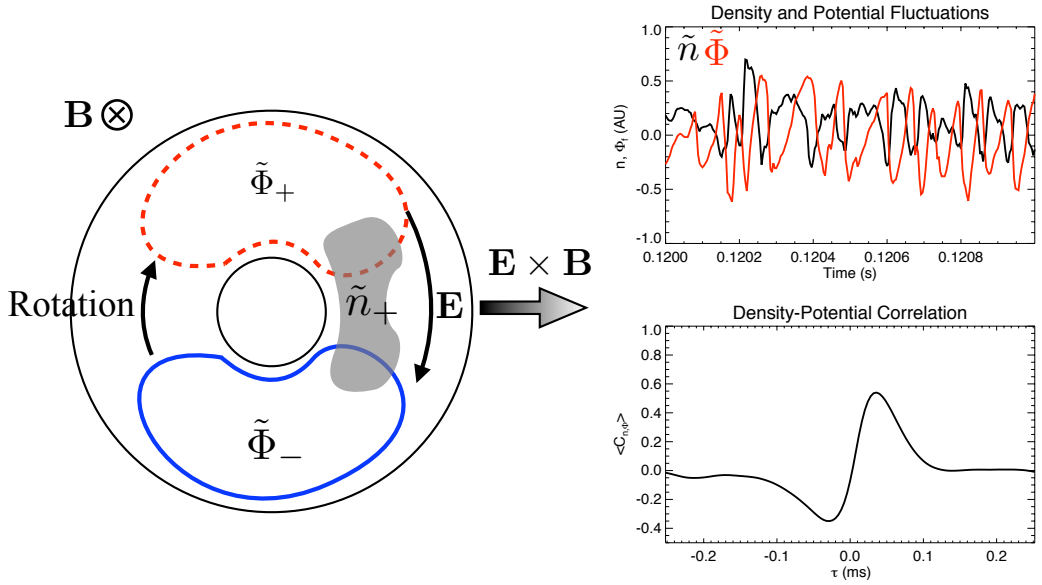

Figure 4.12: A schematic displaying the outward convection of a density perturbation by radial fluctuation induced flux. Signal samples of fluctuating density and potential (arb. units). Also, the ensemble cross-correlation indicating that positive potential perturbations lag higher density perturbations.

The transport is maximized when the phase is $\alpha_{\tilde{n},\tilde{\Phi}} = -\pi/2$. When the density fluctuations and potential fluctuations are exactly in phase or out of phase, then no fluctuation induced transport occurs, and the density circulates around potential contours without net transport. This is a convective cell which causes circulation, but not large amounts of

[2] $B \sim 0.014T, \tilde{n} \sim 3 \times 10^{15}m^{-3} \times 20\%, \tilde{\Phi} \sim 10\text{ V} \times 50\%$

particle transport. The tracked cross-phase in time, Fig.4.13, indicates that this relation is true on average, but deviations from the 90° cross-phase value occur often. The ensemble cross-correlation function also agrees with the cross-phase, as $\langle C_{\tilde{n},\tilde{\Phi}} \rangle$ has a positive lag, with coherence $\kappa_{\tilde{n},\tilde{\Phi}} \sim \max[\langle C_{\tilde{n},\tilde{\Phi}} \rangle] \sim 50\%$. The asymmetric probability density function ($pdf = (n - \bar{n})/\mathrm{var}(\tilde{n})$) of edge density fluctuations, possessing intermittency with a positive skewness, also supports these findings. The positive deviation from Gaussian skewness (Gaussian skewness = 0) indicates that positive density 'spikes' occur more often in the time series. The skewness of edge density fluctuations is near +0.25, which is small compared to typical tokamak 'blob' transport [96](s5.6), but closer to simulation results of 2D enstrophy conserving flows [88] having skewness 0.0-0.2. The skewness is increased in the presence of coherent structures. At the tokamak edge, intermittent transport events are observed through density fluctuations having skewness ≥ 1 or more. These are large amplitude coherent density 'blobs' which may be generated by interchange/ballooning or peeling/ballooning instabilities [3]. The process which generates these structures, and suppressing the high heat load associated with these intermittent transport events (ITEs) remains an active area of research. Inside of the separatrix, the skewness typically drops and can even change sign, representing rarified density fluctuations being more intermittent.

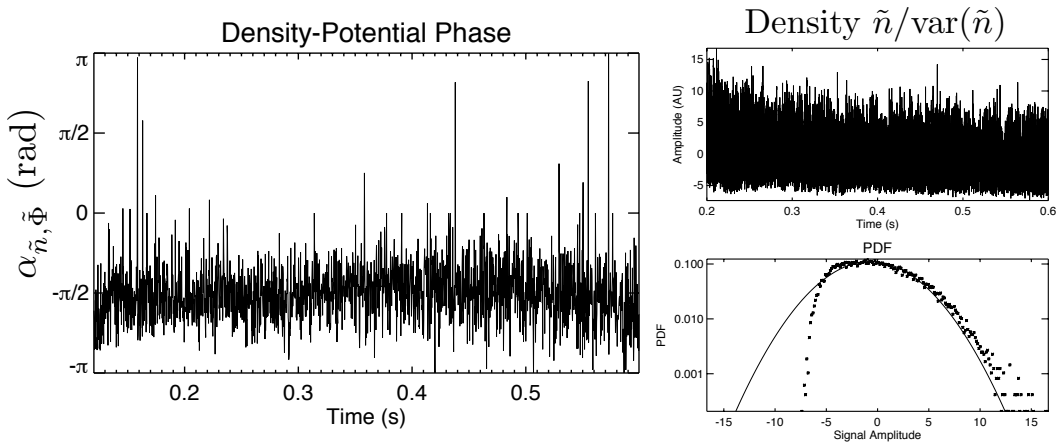

Figure 4.13: The density-potential tracked cross-phase, indicating that, on average, positive density fluctuations lead potential fluctuations by 90°. The probability density function for density fluctuations displaying positive skewness from Gaussian (solid line). The positive skewness indicates transport of high density perturbations to the outboard edge of CTX.

4.3 Stream Function

The potential structures which cause the plasma motion are dominated by an axisymmetric negative potential profile, and $m = 1, 2$ azimuthal modes, as determined by probe measurements in Sec.4.2. This suggests that the stream function which causes the plasma motion can be calculated by a model assuming low order azimuthal modes. By using multi-time measurements of the motion of plasma density measured by the polar imager, the stream function can be obtained by inverting the continuity equation with the model Eq.3.34.

A snapshot of the density evolution and potential is shown in Fig.4.14, and displays a radially broad density structure near $\varphi = \pi/2$. The time-rate of change is also calculated, and displays that this density structure is becoming more rarified for $\varphi > \pi/2$, and becoming more dense for $\varphi < \pi/2$. The structure is moving in the $-\hat{\varphi}$ direction. The stream function is then calculated over these three time steps, and displays a smooth, radially broad, $m = 1$ potential mode.

The stream function calculation is performed over 100 ms with a full two-dimensional density record digitized at 1 MHz. The mean coefficients of the basis function expansion

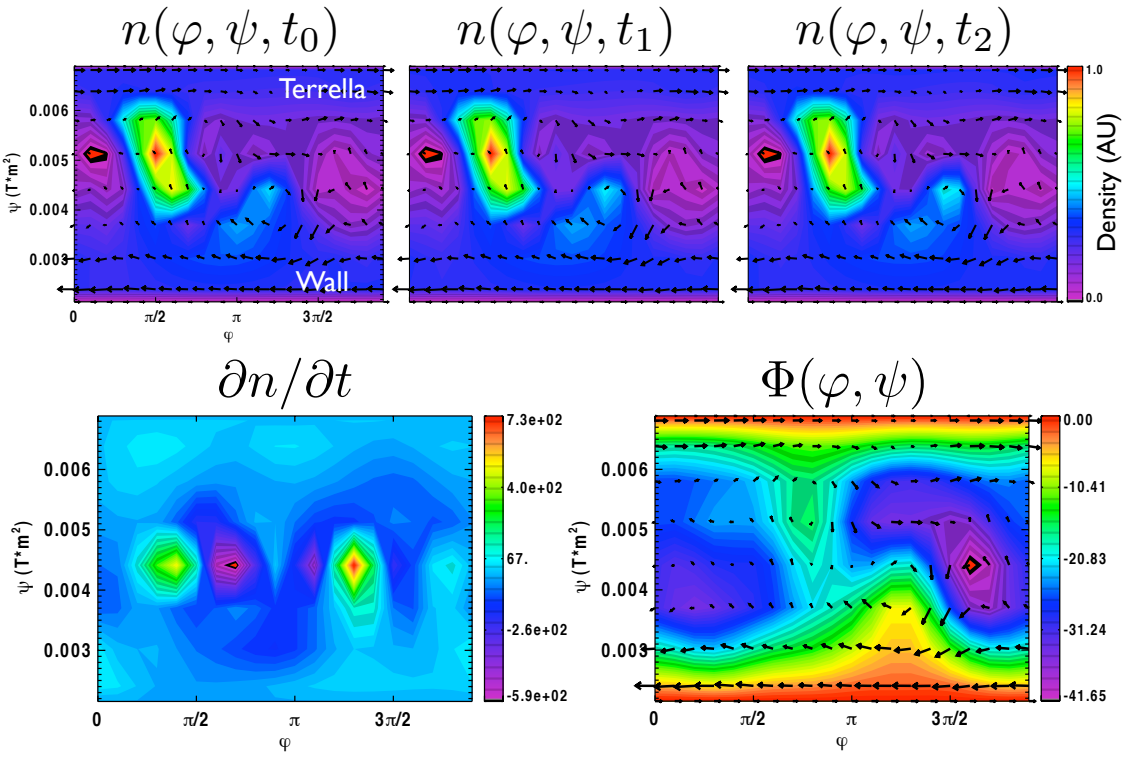

Figure 4.14: The density at three times, the associated time-rate of change of density, and the potential which caused the motion obtained from inverting the continuity equation. The outboard velocity is predominantly in the $-\hat{\varphi}$ direction.

$A_{m,n}, B_{m,n}, C, D_n$ averaged over this time gives the mean stream function, and the mean potential structure. Without allowing rigid rotation, t is found that the plasma motion is caused predominately by a radially broad negative potential causing rotation $\Omega_R = -\partial\Phi/\partial\psi$ in the $-\hat{\varphi}$ direction at 1-2 kHz. This is in agreement with the observed rotation seen in Fig.4.11, and probe measurements inside the plasma. When allowing rigid rotation, the dominant structure is $C \approx -30$ V, or rigid rotation at 1.3 kHz.

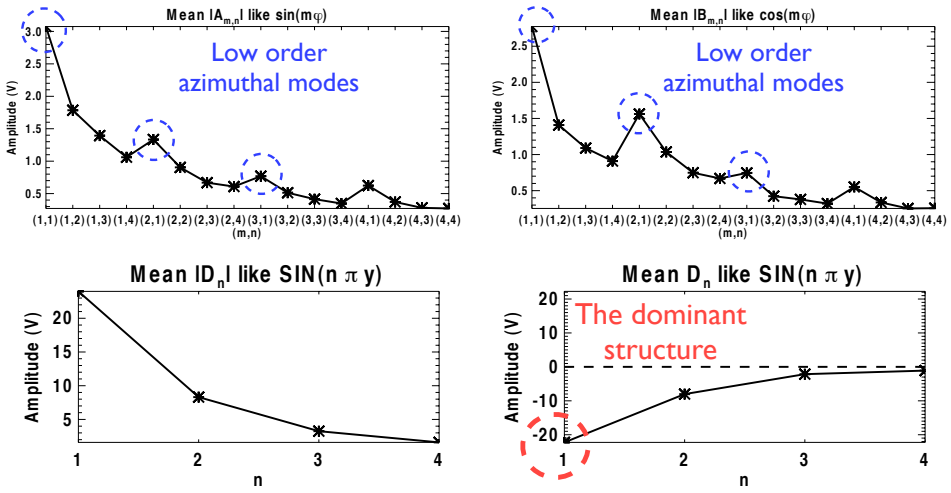

Figure 4.15: The coefficients of the basis function expansion for the potential. The global potential structure is dominated by a -20 V axisymmetric potential. The subdominant structures are radially broad (low n) $m = 1, 2, 3$ potential modes.

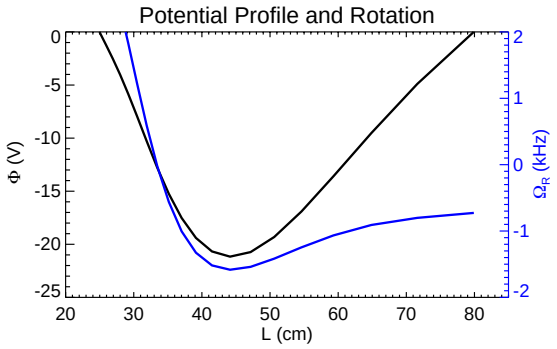

Figure 4.16: The potential calculated by inverting the continuity equation. The rotation calculated from the mean potential is in good agreement with the observed plasma rotation near $1 - 2$ kHz in the $-\hat{\varphi}$ direction.

A test of accuracy is the error from convecting the density ahead in time $n(\varphi, \psi, t_0) \rightarrow n(\varphi, \psi, t_0 + 2\delta t)$ with $\Sigma(\varphi, \psi, t_0)$, and comparing with the measured density field $n(\varphi, \psi, t_2)$. This difference is typically less than 10%. One cannot advance the density indefinitely, because the inversion is only accurate on the time scale of which the density is evolving, typically a few $\times \delta t$.

4.4 Fast Camera

The fast camera which has been installed on CTX produces time-integrated collected light at high frame rates, and with very high spatial resolution. When focused at the equatorial midplane, the radial resolution is 800 pixels over 40 cm. This provides high radial wavenumber resolution of 2 pixels/mm.

Due to the limit on the signal-to-noise ratio which decreases with frame rate, the fast camera is sequenced at 10,000 frames per second. This frame rate represents a tradeoff between collected light and temporal resolution.

Light intensity collected from the fast camera is well-correlated with density fluctuations, measured both in the bulk plasma and at the magnetic pole, shown in Fig.4.17. For these discharges, the fast camera was oriented to view the plasma over the region of $\varphi = [90 : 170]$ degrees, and across the plasma radius from the terrella to the wall. The Langmuir probe measuring density was located at $\varphi = 145°$, and the polar detectors are also in this range.

When the fast camera is focused on the equatorial plane with a narrow azimuthal angular span (Fig.4.18), and higher radial resolution, the radial light intensity profile and fluctuation profile can be calculated. Because the polar imager can view the entire plasma density, and fluctuations of light are well correlated with bulk density fluctuations and polar current fluctuations, comparisons between light emission measured by the fast camera and the polar current profile can be made. It is found that the radial light profile and radial density profile measured by the polar imager, seen in Fig.4.19, are in excellent agreement. The fluctuations

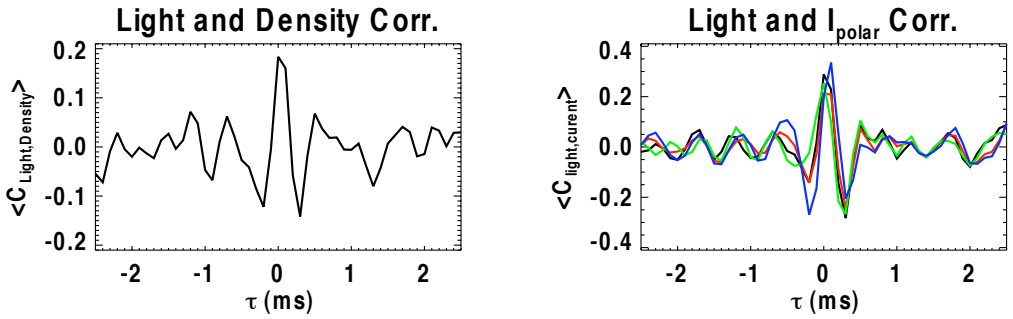

Figure 4.17: The cross-correlation between density fluctuations and light intensity (left) and between light and polar current (right) measured on field lines intersecting the equatorial plane where the fast camera is viewing. The cross-correlation is maximized at zero lag.

in light intensity peak near the heating zone at L=25 cm, and near L=40 cm, where the gradient is the strongest.

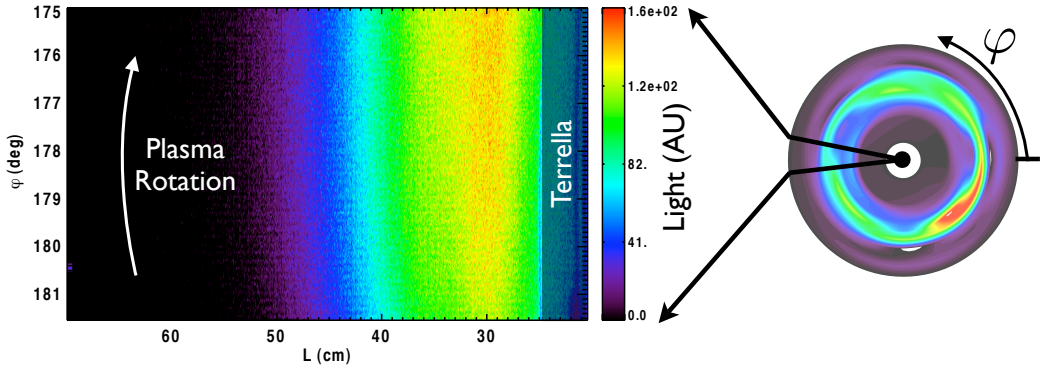

Figure 4.18: The view orientation of the fast camera for investigating radial profiles and radial wavenumber variation.

The density fluctuations are measured to be radially broad by the fluctuations in light intensity. By calculating the azimuthally integrated light fluctuation intensity in wavenumber space, it is seen that the radial structure is dominated by the lowest order radial mode.

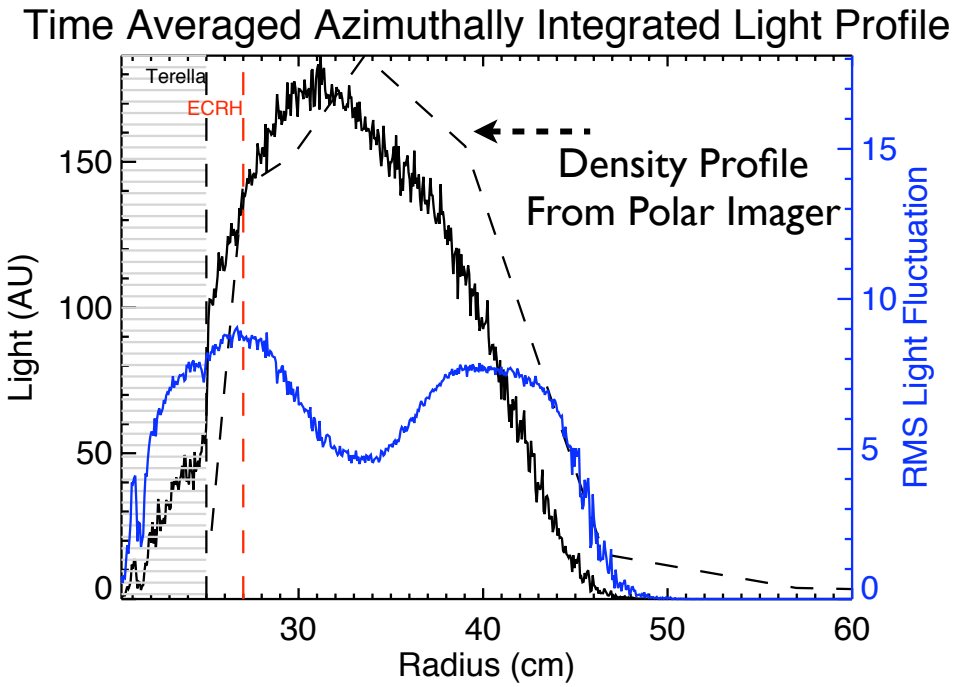

Figure 4.19: The radial profile of light intensity, and RMS fluctuation. Radial fluctuation amplitude is near 5%. The radial light intensity profile agrees with the radial density profile obtained from the polar imager (dashed).

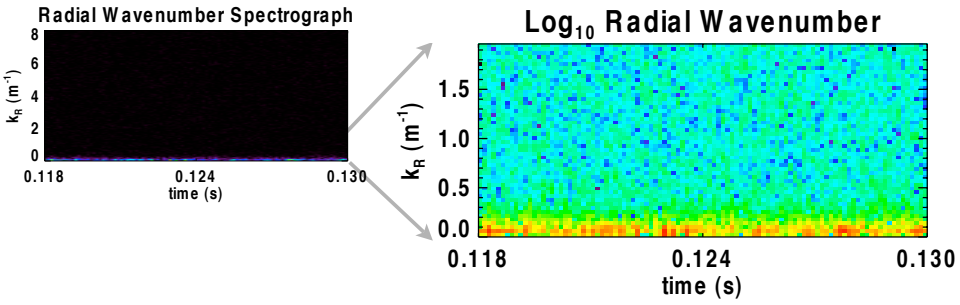

Figure 4.20: Spectrograph of radial wavenumber calculated from the the fluctuation images obtained from the fast camera. The radial wavenumber k_R is strongly dominated by the low wavenumber, indicating that the structures in the plasma are radially broad.

4.5 Hilbert Modal Decomposition

The modal decomposition based on the Hilbert transform (Sec.3.5) has been used on tokamaks [44] for investigation density and magnetic fluctuations. When the signals being analyzed often contain significant nonlinear or harmonic content, the Hilbert spectrum method can provide a cleaner representation of how the spectrum evolves in time, similar to a spectrogram. The density fluctuations measured by one of the gridded particle detectors at the pole of the CTX device has been decomposed by the Hilbert-Huang method and is displayed in Fig.4.21. The detector signal which is being analyzed is one which was used in creating Fig.4.11, where a coherent $m = 1$ mode is formed from higher mode numbers at times near 0.131 s and 0.133 s. In Fig.4.21, the formation of these coherent modes is associated with considerable 'instantaneous energy' in the time series at times t =0.128, 0.129, 0.131 and 0.133 s. Each time a coherent $m = 1$ mode is formed the signal energy is amplified, most easily seen at 0.131 and 0.133 s. Thus the coinciding of increased fluctuation energy and formation of large-scale structures is a phenomena consistent with an inverse cascade process.

The mode functions which are extracted from the density fluctuations are displayed in Fig.4.22 with the same vertical axis. The mode function (IMF) #5 is the most strongly correlated with the original time series, although IMFs 4-8 are all well correlated with correlation coefficient greater than 30%. At time t=0.131 s, the large amplitude $m = 1$ mode is seen on IMF #4. At time t=0.133 s the large amplitude $m = 1$ mode is seen on IMFs 5-8.

The Hilbert modal decomposition thus provides a novel representation of a complex time-varying quantity by a relatively small number of mode functions. The time series can then be visualized on the intrinsic time-scales present is the record, and existing near some average frequency. This representation is far simpler than an Fourier decomposition consisting of thousands of modes, with prescribed frequencies at their respective amplitudes, discretely spaced in the spectral domain.

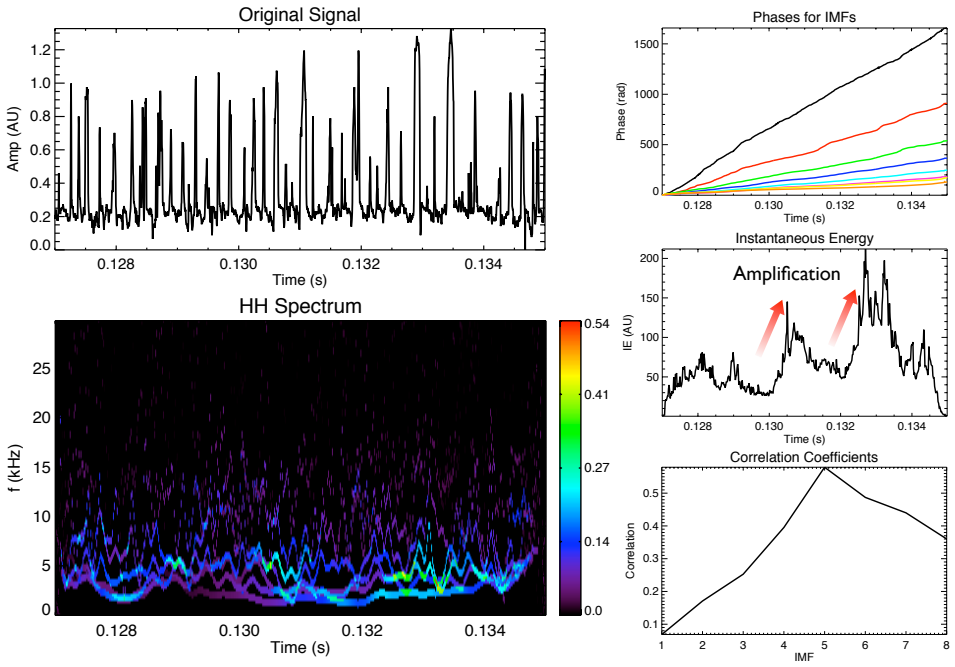

Figure 4.21: The Hilbert spectrum for density fluctuations over the same time as Fig.4.11. When the low-order azimuthal mode is formed around $t = 1.31$ and $t = 1.33$ s, the energy increases dramatically.

4.6 Bi-Orthogonal Decomposition

The bi-orthogonal decomposition method detailed in Sec.3.6 has been executed on density fluctuations measured by the polar imager in CTX. As can be seen in Fig.4.23, the amplitudes of the decomposition are well ordered in amplitude, with the lowest azimuthal mode numbers being dominant. The spatial mode functions are relatively simple $\sin(m\varphi)$, $\cos(m\varphi)$-like modes, even though no Fourier basis was prescribed. The radial profile of the spatial mode functions is broad, and representative of the density profile in the plasma. The mode functions are returned in sine and cosine pairs with similar amplitudes indicating a degeneracy or traveling wave in the system. This is a consequence of the $\mathbf{E} \times \mathbf{B}$ rotation of the plasma.

In contrast to the fairly simple sine and cosine-like spatial modes, the temporal fluctuation of these modes displays a much more complex variation (Fig.4.24). While the dominant frequency of the temporal modes increases with mode number, the time sequences are

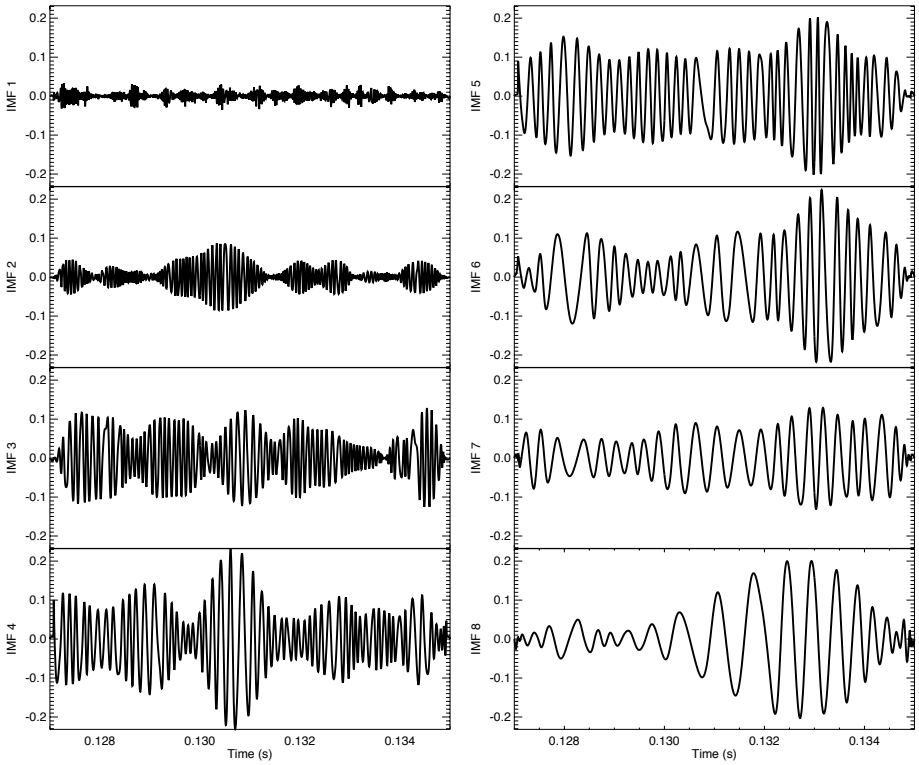

Figure 4.22: The Hilbert mode functions for density fluctuations. The 5^{th} mode function is most strongly correlated with the original data.

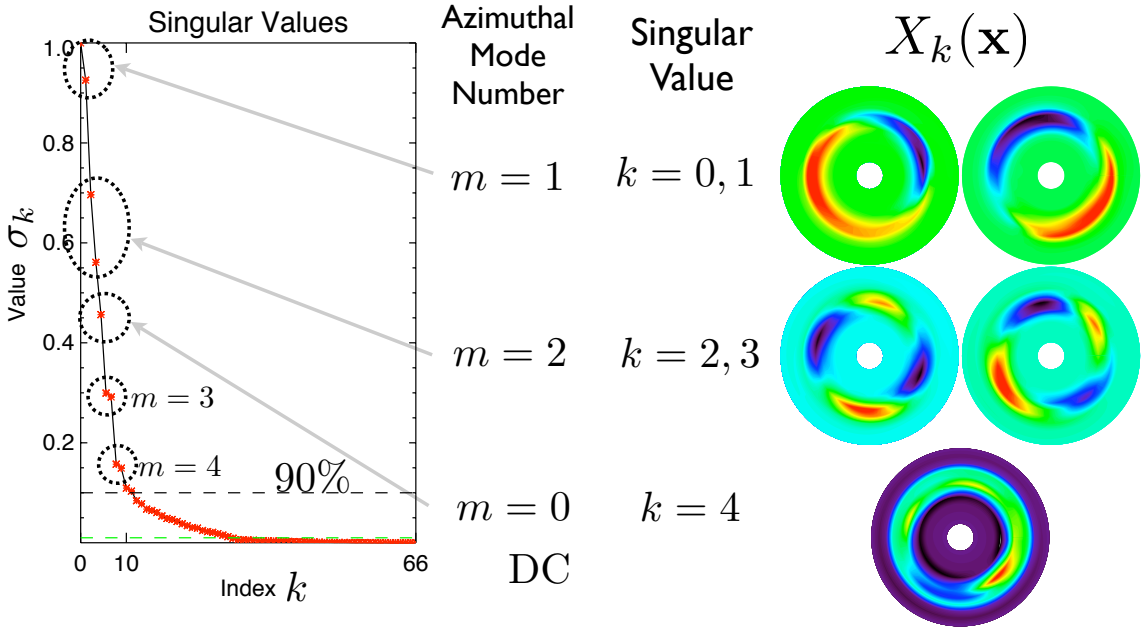

Figure 4.23: The amplitude of mode $k = 0, \ldots$ and the spatial mode functions.

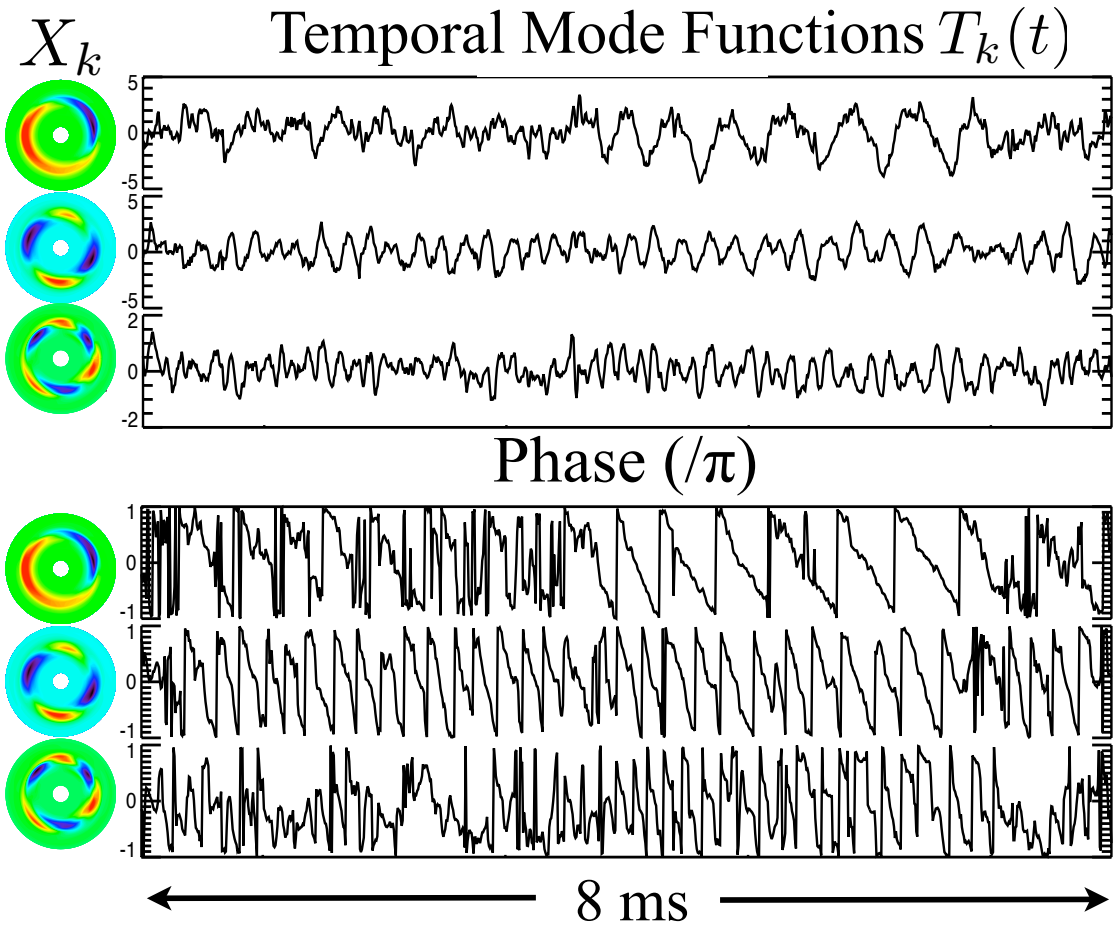

Figure 4.24: Spatial mode functions and the respective spatial and temporal modal decomposition. The modes for $k = 0, 2, 5$ are plotted corresponding the the azimuthal mode number $m = 1, 2, 3$.

more characteristic of turbulence, with a power-law spectrum and significant harmonic content. The lowest order temporal mode functions do contain some high frequency content. The highest frequency amplitude variation of the $m = 1$ component may in fact be do to the dynamics of the mode, or to an artifact of the decomposition. Nevertheless, the non-sinusoidal variation of $T_0(t)$ can lead to spectral harmonics, also indicating complex or nonlinear behavior.

In addition to the spectrum, the phase, or rotation, can be calculated via $\alpha_k = \tan^{-1}(T_k/T_{k+1})$ where T_k and T_{k+1} are the sine and cosine pairs for the mode functions k and $k+1$. The phase in Fig.4.24 displays periods of non-steady rotation, as well as coherent rotation indicated by the periodic sawteeth.

Because the modes are well-ordered and 90% of the amplitude is contained in the first 9 mode functions ($k = 0, \ldots, 8$) which correspond to the $m = 1, 2, 3, 4, \mathrm{DC}$ modes, the spatio-temporal dynamics of the fluctuations can be re-constructed by summing the product of the space and time mode functions weighted by their respective amplitudes $\hat{n}(x_j, t_i) \approx \sum_{k=0}^{\hat{K}-1} \sigma_k X_k T_k$, where now $\hat{K} = 9$. It is found that the truncated reconstruction well-represents the original data both globally *and* locally (Fig.4.25). Not only does the reconstruction well-represent the large-scale fluctuations, but in addition a single polar detector signal can be compared with the reconstruction of the signal at that same spatial point. Both the individual polar detector signal and the reconstructed signal display the same power-law characteristic of f^{-3}, which agrees with measurements in the bulk plasma. Thus, we find the turbulent fluctuations can be described either as chaotic variation of the amplitudes of a limited number of simple spatial modes that produce an equivalent local spectrum or, as will be described in Sec.4.8, as broad power-law spectrum of a very large number of turbulent structures that transfer energy and mean squared vorticity in both frequency and wavenumber.

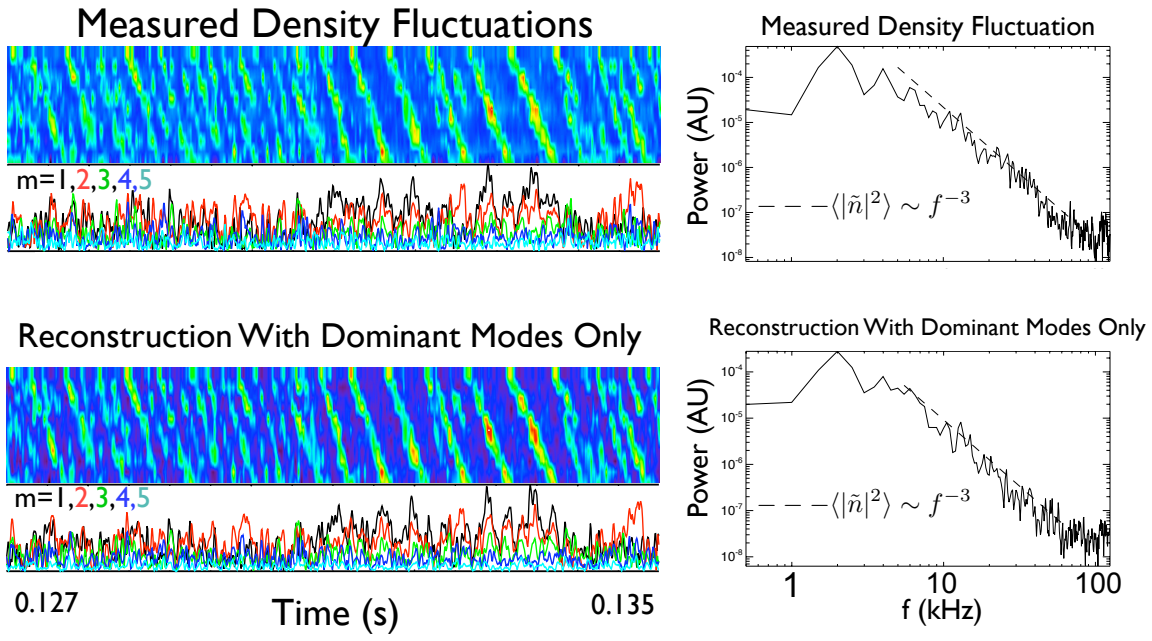

Figure 4.25: The truncated reconstruction of the plasma density using $\hat{K} = 9$. Good agreement is found between the observed density fluctuations and spatio-temporal reconstruction by the bi-orthogonal decomposition (left). The density spectrum of both the observed density at a single point and the reconstructed density at that point follow a f^{-3} trend.

4.7 Lyapunov Spectrum

The Lorenz system was originally derived from a finite mode truncation of the partial differential equations describing thermal convection in the Earth's lower atmosphere. Models of plasma convection similar to Rayleigh-Bérnard convection have been proposed [77], where there is a well-known plasma equivalent in flute modes. This has been investigated experimentally as well in the Helimak configuration [95]. The recurrence plot analysis used in Sec.3.7 is used to visualize embedded time series. When the embedding dimension is $d_E = 1$, the recurrence plot pattern resembles the 'checkerboard'-like pattern, similar to the Lorenz system embedded in a dimension less than the true dimensionality of the system. With dimension d_E increased to 3, lines parallel to the diagonal emerge, and indicate that there is periodicity in that chosen dimension. This is an indication of a low-dimensionality to the nonlinear system.

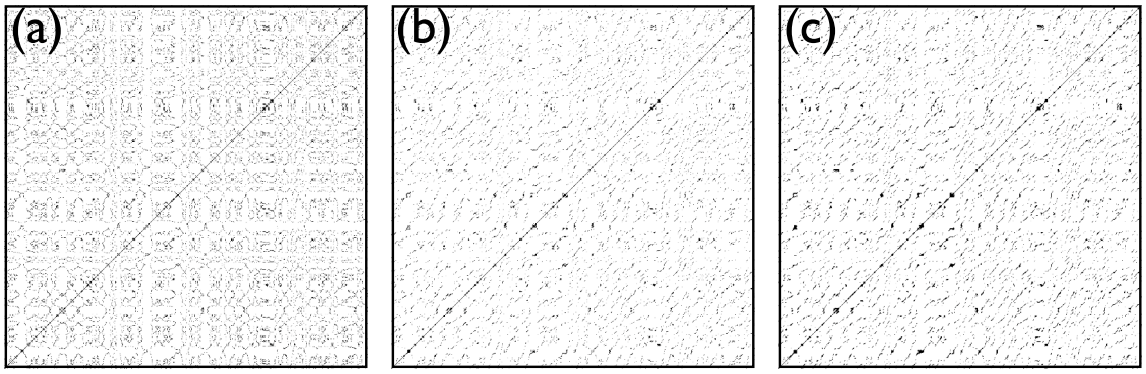

Figure 4.26: Recurrence plots for the density fluctuations in CTX embedded in one to three dimensions (a-c). For embedding dimension $d_E = 1$ there is a 'checkerboard' pattern. For embedding dimension $d_E = 3$, there are long lines parallel to the diagonal.

The same Lyapunov analysis technique introduced in Sec.3.7 has been performed with density fluctuation data in CTX, measured by the polar imager diagnostic. A single positive Lyapunov exponent persists as the embedded dimension is increased, indicating a chaotic time evolution. The value of the positive exponent converges near $25,000\ \mathrm{s}^{-1}$, corresponding to a Lyapunov time of 40 μs. This is near the auto-correlation time of the density fluctua-

tions, approximately 50 μs, and an order of magnitude faster than quasi-coherent density fluctuations of a few kHz. Similar results have been obtained in a magnetized torus exhibiting interchange modes [95]. Furthermore, above an assumed dimensionality of $d_E = 3$, smaller negative exponents appear, qualitatively similar to the Lorenz system. This is further indication of a low-dimensionality to the system, and is in qualitative agreement with the Hilbert and bi-orthogonal decompositions. The results from the Hilbert method displays 4 mode functions (IMFs 4-8) which are strongly correlated with the original time series. These are the lower frequency, longer wavelength modes with energy that is amplified when merging into the lowest order mode in the system. The bi-orthogonal decomposition also observes these in a complimentary sense, but on the global scale, and finds the spatial modes to be simple with complex time variation.

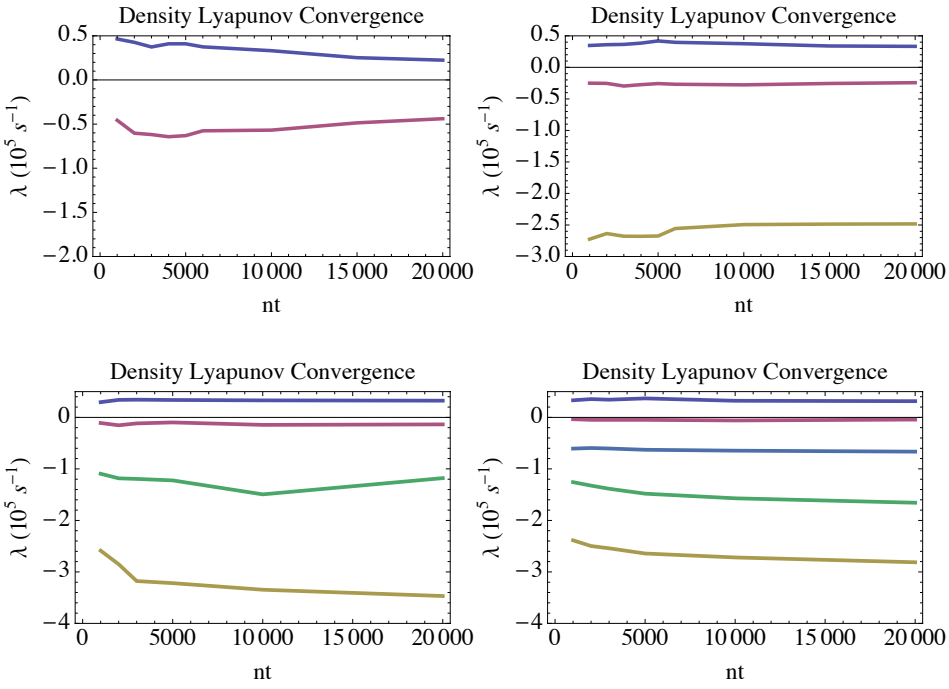

Figure 4.27: Convergence of Lyapunov exponents using 1,000 to 20,000 time points. For embedded dimension of $d_E = 2$, the spectrum is not well converged. For $d_E \geq 3$ the spectrum converges. For $d_E > 3$ exponents exist in the intermediate negative exponent range for $d_E > 3$, similar to spurious exponents calculated for the Lorenz system.

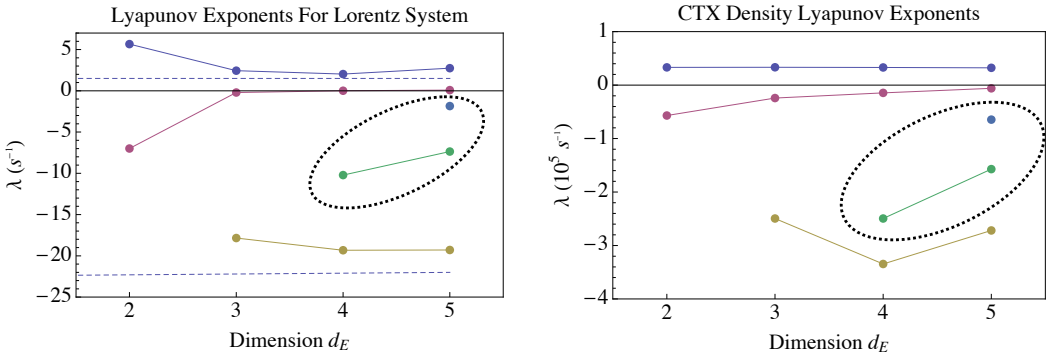

Figure 4.28: The Lyapunov spectrum for embedded dimension $d_E = [2, 5]$ for the Lorenz system (left) and density fluctuations in CTX (right). The largest Lyapunov number is converged near $25,000\ \mathrm{s}^{-1}$, or a characteristic time of 40 μs. For embedding dimension $d_E > 3$ small negative exponents are calculated.

4.8 Spectral Energy Transfer

The existence of quasi-coherent structures in background turbulence motivates a study of the direction of energy flow. Does the fluctuation energy in the small-scale turbulence, on average, receive energy from the large structures by the splitting of those large structures? Or, do the smaller turbulent structures merge to form these quasi-coherent modes? It is well known in fully developed three-dimensional turbulence that energy is the conserved quantity which flows down the spectrum, from the energy injection scale to larger wavenumber. The energy E_k flows to larger k, in a *forward* energy cascade. It is then at a finite k, the dissipation scale, where the energy is dissipated. This is the Kolmogorov scaling of $E_k \sim k^{-5/3}$. In two-dimensional systems such as soap films, stratified fluids, and strongly magnetized plasmas a different cascade process takes place [51]. In 2D flows, there are two conserved quantities: energy and enstrophy (mean-squared vorticity). When both energy and enstrophy are conserved, for k larger than the energy injection scale, there is a *forward* enstrophy cascade with $E_k \sim k^{-3}$. For k smaller than the injection scale, the energy takes on a $k^{-5/3}$ power-law like in 3D, but the energy flows to lower k, in an *inverse* energy cascade [87, 90, 79].

The method [71, 72] Sec.3.9 using ensemble spectral quantities such as the auto- and

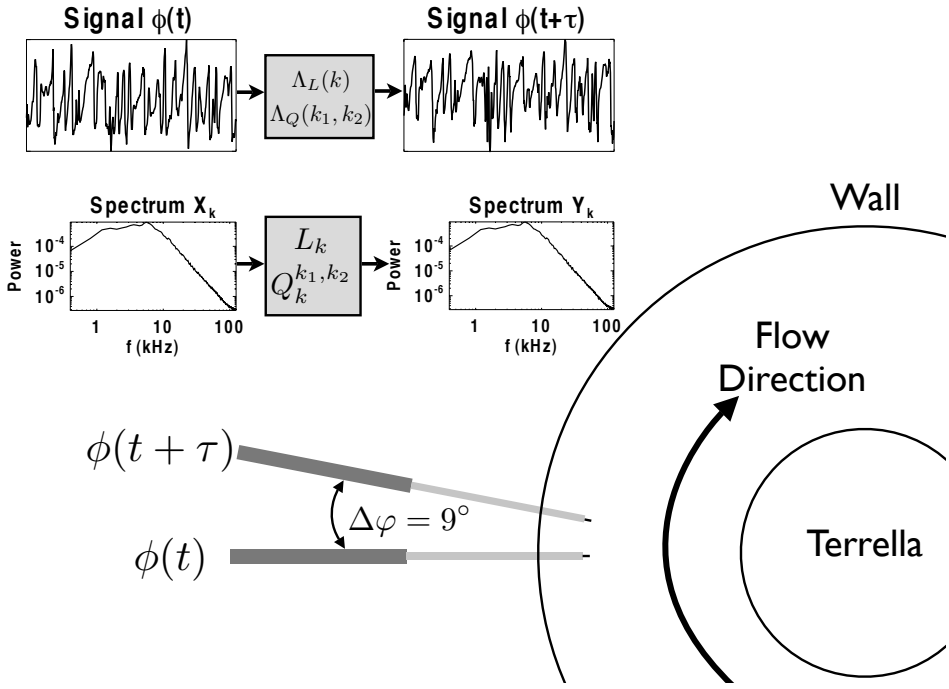

Figure 4.29: The experimental setup for measuring the nonlinear power transfer.

cross-power, as well as the auto- and cross-bispectrum calculates both the linear and quadratically nonlinear terms in a simple wave-kinetic equation3.35. Using two closely spaced probes in a flowing plasma, we can calculate the dispersion relation between frequency and wavenumber. If the wavenumber is linear over a frequency range, then over this range frequency and wavenumber can be related by a constant phase velocity v_φ, representing the propagation of fluctuations. This linear relationship allows a rigorous interchange of $f \leftrightarrow k$, rather than assuming this relationship, as is done with Taylor's hypothesis. This analysis can also be done in wavenumber domain [61] with an array of closely spaced probes. Using the bispectral analysis we calculate the dispersion for potential fluctuations measured by probes separated azimuthally by $\Delta x = 8$ cm with 4,000 realizations of the two signals Fig.4.30. A linear dispersion is found for fluctuations with $f < 40$ kHz, Fig.4.31, and over this range wavenumber $k = \omega/v_\varphi$ with $v_\varphi \approx 6$ km/s.

The calculated growth rate suggests that all fluctuations are damped. This is characteristic

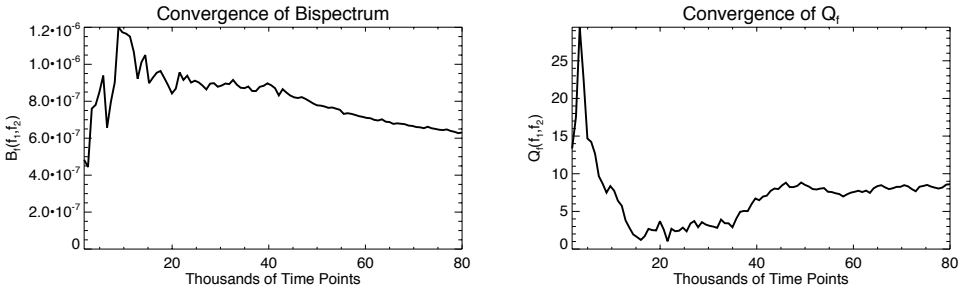

Figure 4.30: Convergence for the bispectrum and quadratic transfer function. The bispectrum is seen to converge above 50,000 time points (the decay is due to signal amplitude decay). Once the bispectrum has 'settled down', the quadratic transfer function is seen to converge.

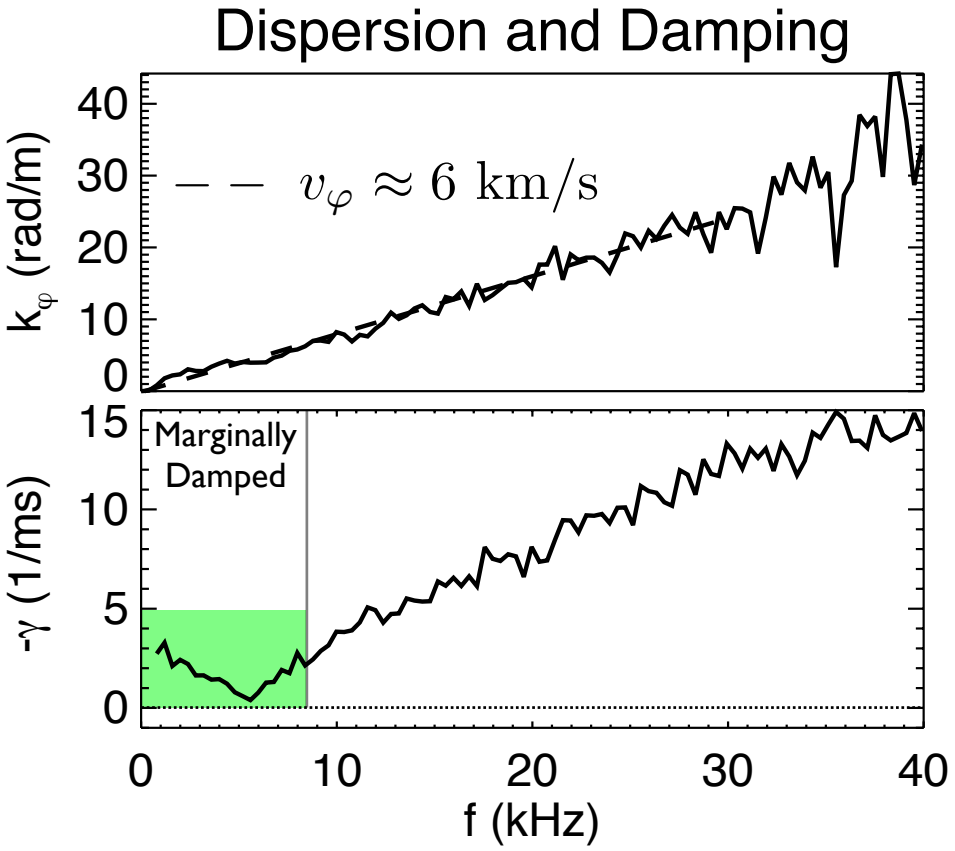

Figure 4.31: Dispersion relation and growth rate from the linear contribution Λ_L. The dispersion is linear at $v_\varphi = \omega/k \sim 6$ km/s. Marginally damped modes exist in the range below approximately 10 kHz.

of a continuously driven system rather than a freely-evolving system. Smaller scale structures in the higher frequency (wavenumber) range are more strongly damped. While a scale-free neutral damping coefficient would scale as $-\gamma \sim k^2$, the observed damping rate follows a more gradual trend. The fluctuations near 5-7 kHz are marginally damped or undamped, representing the "source" or "injection scale" of the turbulence. This energy injection scale is possibly due to rotational excitation of higher azimuthal mode number fluctuations, or non-axisymmetric heating of a nearly over-dense plasma. The quasi-coherent modes at m=1,2 exist in a more strongly damped wavenumber range than the essentially undamped fluctuations at 6-7 kHz (m=3-4), and therefore would be less likely to be observed than the m=3-4 structures. However, the higher mode number fluctuations are found to be sub-dominant when the plasma mode structure is measured. It is the power transfer function which will determine how the large-scale, low-m modes are generated, and come to dominate the quasi-coherent observed structures.

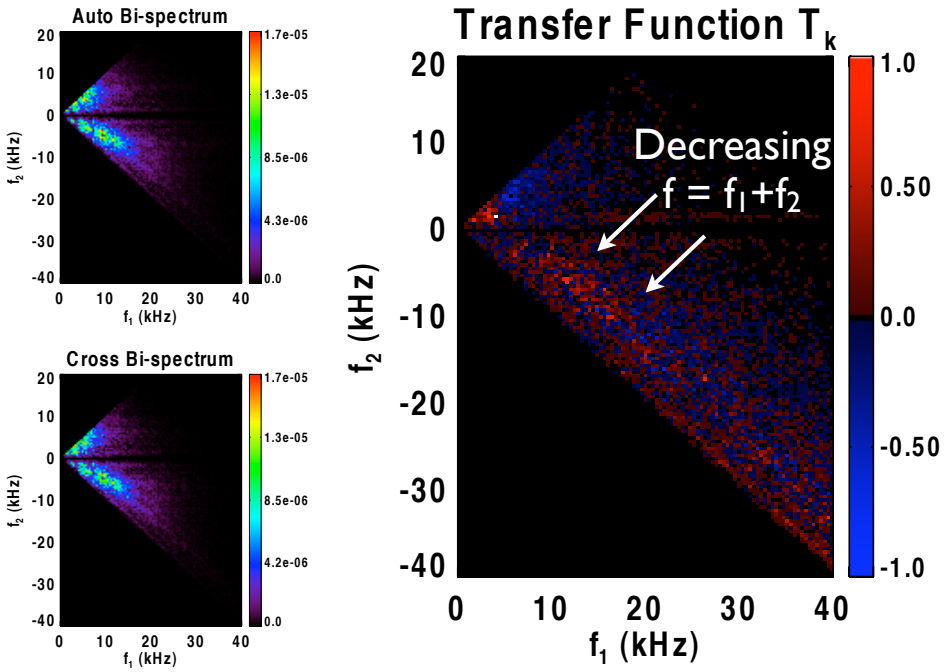

Figure 4.32: Auto- and cross- bi-spectra, as well as the nonlinear power transfer function. The transfer function $T_k(f_1, f_2)$ displays a positive power transfer at lower frequencies, most evident in the upper triangular region.

Using the calculated nonlinear coupling coefficient and bispectrum, the power transfer function is given as $T_k = \Re[\Lambda^k_Q \langle \phi_f \phi_{f_1} \phi_{f_2} \rangle]$. The converged auto- and cross- bi-spectra, and power transfer function $T_k(f_1, f_2)$ are shown in Fig.4.32. The relative power transfer into mode k is calculated by $\sum_{f=f_1+f_2} T_k(f_1, f_2)$. The transfer function is calculated to be 'conservative' in the fact that there is a power-match satisfying $\sum_f T_k(f) = 0$, and serves as another indication of proper convergence [90]. The power transfer is found to be positive for $f < 7 - 8$ kHz and negative for $f > 7 - 8$ kHz, Fig.4.33. This indicates that the smaller scale fluctuations give up their energy to the larger scale fluctuations in an inverse cascade, consistent with the expectations of two-dimensional turbulence. It is therefore reasonable to conclude that nonlinear amplification of small scale structures contributes to the predominance of the large-scale $m = 1$ and $m = 2$ modes in dipole interchange turbulence.

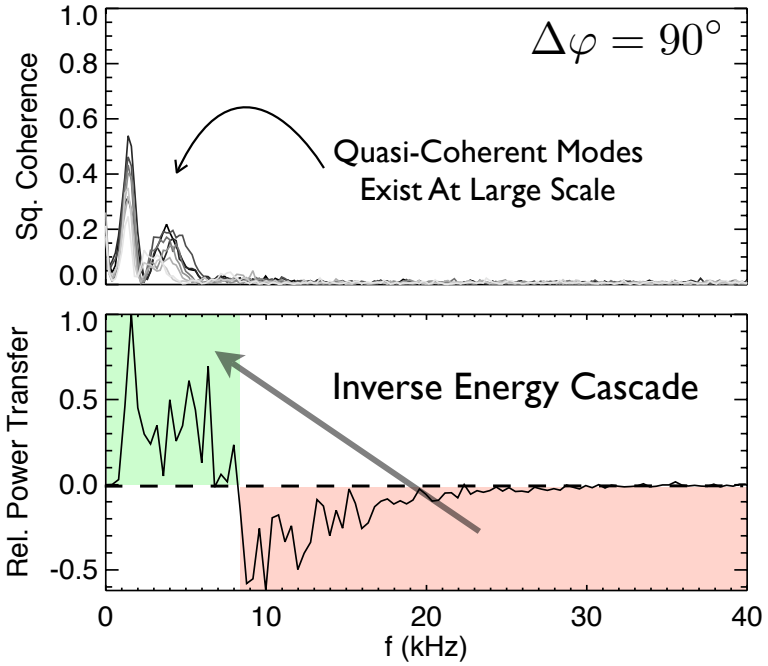

Figure 4.33: Coherent modes exist in the range $f \leq 5$ kHz. This is the frequency range which receives spectral power from higher frequency fluctuations.

4.8.1 Fluctuation Energy Spectrum

In the drift-interchange limit, the fluctuation energy in a plasma is given by the sum of an adiabatic and electrostatic contribution [36, 13].

$$E_k = \left(\frac{\tilde{n}_k}{\bar{n}}\right)^2 + k^2\rho_S^2\left(\frac{e\tilde{\Phi}}{T_e}\right)^2 \tag{4.2}$$

The observed spectral trends of $\langle|\tilde{n}_k|^2\rangle \sim k^{-3}$ and $k^2\langle|\tilde{\Phi}_k|^2\rangle \sim k^{-3}$ are in agreement with the expectations for two-dimensional turbulence. Using these ensemble quantities the energy spectrum for fluctuations in CTX has been computed and is shown in Fig.4.34 plotted against wavenumber $k = \omega/v_\varphi$. The spectrum obeys a power-law of $E_k \sim k^{-3}$ for $k > 2$ m^{-1}, consistent with the forward enstrophy cascade. The range just below $k = 2$ m^{-1} and above the coherent mode at $k = 0.9$ m^{-1} displays a $k^{-5/3}$ characteristic, consistent with the inverse energy cascade for k below the wavenumber of the injection scales. It is in this small range that the fluctuations have been shown to be very weakly or marginally damped. At L=50 cm, the total fluctuation intensity is $|\tilde{n}|/n_0 \approx 0.6$, $e|\tilde{\Phi}|/T_e \approx 0.5$, and the sonic Larmor radius is $\rho_S \approx 2$ cm with $T_e \approx 8$ eV and $|B| = 140$ G. For drift waves, experimental evidence shows that the energy fluctuation spectrum peaks for $k_\perp\rho_S \approx 1$, and increases in energy for $k_\perp\rho_S < 1$ are associated with zonal flow generation [13]. For interchange modes the energy spectrum peaks for $k_\perp\rho_S < 1$. This is consistent with the dominance of interchange fluctuations in CTX, not drift waves. While the adiabatic contribution to the fluctuation energy appears larger than the electrostatic part, both have the same power-law dependence for the energy spectrum as the Kraichnan result, $E_k \sim k^{-3}$.

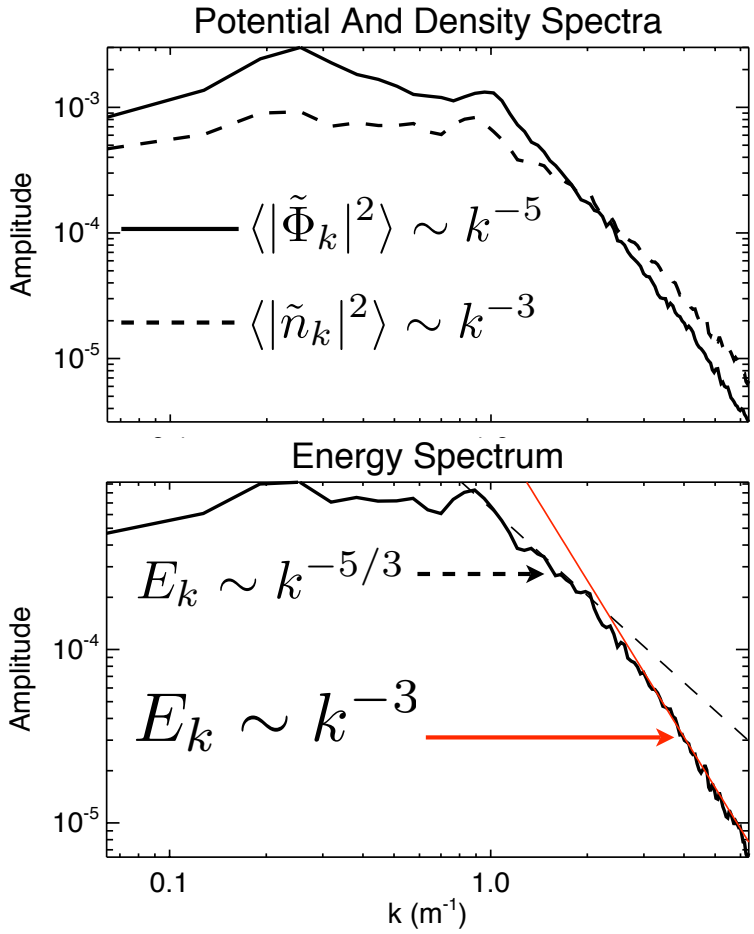

Figure 4.34: The spectra $\langle|\tilde{\Phi}_k|^2\rangle$, $\langle|\tilde{n}_k|^2\rangle$, and the computed energy spectrum E_k. The energy spectrum displays a k^{-3} power-law for $k > 2$ m^{-1}

4.9 Amplitude Correlation

The amplitude correlation technique of Sec.3.10, refs. [90, 89] has been applied to a single floating potential signal in CTX over an entire discharge. In further support of the calculation of spectral energy transfer and the observed power-law scaling indicating the inverse energy cascade, it is found that low frequency components lag high frequency components indicated by a positive lag cross-correlation function. The primary power bands of interest for this technique are the marginally damped spectral region and the low frequency band containing the quasi-coherent modes. As seen in Fig.4.35, the positive lag time in the cross-correlation function indicates that lower frequencies lag the higher frequencies. The interpretation of this result is that a 'pump' wave at frequency f_p, here represented by the marginally damped band, will decay into a lower frequency wave at $f < f_p$.

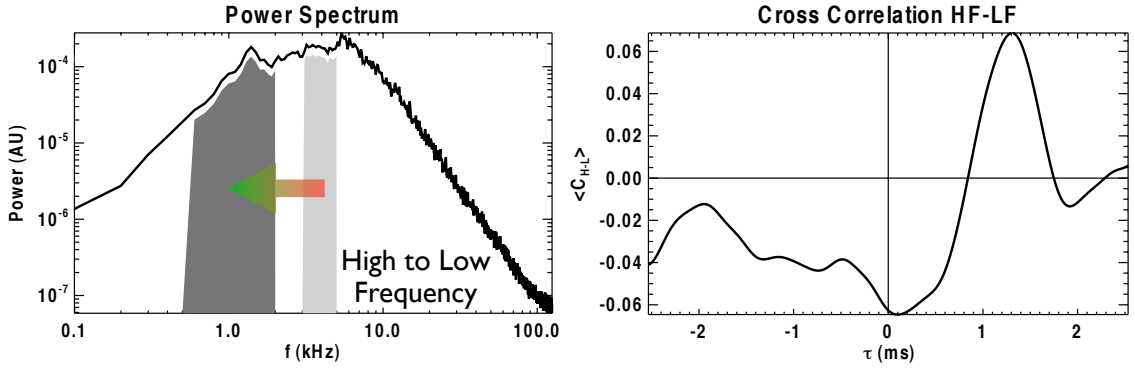

Figure 4.35: The amplitude correlation technique applied between the marginally damped spectral region and the low frequency region where quasi-coherent structures exist. The low frequency lags the high frequency.

Furthermore, it is in the spectral region for $f > 6$ kHz where the power spectrum takes on a full power-law trend. It is also found that the lower frequency band lags the higher frequency band in this spectral region (Fig.4.36). This is further indication that energy is flowing to the lower frequency, longer wavelength modes.

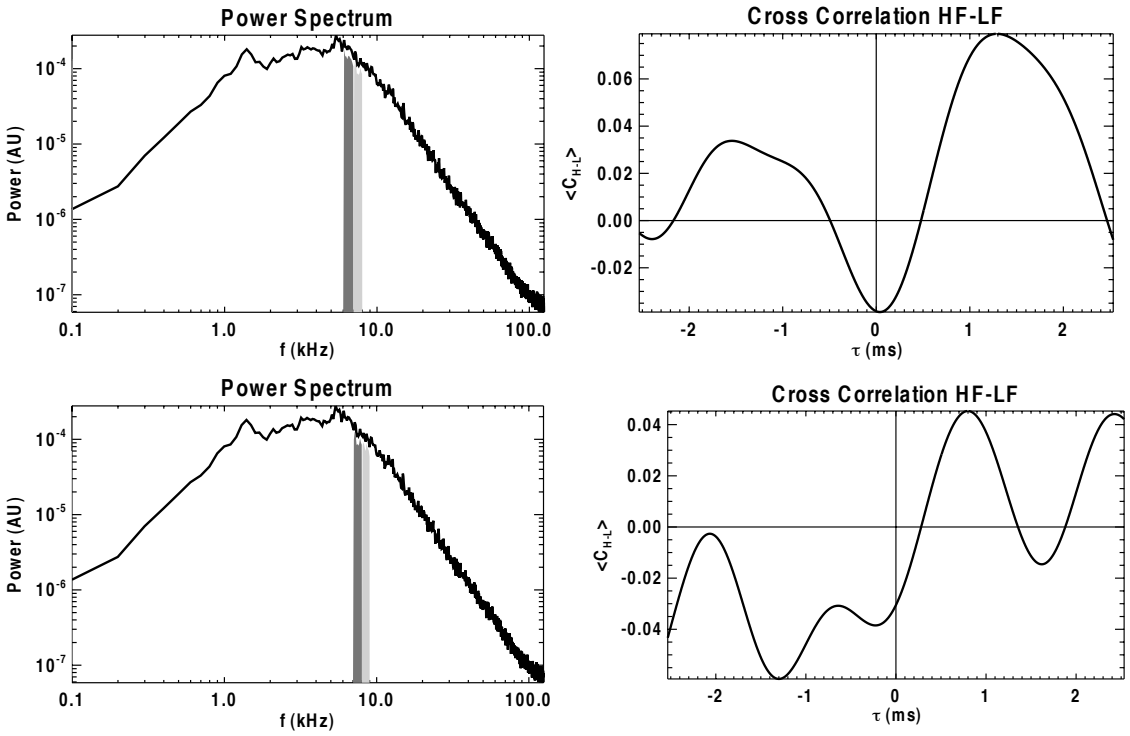

Figure 4.36: The amplitude correlation technique applied between frequency bands above the quasi-coherent modes. The low frequency lags the high frequency.

4.10 Summary of The Observation and Characterization of Interchange Turbulence

This section on the observed turbulence state of a dipole confined plasma reports the primary experimental results.

Local measurements indicate that the plasma fluctuations of density and potential are turbulent. The auto-correlation functions for both density and potential decay quickly, with correlation intervals of $\tau_c \approx 50, 60\ \mu$s, respectively. The potential fluctuations possess stronger long-range correlation of $m = 1, 2$ modes than the density fluctuations, with more pronounced secondary maxima in their auto correlation functions. The power spectra of potential fluctuations displays more pronounced spectral peaks at low frequency than the density, which is in agreement with the longer correlation interval. The spectral trends of density and potential admit power-law trends for frequencies above 10 kHz, with power-laws of f^{-3} and f^{-5}, respectively.

Using two diagnostics positioned on a magnetic field-line, the parallel wavenumber of potential fluctuations is determined to be $k_{\|} \approx 0$. The measurements have been made with a single fixed probe, and a second probe which moves radially at fixed azimuthal angle. There is a slight variation in the cross-phase at maximum cross-coherence when the moving probe is positioned radially separated from the refence field-line, but is exactly zero when $\Delta L = 0$.

The correlation length of potential fluctuation in the rotating plasma has been measured by cross-correlation analysis between probes separated azimuthally. The lag time τ_{Lag} increases in direct proportion to the separation distance between the probes. The azimuthal propagation of the potential is $v_\varphi \approx 6$ km/s in the $-\hat{\varphi}$ direction. The cross-correlation amplitude decreases with correlation length $\lambda_c \approx 45$ cm, and the correlation time in the moving frame is then calculated as $\lambda_c / v_\varphi \approx 75\ \mu$s. This is in close agreement with the auto-correlation time of the potential time trace.

Through ensemble spectral analysis, it is calculated that the potential structure contains

quasi-coherent $m = 1, 2$ modes at $f \approx 1.5$ and 3-4 kHz, respectively. The squared coherence is near 20-40%, being stronger closer to the heating location.

The correlation between bulk density measured by a Langmuir probe and a single polar detector collecting ion current on the same magnetic field-line is measured to possess a zero time-lag. Cross-correlation between density and multiple polar detectors determines that the polar current and bulk density fluctuations are self-consistent. Using the polar imager array, the plasma rotation is calculated to be near 1.5-2 kHz by cross-correlation analysis and the slope of the stripes in Fig.4.11

Density and potential have a mean phase shift of $|\langle \alpha_{\tilde{n},\tilde{\Phi}} \rangle| \approx \pi/2$ which produces a radial fluctuation induced particle flux to the outboard side of CTX. The density fluctuations near $L = 55$ cm also possess a probability density function which is positively skewed, with skewness $\approx +0.25$. The skewness of +0.25 indicates that intermittent transport events do occur in CTX, but with less relative intensity than the tokamak edge.

Based on the observed potential structure, a basis function expansion for the stream function has been used to calculate the global structure of the potential. The time evolution of the global density dynamics measured by the polar imager, along with the spatial and temporal derivatives, is used to invert the continuity equation. The time-averaged global potential found to be dominated by a radially broad, axisymmetric negative potential. The potential fluctuations are dominated by the lowest order, broad radial mode. The fluctuation intensity of potential perturbations decreases with increasing azimuthal mode number $m = 1, 2, 3$.

As a new diagnostic to CTX, a high-speed imaging camera has been used to view the visible light intensity at frame rates up to 10,000 fps. The camera has been oriented to view the radial width of the plasma, and over a angular wedge in azimuth. The fluctuations of light intensity by the fast camera is found to be correlated with density fluctuations and polar diagnostics with a lag time $\tau_{Lag} = 0$. The time-averaged radial light intensity profile is found to be in excellent agreement with the time-averaged density profile obtained from the polar

imager, both displaying that the density profile is radially broad. The radial profile of RMS light fluctuations are near 4%, and are maximum near the plasma ECRH resonance location, and also where the time-averaged profile gradient is the steepest. The radial wavenumber k_R of light fluctuations is calculated to be the longest wavelength which can fit in the system, confirming that the fluctuations of density are radially broad as well.

The Hilbert Transform-based modal decomposition of local single-point density fluctuations displays four mode functions which are correlated above 35% with the original time series. When coherent density structures are formed in time, the signal energy undergoes significant amplification.

The bi-orthogonal decomposition for multiple space-time points has shown that the amplitude of global density fluctuations can be represented by a limited number of spatio-temporal mode functions. The spatial structure of global density fluctuations is composed of a limited number of rotating, radially broad, low-order azimuthal modes. The temporal variation and phase of the relatively simple mode function displays significant harmonic content and periods of steady and non-steady rotation.

Lyapunov exponent analysis of the density fluctuations reveals that the time evolution is chaotic, with a converged positive Lyapunov number $\lambda \approx 25,000\text{s}^{-1}$. The Lyapunov time is 40 μs, near the auto-correlation time of density fluctuations. The Lyapunov analysis also reveals a low-dimensionality to the time evolution.

Based on bispectral analysis, the potential fluctuations are found to be linearly damped, with smaller scale structures damped more strongly than the large structures near $m = 4$ which are marginally damped. The nonlinear power transfer estimator displays suppression of short wavelength structures with mode number $m > 4$, and amplification of the long wavelength $m = 1, 2$ quasi-coherent modes.

The fluctuation energy spectrum is a combination of adiabatic and electrostatic energy, and possesses as k^{-3} power-law trend for $k > 2$ m^{-1}. There also exists a $k^{-5/3}$ region of the energy spectrum at higher k than the quasi-coherent modes and at lower k than the

marginally damped modes.

The amplitude correlation technique calculates a positive time lag between fluctuations in the marginally damped spectral region, and the quasi-coherent modes.

Chapter 5

Simulating Interchange Turbulence

A high-performance simulation [66, 56] is used to investigate the effects of adding a particle source and sink on a dipole confined plasma. The code evolves cold fluid ions with kinetic electrons on a 2D grid in azimuthal angle and normalized magnetic flux ($\varphi, y = \psi/\psi_0$). The third spatial dimension, parallel to the magnetic field, is eliminated by bounce averaging the motion of particles. The bounce-averaging of motion along the magnetic field lines allows the study of the low-frequency interchange dynamics perpendicular to the strong confining field in the same manner as the previous chapter Ch.4.

Numerically, the leapfrog method explicit time-stepping scheme is used to evolve the ion density per unit flux $\hat{N}_i$, the electron distribution function F_μ composed of multiple species of electrons at energy μ, charge density and potential. A flux-corrected transport algorithm [93, 94] is used to advance the electron distribution functions and ions.

The motion of the electron distribution is given by

$$\frac{\partial F_\mu}{\partial \hat{t}} + \nabla \cdot (F_\mu \hat{\mathbf{V}}_e) = 0 \tag{5.1}$$

where $\hat{\mathbf{V}}_e$ is the sum of the $\mathbf{E} \times \mathbf{B}$ and azimuthal magnetic particle drift.

The ion fluid motion is determined by the ion continuity equation

$$\frac{\partial \hat{N}_i}{\partial \hat{t}} + \nabla \cdot (\hat{N}_i \hat{\mathbf{V}}_\mathbf{i}) = 0 \tag{5.2}$$

where $\hat{N}_i$ is the density per unit flux $N = \langle n \rangle \delta V$ ($\delta V = \int d\chi / B^2$, $\langle A \rangle = \delta V^{-1} \int A d\chi / B^2$) and $\hat{\mathbf{V}}_i$ is the sum of the $\mathbf{E} \times \mathbf{B}$ and polarization drifts. The ion polarization drift is calculated through a nonlinear solver, obtaining the time-rate of change of potential by solving

$$\frac{\partial}{\partial \hat{t}} \nabla \cdot \epsilon \nabla \hat{\Phi} = -4\pi \frac{\partial \hat{\rho}}{\partial \hat{t}} = \nabla \cdot \hat{\mathbf{J}} \tag{5.3}$$

in an iterative manner, where $\hat{\mathbf{J}}$ is a function of $\partial \hat{\Phi} / \partial \hat{t}$

In the leapfrog scheme, the velocities are always a half time-step off from the quantities which they are pushing. The following is a sketch of the method for advancing time in the the code, where the time index is superscripted:

- Initialize

$$\begin{array}{ccc} \hat{\Phi}^{j-2} , \hat{\Phi}^{j-1} & , & \hat{\Phi}^{j} \\ \hat{N}_i^{j-1} & , & \hat{N}_i^{j} \\ F^{j-1} & , & F^{j} \end{array}$$

- Leapfrog half-step

$$
\begin{aligned}
\hat{\mathbf{V}}_{\mathbf{E}}^{j} &= \frac{\mathbf{B}\times\nabla\hat{\Phi}^{j}}{B^2} \\
F^{j+1/2} &= F^{j-1/2} - \Delta\hat{t}\nabla\cdot(F^{j}\hat{\mathbf{V}}_{e}^{j}) \text{ where } \hat{\mathbf{V}}_{e} = \hat{\mathbf{V}}_{\mathbf{E}} + \hat{\mu}y^2\hat{\varphi} \\
\left(\frac{\partial\hat{\Phi}}{\partial\hat{t}}\right)^{j} &\leftarrow \text{Solving } \frac{\partial}{\partial\hat{t}}\nabla\cdot(\epsilon\nabla\hat{\Phi}^{j}) = -4\pi\frac{\partial\hat{\rho}^{j}}{\partial\hat{t}} = 4\pi\nabla\cdot\hat{\mathbf{J}}^{j} \\
&\quad \text{where } \hat{\mathbf{J}}^{j} = \hat{\mathbf{J}}^{j}\left(\hat{\rho}^{j}, F^{j}, \hat{N}_{i}^{j}, \hat{\Phi}^{j}, \frac{\partial\hat{\Phi}}{\partial\hat{t}}^{j}\right) \\
\hat{N}_{i}^{j+1/2} &= \hat{N}_{i}^{j-1/2} - \Delta\hat{t}\nabla\cdot(\hat{N}_{i}^{j}\hat{\mathbf{V}}_{i}^{j}) \text{ where } \hat{\mathbf{V}}_{i} = \hat{\mathbf{V}}_{\mathbf{E}} + \hat{\mathbf{V}}_{p} \\
\hat{\Phi}^{j+1/2} &= \hat{\Phi}^{j-1/2} + \Delta\hat{t}\left(\frac{\partial\hat{\Phi}}{\partial\hat{t}}\right)^{j} \\
\hat{\rho}^{j+1/2} &= \nabla^2\hat{\Phi}^{j+1/2}
\end{aligned}
$$

- Leapfrog full-step

$$
\begin{aligned}
\hat{\mathbf{V}}_{\mathbf{E}}^{j+1/2} &= \frac{\mathbf{B}\times\nabla\hat{\Phi}^{j+1/2}}{B^2} \\
F^{j+1} &= F^{j-1} - \Delta\hat{t}\nabla\cdot(F^{j+1/2}\hat{\mathbf{V}}_{e}^{j+1/2}) \text{ where } \hat{\mathbf{V}}_{e} = \hat{\mathbf{V}}_{\mathbf{E}} + \hat{\mu}y^2\hat{\varphi} \\
\left(\frac{\partial\hat{\Phi}}{\partial\hat{t}}\right)^{j+1/2} &\leftarrow \text{Solving } \frac{\partial}{\partial\hat{t}}\nabla\cdot(\epsilon\nabla\hat{\Phi}^{j+1/2}) = -4\pi\frac{\partial\hat{\rho}^{j+1/2}}{\partial\hat{t}} = 4\pi\nabla\cdot\hat{\mathbf{J}}^{j+1/2} \\
&\quad \text{where } \hat{\mathbf{J}}^{j+1/2} = \hat{\mathbf{J}}^{j+1/2}\left(\hat{\rho}^{j+1/2}, F^{j+1/2}, \hat{N}_{i}^{j+1/2}, \hat{\Phi}^{j+1/2}, \frac{\partial\hat{\Phi}}{\partial\hat{t}}^{j+1/2}\right) \\
\hat{N}_{i}^{j+1} &= \hat{N}_{i}^{j-1} - \Delta\hat{t}\nabla\cdot(\hat{N}_{i}^{j+1/2}\hat{\mathbf{V}}_{i}^{j+1/2}) \text{ where } \hat{\mathbf{V}}_{i} = \hat{\mathbf{V}}_{\mathbf{E}} + \hat{\mathbf{V}}_{p} \\
\hat{\Phi}^{j+1} &= \hat{\Phi}^{j-1} + \Delta\hat{t}\left(\frac{\partial\hat{\Phi}}{\partial\hat{t}}\right)^{j+1/2} \\
\hat{\rho}^{j+1} &= \nabla^2\hat{\Phi}^{j+1}
\end{aligned}
$$

5.1 The Hot Electron Interchange Simulation

The simulation code was previously to study the hot electron interchange mode in magnetic dipole geometry [65]. This 'initial value' code evolves a linearly unstable pressure profile, and accurately reproduces the 'frequency-sweeping' nonlinear evolution of fluctuations.

The code also includes ion rotation to drive the centrifugal instability [57]. While the developed simulation has reproduced many of the observations in CTX, it is insufficient for simulating the higher density, turbulent plasmas investigated in this thesis. The existing sequential simulation has computational times prohibitive for computational domains larger than 64×64. There is no conserving source and sink which would allow simulations to achieve a steady, turbulent state.

5.2 Parallelization of Existing Code

To simulate turbulence and measure fluctuations over a large range of scale separations, fine spatial resolution is required. For the sequential simulations on a computationally refined grid, the time to execute a simulation to steady state and the storage requirements on a single processor architecture become prohibitive. Therefore, the existing code written in FORTRAN has been translated to C, and parallelized with the PETSc package for distributed computing [7, 6, 8]. PETSc is a leading suite of data structures and routines for massively parallel architecture, based on the MPI message passing standard for communication. The parallelization of the simulation code requires a distributed nonlinear fast Poisson solver, which has been developed in collaboration with H. Zhang at Argonne National Laboratory.

For the fully parallel simulation, the computational domain (φ, y) is broken into horizontal 'bands' continuous in the periodic direction (φ), but breaking the radial domain across processes (Fig.5.1). This domain decomposition allows continued use of the spectral method for inverting the Poisson equation.

5.2.1 Fast Poisson Solver

For the majority of the simulation, which is dominated by function evaluations (*e.g.* increasing the number of electron species, evaluating local flux functions, performing numerical derivatives), parallel speedup is achieved immediately even for small computational grids.

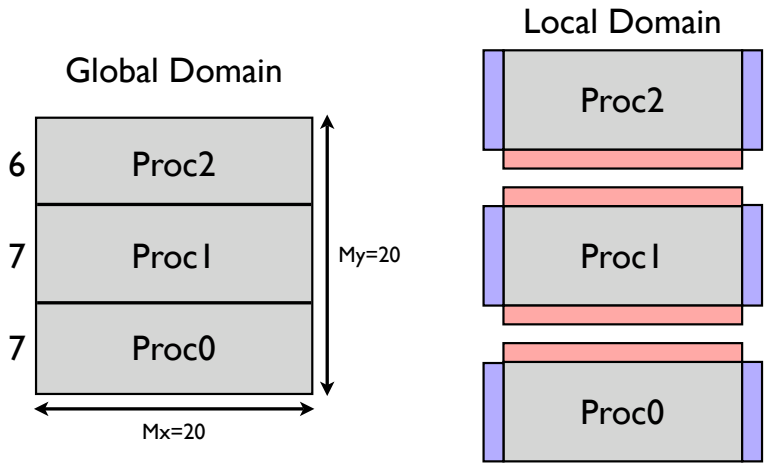

Figure 5.1: The computational domain decomposition allowing use of the sequential FFTW.

The solution to the Poisson equation, however, is a global solve, not a local function evaluation. The solution to Poisson's equation therefore requires communication across processes. The Fast Poisson Solver (FPS) is unique in that it requires the fast solution to a complex, non-symmetric tri-diagonal linear system: an inherently sequential operation based on the $\mathcal{LU}$ decomposition. In collaboration with H. Zhang at Argonne National Laboratory, we have developed the DAFPS (Distributed Array Fast Poisson Solver) PETSc module for parallel fast Poisson solves using a divide and conquer algorithm [82]. The system to be solved is a general $\mathcal{A}\mathbf{x} = \mathbf{b}$, tri-diagonal linear system. The Thomas algorithm [82] is the usual means of an exact solution, performed sequentially and 'in place' for speed and memory efficiency. The Thomas algorithm, however, cannot be used for a global linear solve, because it will not parallelize. In order to solve the system exactly, without assumptions of diagonal dominance or symmetry, the matrix is decomposed as follows:

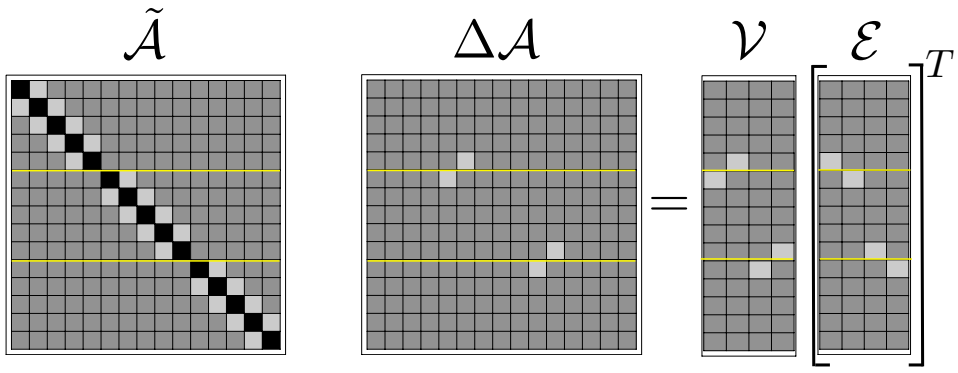

Figure 5.2: The decomposition across 3 processors of tri-diagonal matrix $\mathcal{A}$ into $\tilde{\mathcal{A}}$ (left) and $\Delta\mathcal{A} = \mathcal{V}\mathcal{E}^T$ (right). The processor boundaries are indicated by the yellow lines.

$$
\begin{aligned}
\mathcal{A}\mathbf{x} &= \mathbf{b} \\
\mathcal{A} &= \tilde{\mathcal{A}} + \Delta\mathcal{A} \\
&= \tilde{\mathcal{A}} + \mathcal{V}\mathcal{E}^T \\
\mathbf{x} &= \mathcal{A}^{-1}\mathbf{b} \\
&= (\tilde{\mathcal{A}} + \mathcal{V}\mathcal{E}^T)^{-1}\mathbf{b} \\
&= \tilde{\mathcal{A}}^{-1}\mathbf{b} - \tilde{\mathcal{A}}^{-1}\mathcal{V}(\mathcal{I} + \mathcal{E}^T\tilde{\mathcal{A}}^{-1}\mathcal{V})^{-1}\mathcal{E}^T\tilde{\mathcal{A}}^{-1}\mathbf{b}
\end{aligned}
$$

where $\tilde{\mathcal{A}}$ is block tri-diagonal, and $\Delta\mathcal{A}$ contains the remaining off-diagonal entries. The interface system which requires communication between processes is illustrated in Fig.5.2.

The solution procedure is summarized as follows for the general system $\mathcal{A}\mathbf{x} = \mathbf{b}$, where the left-aligned equations are solves, and the right-aligned equations are algebraic.

$$
\begin{aligned}
\tilde{\mathcal{A}}\tilde{\mathbf{x}} &= \mathbf{b} \\
\tilde{\mathcal{A}}\mathcal{Y} &= \mathcal{V} \\
&\mathbf{h} = \mathcal{E}^T\tilde{\mathbf{x}} \\
&\mathcal{Z} = \mathcal{I} + \mathcal{E}^T\mathcal{Y} \\
\mathcal{Z}\mathbf{y} &= \mathbf{h} \\
&\Delta\mathbf{x} = \mathcal{Y}\mathbf{y} \\
&\mathbf{x} = \tilde{\mathbf{x}} - \Delta\mathbf{x}
\end{aligned}
$$

This major advancement allows the simulation to be run on a massively parallel architecture with very large spatial grids. The strong scaling and parallel speedup for a 250×250 computational grid is show in Fig.5.3. For up to 12 nodes (CPUs), the execution time for a single iteration of the simulation drops from 14 s to 2 s, a speedup of a factor of 7. While this may not be ideal scaling[1], it nevertheless allows reasonable execution time for achieving a steady state.

5.2.2 Simulating Steady State, Driven Turbulence

To simulate the turbulent plasmas in CTX, a particle conserving source and sink of ion and electron density and electron energy is incorporated into the time evolution of the ions and electron distribution functions. The time evolution is advanced by the leapfrog scheme based on the continuity equation, but now has a source and sink added:

$$\frac{\partial \hat{N}_i}{\partial t} + \nabla \cdot (\hat{N}_i \hat{\mathbf{V}}_i) + \nabla \cdot \mathbf{\Gamma}_D = S \tag{5.4}$$

[1]Ideal speedup has $T_1/T_{np} = np$ where T_1 is the execution time on one processor, and T_{np} is the execution time on np processors.

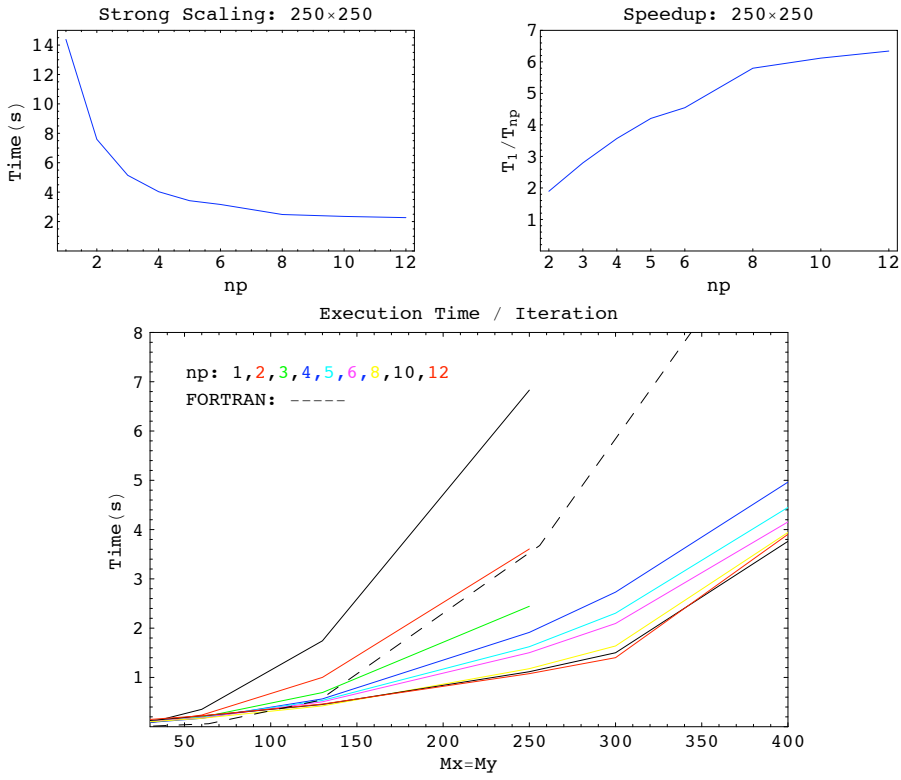

Figure 5.3: Parallel performance of the simulation code. A 250×250 computational grid shows good strong scaling and parallel speedup for up to 12 nodes (CPUs). For a computational grid larger than 130^2 the performance of the parallel version of the code far exceeds the sequential FORTRAN version.

where $\mathbf{\Gamma}_D = -\mathcal{D}\cdot\nabla\hat{N}_i$ is the particle flux, $\mathcal{D}$ is the cross-field diffusion tensor, and S a volume source rate of particles. The diffusion profile is taken as axisymmetric $\mathcal{D} = D(\psi)(\mathcal{I} - \hat{\mathbf{b}}\hat{\mathbf{b}})$. In non-dimensionalized magnetic coordinates, this is

$$\frac{\partial\hat{N}}{\partial\hat{t}} + \frac{\partial}{\partial\varphi}(\hat{N}_i V_{i,\varphi}) + \frac{\partial}{\partial y}(\hat{N}_i V_{i,y}) - 1.8\hat{D}h_D y^2\frac{\partial^2\hat{N}_i}{\partial\varphi^2} - 3.2\hat{D}\frac{\partial}{\partial y}\left[h_D\frac{\partial}{\partial y}(y^4\hat{N}_i)\right] = \hat{D}D_S h_S \quad (5.5)$$

were $D(\psi) \to \hat{D}h_D(y)$. The functions $h_D(y)$ and $h_S(y)$ are normalized diffusion and source profiles. Thus the single parameter $\hat{D}$ represents the strength of the particle 'recycling'. To maintain the total number of particles, the time-rate of change of the integrated ion density must be unchanged.

$$\int\frac{\partial\hat{N}}{\partial\hat{t}}d^2\mathbf{x} = 0 \quad (5.6)$$

The coefficient D_S is negative the integrated volume loss rate of diffusion divided by the integrated volume source profile, and must be calculated at every time step to maintain conservation. Therefore, we calculate D_S as

$$D_S = \frac{-\int 1.8h_D y^2\frac{\partial^2\hat{N}}{\partial\varphi^2} + 3.2\frac{\partial}{\partial y}(h_D\frac{\partial}{\partial y}(y^4\hat{N}))d^2\mathbf{x}}{\int h_S d^2\mathbf{x}} \quad (5.7)$$

At each time step both the ions and each electron distribution function $\hat{N}, F_\mu$ are updated with a 2D grid which integrates to zero. Because the ions are cold but move as a fluid, the number density $\hat{N}_i$ must be conserved. The electron distribution functions F_μ, however, each have characteristic energy $\hat{\mu}$. Therefore the electron source adds to the distribution, maintaining number conservation and energy conservation.

5.3 Results from Simulations

On a 60 x 60 grid, quasi-steady driven turbulence is achieved with the conserving source and sink. This represents a grid spacing of approximately 5.2 cm at L=50 cm major radius. When

the diffusion parameter is too small $\hat{D} = 1.0 \times 10^{-5}$, the strength of the recycling is too weak, and the density profile is maintained at marginal stability $\partial N/\partial\psi \approx 0$ (Fig.5.4,bottom). There is very little density or potential fluctuation for $\hat{D} = 1.0 \times 10^{-5}$. When the diffusion parameter is too large, the steady-state density profile approaches the difference between the source and sink profiles (Fig.5.4,top), far from marginal stability. When the diffusion parameter[2] is set at $\hat{D} = 1.0 \times 10^{-4}$, quasi-steady convection cells develop (Fig.5.4,middle). These convective cells are radially broad, and have low order azimuthal wavenumbers. During this steady convection, the density profile is maintained slightly steeper than marginal stability. This is in agreement with density profile measurements in CTX (Fig.2.16).

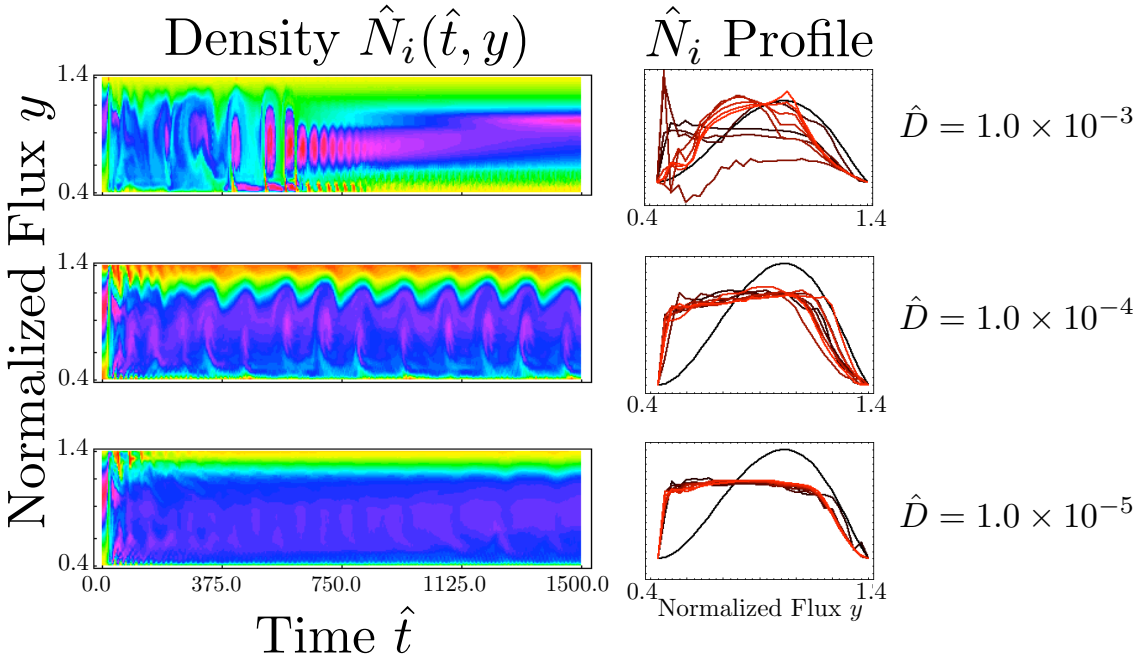

Figure 5.4: The results for three different values of the parameter $\hat{D}$, which determines the 'strength' of the source/sink. When the diffusion is strong (top), the steady state density profile matches that of the source profile. When the diffusion is too weak, no recycling occurs and the density takes on a $\hat{N}_i(y)$=constant, or $n(L) \sim 1/L^4$ profile. When the diffusion is adjusted to $\hat{D} \sim 1.0 \times 10^{-4}$, steady-state recycling of large convective cells occurs. The profile increases slightly with y, indicating that the density is maintained at a profile steeper than marginal stability.

[2]This is a diffusion coefficient of $D_\perp \approx 15\ m^2/s$, using $D = \hat{D}\omega_{dh}L_0^2$

The potential profiles from the simulation are also in agreement with the measurements in CTX. The potential structure is found to be radially broad and negative. This potential profile agrees with both probe measurements (Fig.2.16) and the stream function calculation detailed in Sec.3.34 and results presented in Fig.4.16.

On a more refined grid, the coherent structures are less pronounced. Higher m-number structures are observed to persist on a computational domain of $M_x \times M_y = 200 \times 60$. This represents a grid spacing of approximately 1.56 cm at $L = 50$ cm. This size scale is of the order of the ion gyro-radius in CTX for a 1 eV ion at major radius L=50 cm where $\rho_i \approx 1$ cm.

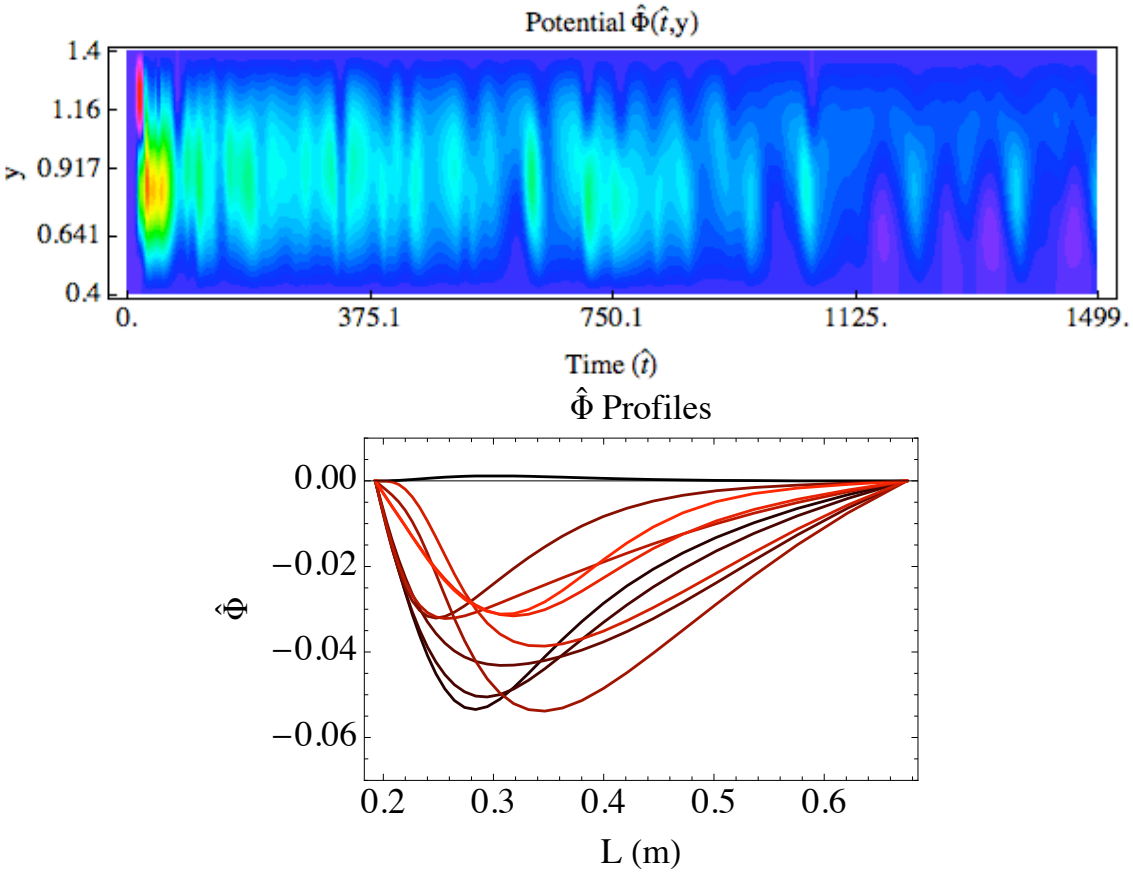

Figure 5.5: The non-dimensionalized potential $\hat{\Phi}$ measured at $\varphi = 0$, and across the plasma radius from y=[1.4, 0.4] (L=[25,65 cm]). The evolution of the profile $\hat{\Phi}(L)$ indicated as black to red as time evolves. The profile is similar to that in Fig.4.16

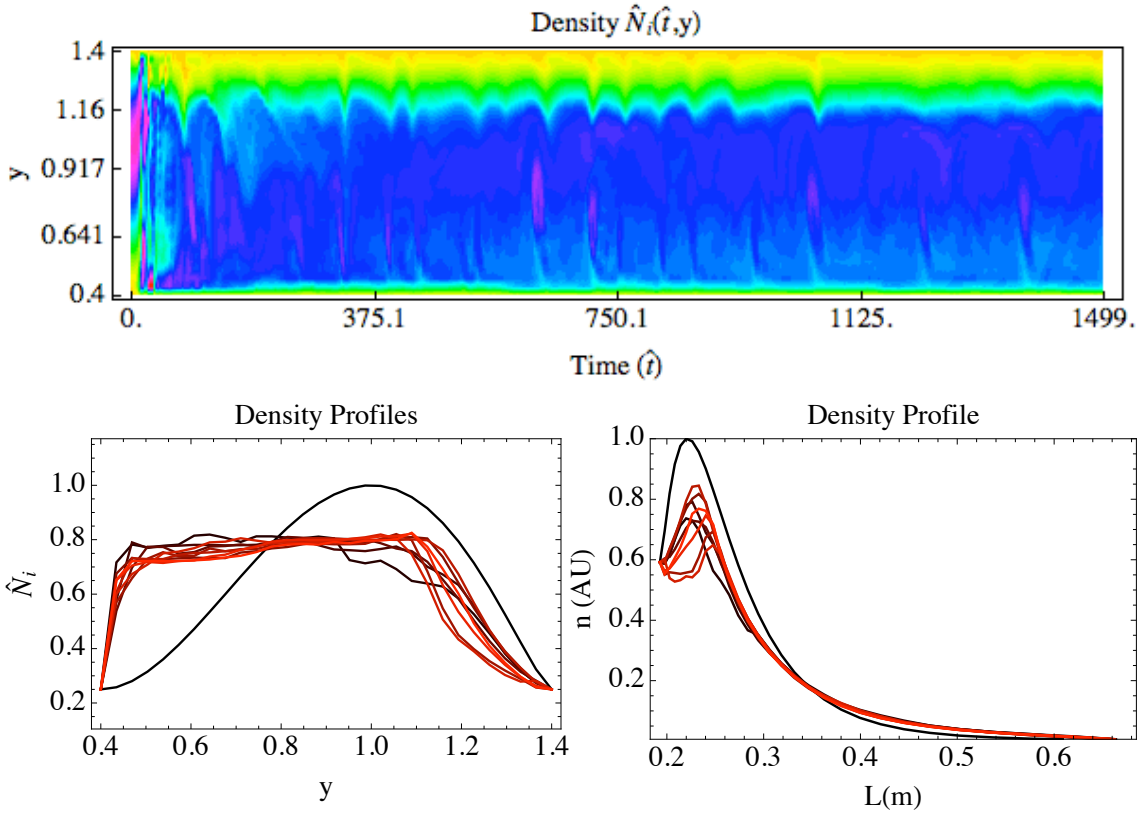

Figure 5.6: The non-dimensionalized density $\hat{N}_i$ measured at $\varphi = 0$, and across the plasma radius from y=[1.4, 0.4] (L=[25,65] cm). The evolution of the profile $\hat{N}_i(y)$ is maintained slightly steeper than marginal stability ($\partial N_i/\partial y = cnst$). Also the density profile in laboratory coordinates which varies like $1/L^4$.

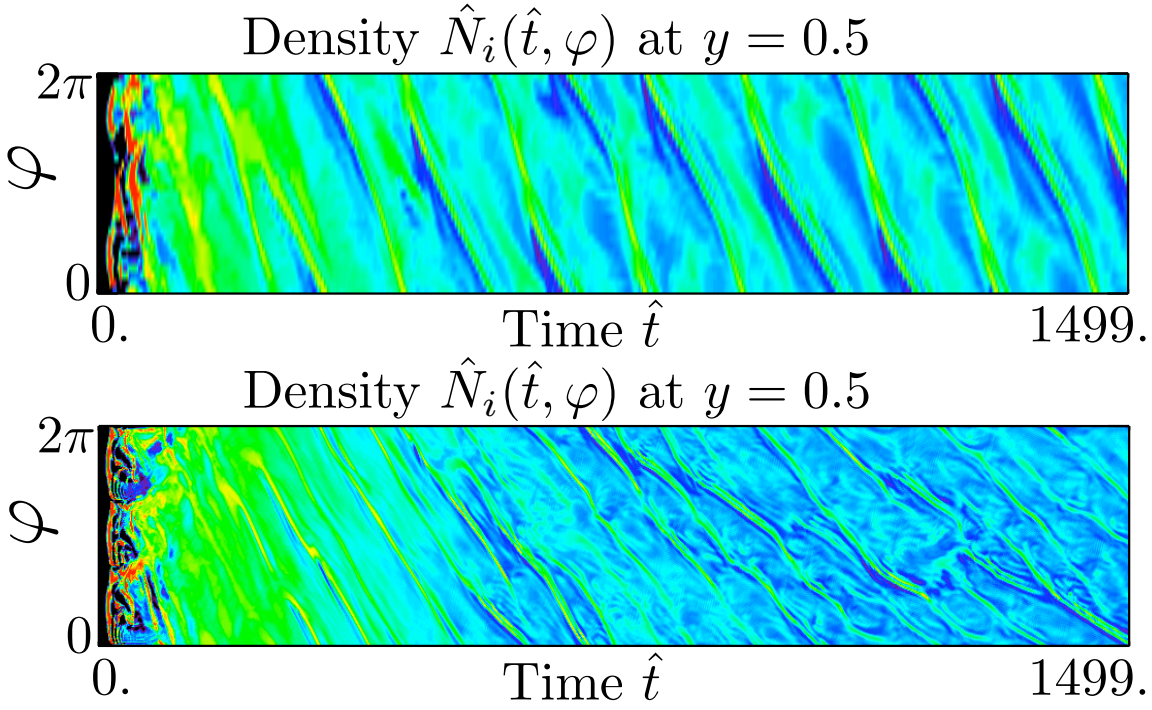

Figure 5.7: The non-dimensionalized density $\hat{N}_i$ measured at y = 0.5 (L=54 cm), and around the plasma azimuth for Mx = 30 and Mx = 200. Large-scale structures rotate around in the negative azimuthal direction, as measured in CTX. Coherent structures are seen to merge and split similar to Fig.4.11.

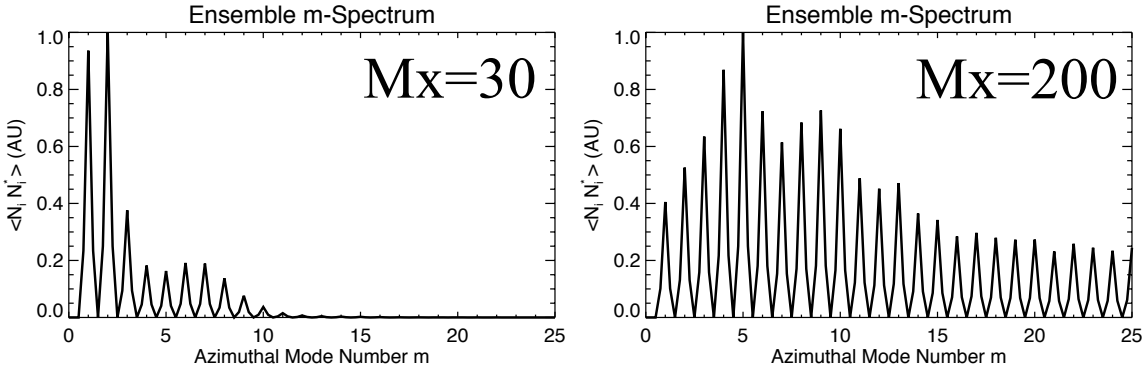

Figure 5.8: The ensemble azimuthal mode number spectrum for Mx = 30 and Mx = 200. As the azimuthal grid is refined, the dominant structures tend to increase in wavelength from $m = 1, 2$ to $m = 5$.

Using the same numerical techniques detailed in Sec.3, the spectral trends of potential and density have been calculated. Displayed in Fig.5.9 are both a single time series of potential fluctuations, and the associated spectrum $\hat{\Phi}\hat{\Phi}^*$ taken at an equivalent radial location in the plasma. The spectral trend of potential fluctuations displays the same power-law scaling $\hat{\Phi}\hat{\Phi}^* \sim f^{-5}$ as the observation in CTX (Fig.4.3). The density, which displays more fine structure, has a less-steep spectral trend of $\hat{N}_i\hat{N}_i^* \sim f^{-3}$, which is also in agreement with the observation in CTX. Both of these spectral trends are in agreement with the expectations of two-dimensional turbulence, and the experimental results of Sec.4.8.

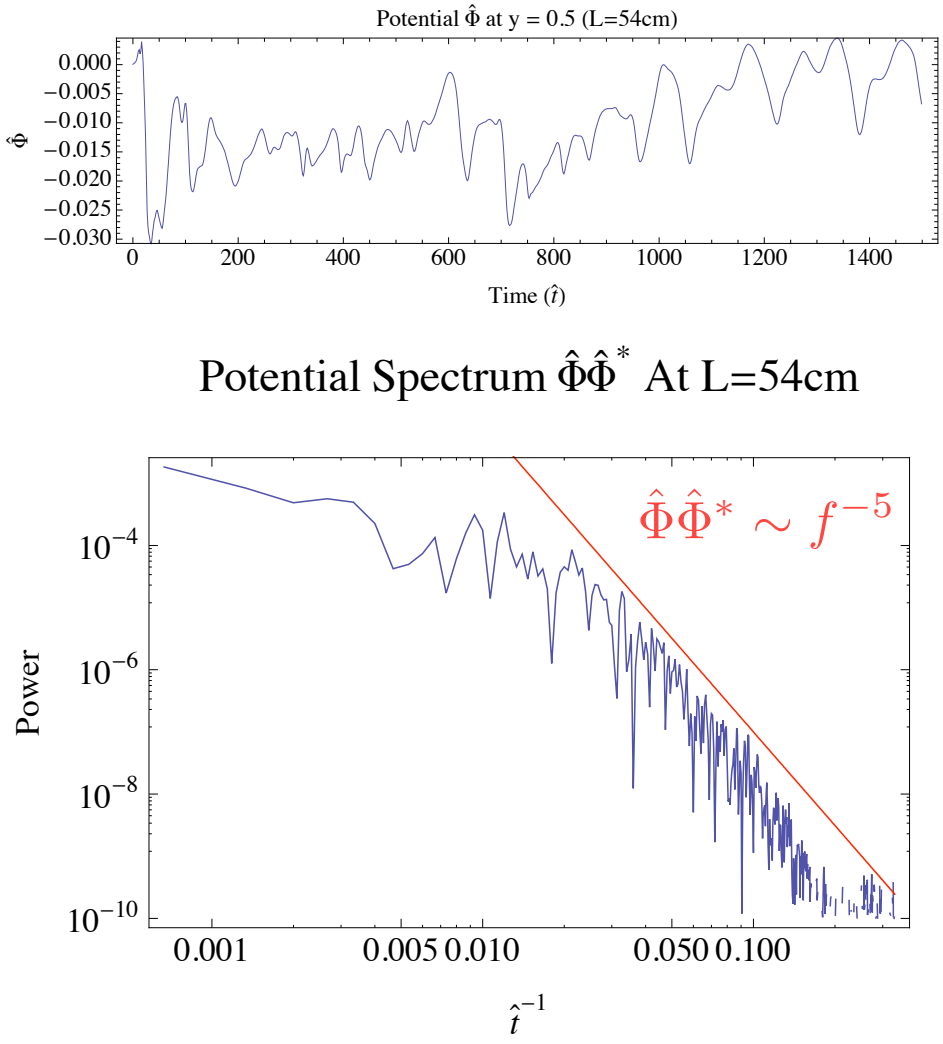

Figure 5.9: A time trace and associated spectrum for potential fluctuations. The potential displays smooth traces with little fine structure. The power spectrum follows a f^{-5} power-law.

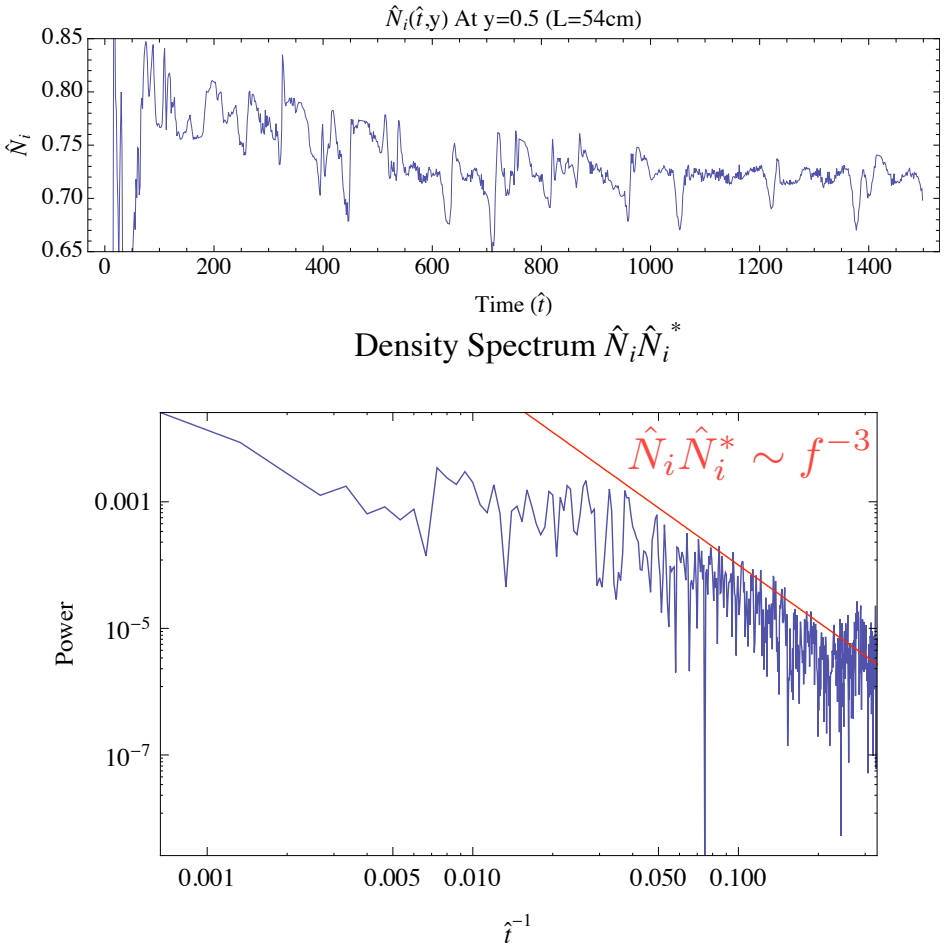

Figure 5.10: A time trace and associated spectrum for density fluctuations. The density displays much more fine structure than the potential, resulting in a power spectrum which is less steep. The power spectrum is seen to follow a f^{-3} power-law.

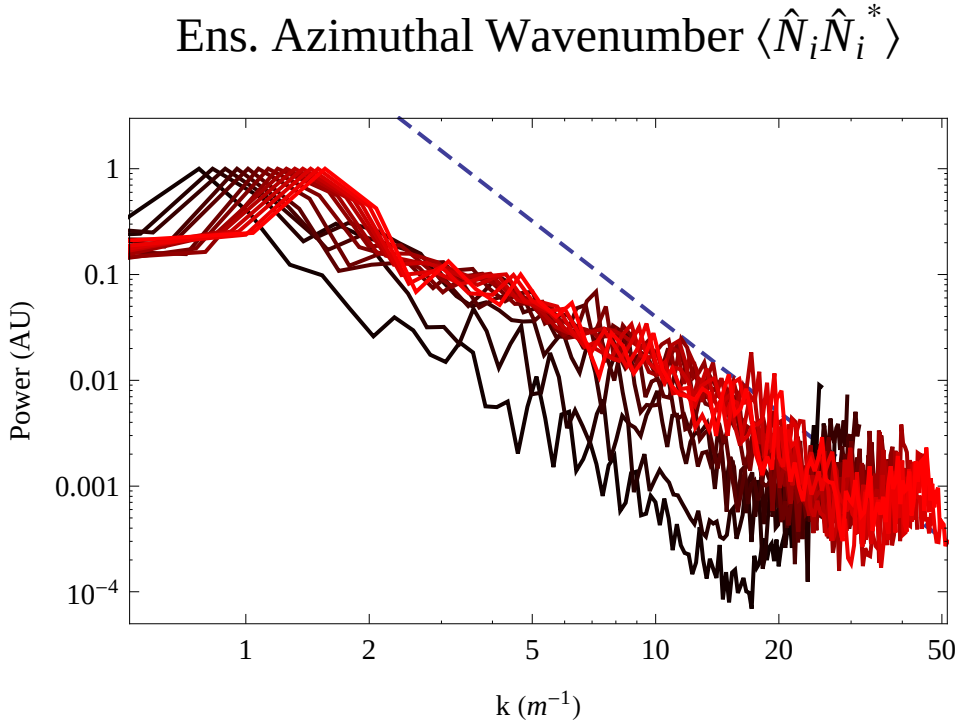

Figure 5.11: Ensemble wavenumber spectrum taken across the outboard computational domain from $L = [62 : 30]$ cm (blk-red). The power spectrum is seen to follow an approximate f^{-3} power-law most accurately for the outboard (darker) measurements.

5.4 Summary of Simulation Results

New additions to a successful dipole magnetic field-confined hot electron plasma simulation have achieved quasi-steady turbulence. The high-performance parallel simulation of driven interchange turbulence reproduces many of the features observed in the laboratory. The parallelization of the software and inclusion of a conserving source and sink provides a tool which is used to test the model equations. Both laboratory observations and simulation results are consistent with two-dimensional, cross-field interchange mixing driven at marginal stability. The simulation accurately captures the dynamics of rotating, long wavelength density and potential structures, in agreement with experimental observations. Furthermore, the spectral trends of density $\tilde{N}\tilde{N}^* \sim k^{-3}$ and potential $\tilde{\Phi}\tilde{\Phi}^* \sim k^{-5}$ agree with the predictions for two-dimensional enstrophy cascading, and are also consistent with experimental observations. However, as the grid is continuously refined, the dominant structures increase in wavenumber (Fig.5.8). As a suggestion for future work, apply the statistical treatment of spectral energy transfer to long time series obtained from long-time turbulence simulations on more sophisticated architectures. These results may be used to further test the model equations to determine the consistency between the spectral cascade trends and the inverse energy, forward enstrophy cascade for two-dimensional turbulence.

Chapter 6

Conclusion

Understanding turbulence in fluids and plasmas remains a challenge for theory, experimentation, and simulation. Turbulent processes have broad impact on fields such as fluid dynamics, plasma physics, astrophysics, combustion, atmospheric and earth sciences. In magnetic fusion plasmas, turbulent energy transfer and structure coupling remain primary candidates for generating shearing zonal flows and transport barriers. The formation of transport barriers achieves enhanced confinement regimes in modern tokamaks and is necessary for the feasibility of fusion energy. Advancements in understanding the generation of turbulence and the associated transport of particles, heat, and momentum requires thorough measurements of plasma parameters and fluctuations. This thesis reports the local and global spatial and temporal characteristics of plasma turbulence in a magnetic dipole for the first time. Using newly installed diagnostic capabilities, the plasma parameters, profiles and dynamics are measured, and long-time data records are statistically analyzed. These comprehensive measurements of the dipole-confined plasmas in CTX show that the turbulence consists of rotating, two-dimensional interchange modes.

6.1 Discussion of Results

The field-aligned wavelength and coherence confirms the dominance of the interchange mechanism for cross-field mixing, and strengthens the presumption of the two-dimensional nature of the dynamics. The local measurements are consistent with fully developed turbulence, with power-law spectral trends, quickly decaying auto-correlation functions, and a lack of fully coherent modes in the plasma. When viewed globally, ensemble statistics of cross-correlation, cross-coherence and phase reveal evidence of long-range correlation and quasi-coherence of low-order azimuthal modes. This remains a feature of two-dimensional turbulence, and turbulence in general: the existence of coherent structures in a fully turbulent medium. These quasi-coherent structures are responsible for the majority of the fluctuation induced particle flux, and can form the basis of understanding nonlinear phenomena such as intermittent "blob" transport in plasmas.

The polar imaging diagnostic and amplifier upgrades provide multi-point global measurements of density fluctuations at high temporal resolution, and spatial resolution within the correlation length of the fluctuations. Globally, plasma dynamics are observed to evolve by relatively simple, large-scale, radially broad, sine and cosine-like modes which represent the "self-organized" state of dipole-confined plasma turbulence. It is the chaotic temporal variation of these global structures which produces locally measured fluctuations that appear with a power-law frequency spectrum trend that peaks at low frequencies, while having the spectral density usually associated with "classical turbulence". The Lyapunov exponent analysis indicates that nearby trajectories in phase space diverge exponentially on a timescale near 40 μs. This phase-space divergence manifests itself as a decorrelation of fluctuations before the plasma rotates once around the device azimuthally. These properties of the large-scale, global modes are indeed evocative of Rayleigh-Bérnard convection in fluids. Rayleigh-Bérnard convection is a driven flow which can have chaotic convection patterns describable by a Lorenz model. There is a know plasma equivalent in flute modes explored theoretically by Rypdal and Garcia [77] and investigated experimentally by Živković and

Rypdal [95].

The broad power-law frequency spectrum and the dominance of just a few large-scale modes are two views of interchange turbulence that are not paradoxical. They are consistent in that they join together two spatial scales: the large global scale and the smaller scale associated with viscous or collisional damping. We observe the small scale of the damped fluctuations, which disappear too quickly to become global observables, and relinquish their fluctuation energy to lower wavenumbers at the large-scale. The scale of the large structures is on the order of the system size, possesses azimuthal mode numbers $m < 4$, and receives energy from the higher wavenumbers. The energy cascade is the process which connects these two scales, generates the large-scale, global structures, and determines the power-law spectrum.

The spectral trend of the fluctuation energy corresponds to the forward enstrophy, inverse energy cascade for a two-dimensional turbulent fluid. The converged estimator of nonlinear power transfer through three-wave interaction provides further evidence that the observed quasi-coherent structures are the direct result of an inverse energy cascading process. The amplitude correlation between the marginally damped region of the spectrum and the quasi-coherent modes provides corroborating evidence. Thus the inverse energy cascade originally proposed by Robert Kraichnan in 1967 [51] is a likely candidate for the generation and sustainment of long wavelength modes in CTX.

A fully parallelized, self-consistent nonlinear simulation has been used to test the model equations. The simulation achieves a quasi-steady driven turbulent state. The combination of a source and sink of ion and electron number density and electron energy achieves a balance at marginal stability, with a density profile in agreement with observations in CTX. Density and potential fluctuations are computed to be dominated by rotating, radially broad, long wavelength azimuthal modes which are also observed experimentally.

6.2 Opportunities for Future Research

This thesis also reports the observation and identification of large, convective-like structure generation in an open field-line configuration. The nonlinear dynamics of these structures contributes to the body of knowledge for understanding the convective 'blob' structures at the edge of tokamaks where the field-lines are open. Because of its large plasma volume and diagnostic access, the CTX device may serve as a testbed for a tokamak disruption mitigation mechanism which produces local convective cells in the scrape-off layer [18, 78, 19]. These convective cells are generated by biasing poloidally neighboring flux tubes. The application of a voltage bias creates a controllable-rate radial convective mechanism through a poloidal electric field. This is one testable option for reducing the heat flux which can damage the material wall of a fusion reactor.

The work in this thesis provides experimental evidence for the two-dimensional dual cascade of energy and enstrophy. Further investigation into the interrelationship of energy injection, or 'pumping', and the inverse energy cascade may be possible by seeding the plasma with a high-frequency electrostatic perturbation. Equivalently, an array of phase-shifted, closely spaced probes may indeed inject energy directly into the high wavenumber region. Because the plasma is rotating, the same nonlinear power transfer calculations performed in this thesis can be used by probe-pairs situated 'downstream' from the azimuthal location of the energy injection. Thus, by varying either the frequency or wavenumber of the pump wave, the spectral cascade may be viewed over a wider range of spatial scales between the injection and condensate.

Appendix A

Velocity-Vorticity Formulation of Navier-Stokes Equation

The Navier-Stokes equation is

$$\frac{D\vec{u}}{Dt} = \frac{\partial \vec{u}}{\partial t} + (\vec{u}\cdot\nabla)\vec{u} = -\frac{1}{\rho}\nabla p + \vec{f_{ext}} + \nu\nabla^2\vec{u} \tag{A.1}$$

where term by term, we have unsteady acceleration, convective acceleration, pressure gradient, body forces, and viscosity. We will consider the two-dimensional case in $\hat{x}, \hat{y}$. The vorticity is defined as $\vec{\omega} = \nabla \times \vec{u} = \omega\hat{z}$. Taking the curl of Eq.A.1, the first term on the LHS is

$$\nabla \times \frac{\partial \vec{u}}{\partial t} = \frac{\partial \vec{\omega}}{\partial t} \tag{A.2}$$

The second term on the LHS is

$$\begin{aligned} \nabla \times (\vec{u}\cdot\nabla)\vec{u} &= \nabla \times \left[\nabla\Big(\frac{|\vec{u}|^2}{2}\Big) + (\nabla\times\vec{u})\times\vec{u}\right] \\ &= -\nabla\times(\vec{u}\times\vec{\omega}) \\ &= -\Big[\cancel{\vec{u}(\nabla\cdot\vec{\omega})} + \cancel{\vec{\omega}(\nabla\cdot\vec{u})} + \cancel{(\vec{\omega}\cdot\nabla)\vec{u}} - (\vec{u}\cdot\nabla)\vec{\omega}\Big] \end{aligned} \tag{A.3}$$

and the first, second, and third terms can be eliminated by the vector identity $\nabla \cdot \nabla \times (\vec{\star}) \equiv 0$, incompressibility $\nabla \cdot \vec{u} = 0$, and the two-dimensional assumption, respectively. This leaves the LHS as

$$\frac{\partial \vec{\omega}}{\partial t} + (\vec{u} \cdot \nabla)\vec{\omega} = \frac{D\vec{\omega}}{Dt} \tag{A.4}$$

The RHS is, for constant ρ,

$$\nabla \times -\frac{1}{\rho}\nabla p = 0 \tag{A.5}$$

by $\nabla \times \nabla(\star) \equiv 0$. The body force term is simply $\nabla \times \vec{f_{ext}} \cdot \hat{z} = g$. The viscous contribution is, for constant ν,

$$\begin{aligned} \nabla \times \nu\nabla^2\vec{u} &= \nu\nabla \times \left[\cancel{\nabla(\nabla \cdot \vec{u})} - \nabla \times \nabla \times \vec{u}\right] \\ &= \nu\nabla \times (-\nabla \times \vec{\omega}) \\ &= \nu[\,-\cancel{\nabla(\nabla \cdot \vec{\omega})} + \nabla^2\vec{\omega}] \\ &= \nu\nabla^2\vec{\omega} \end{aligned} \tag{A.6}$$

Therefore, in the two-dimensional velocity-vorticity formulation, the Navier-Stokes equation for vorticity $\vec{\omega} = \omega\hat{z}$ becomes

$$\frac{\partial \omega}{\partial t} + (\vec{u} \cdot \nabla)\omega = g + \nu\nabla^2\omega \tag{A.7}$$

The kinetic energy per unit mass is

$$E = \frac{1}{2}\langle \vec{u}^2 \rangle \tag{A.8}$$

and the evolution is given as [83]

$$\frac{DE}{Dt} = \frac{1}{2}\frac{D\vec{u}^2}{Dt} = -\nu Z \tag{A.9}$$

where $Z = \langle \omega^2 \rangle$. Therefore energy is conserved in the inviscid case. For the enstrophy evolution,

$$\frac{DZ}{Dt} = -\nu \langle (\nabla \omega)^2 \rangle \tag{A.10}$$

which is also conserved in the inviscid case.

Appendix B

Basic Probe Theory

B.1 Langmuir Probes

The Langmuir probe, named for Columbia University graduate and Nobel Prize winning physicist Irving Langmuir, is simply a material electrode inserted into a plasma and biased with a voltage different from other electrodes or from the containing vessel.

Foregoing the full derivation [43], the Debye sheath between the plasma and a material has the property that ions pass through the sheath with the sound speed in the plasma, where

$$C_s = \sqrt{\frac{T_e + \gamma_i Z T_i}{M}} \tag{B.1}$$

and is usually approximated as $C_s = \sqrt{T_e/M}$ when the ions can be assumed cold.

The current density is always given as $j = qnv$, where the ion current is $j_i = en_iC_s$. Because net current is always what is measured, Langmuir probes are biased sufficiently negative such that only ions are collected (usually a few times the electron temperature T_e). When this condition is met, the collected current is called the *ion saturation current*, or I_{sat}, and is directly proportional to density, but varies more weakly with temperature as $\sqrt{T_e}$. Quasineutrality allows us to write this as $j = en_eC_s$ since $n_i \approx n_e$.

The electrons can be modeled as Boltzmann in one dimension, where

$$f_e(v_x)dv_x \propto \exp\Big(-\frac{W}{k_BT}\Big) = \exp\Big(-\frac{mv_x^2/2}{k_BT}\Big) \tag{B.2}$$

and only higher energy electrons can overcome the potential hill set up by the negative sheath potential. The mean velocity is

$$\bar{v_e} = \frac{\int_{v_{e0}}^{\infty} f_e(v_x)v_x dv_x}{\int_{v_{e0}}^{\infty} f_e(v_x)dv_x} \tag{B.3}$$

where v_{e0} is given by setting the kinetic energy equal to the electrostatic energy $q\Phi$.

$$v_{e0} = \sqrt{\frac{2e\Phi_{sh}}{m_e}} \tag{B.4}$$

resulting in

$$\bar{v_e} = \sqrt{\frac{k_BT_e}{2\pi m_e}}e^{-e\Phi_{sh}/k_BT_e} \tag{B.5}$$

Now, using $j_{isat} = en_eC_s$ and our expression for $\bar{v_e}$, we can write

$$j_e = j_{isat}\sqrt{\frac{M}{2\pi m_e}}e^{-e\Phi_{sh}/k_bT_e} \tag{B.6}$$

The total current is then $j = j_e - j_{isat}$,

$$j = j_{isat}\Big(-1 + \sqrt{\frac{M}{2\pi m_e}}e^{-e\Phi_{sh}/k_bT_e}\Big) \tag{B.7}$$

B.2 The Single-Electrode Langmuir Probe

The single electrode Langmuir probe is simply a metallic wire inserted into a plasma, with a DC or AC voltage applied to the tip. When the voltage is DC and sufficiently negative, this is called an I_{sat} probe, which measures the ion saturation current through the plasma sheath.

That current is

$$j_{isat} = en_eC_s \tag{B.8}$$

which is a current density. The current which will be measured electronically is the total current, $I = Aj$, where A is the area through which that current density flows. This area is usually larger than the physically measured area of the probe, because the sheath thickness is nonzero. If the temperature fluctuations are assumed negligible compared to density fluctuations, it is common to assume $I_{isat} \propto n$.

For a sinusoidal or triangle waveform variation of the bias voltage, the $I - V$ characteristics of the plasma can be obtained. This is the response of the collected current to the applied bias to the electrode. The floating potential is the zero current crossing voltage point where the current is zero. For voltages below the floating potential, more ions are collected than electrons. For voltages above this, exponentially greater electrons are collected for increasing voltage. This characteristic of increasing the bias voltage allows one to extract the electron temperature T_e. Using

$$I(V) = I_{isat}\Big(- 1 + e^{e(V-V_f)/k_BT_e}\Big) \tag{B.9}$$

and taking the natural logarithm, we arrive at

$$ln(I(V) + I_{isat}) = \frac{V - V_f}{k_B(T_e/e)} \tag{B.10}$$

and therefore the slope of the log of the $I - V$ curve in the region above V_f is $1/(T_e/e)$, where T_e/e has units Volts.

The electron temperature in CTX is $T_e \approx 5 - 10$ eV as calculated by a simple triangle waveform swept langmuir probe. This is in agreement of the triple probe electron temperature measurements.

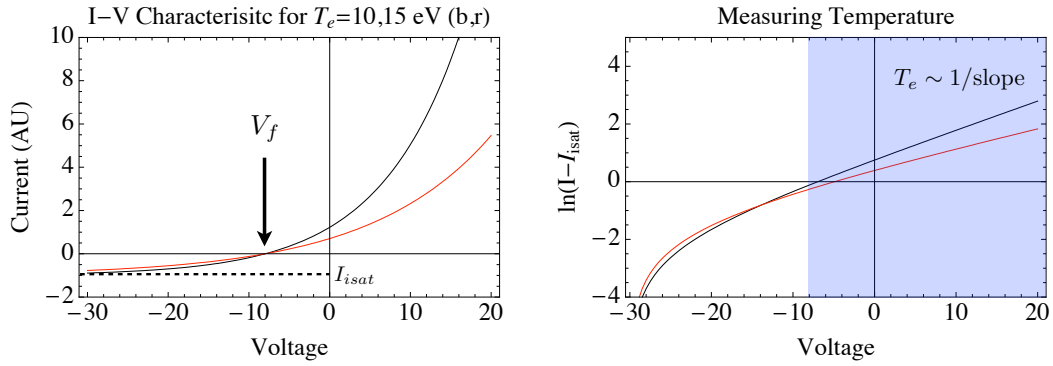

Figure B.1: A current-voltage trace for a swept langmuir probe in a plasmas with floating potential of -8 V and having $T_e = 10, 15$ eV. For V ≥ -8V the log current plot takes on a linear relationship.

B.3 Double Probe

A double probe [43] is two langmuir probes, biased with respect to each other rather than the vessel which contains the plasma. In this case, the two probes measure equal and opposite current

$$I = I_{isat}\left(-1 + e^{e(V_2 - V_f)/k_B T_e} \right) = -I_{isat}\left(-1 + e^{e(V_1 - V_f)/k_B T_e} \right) \tag{B.11}$$

which can be written as

$$I = I_{isat} \tanh\left(\frac{eV_B}{2k_B T_e} \right) \tag{B.12}$$

where $V_B = V_2 - V_1$.

B.4 Triple Probe

A triple probe [43, 23] is similar to a double probe, with the addition of a third tip to directly measure the floating potential. The bias voltage is chosen to be a few times T_e so that the negative tip draws I_{isat}, and the other tip draws the (normally negative) positive I_{isat}.

Therefore

$$\begin{aligned} I_{isat} &= I_{isat}\Big(-1 + e^{e(V_+ - V_f)/k_B T_e}\Big) \\ 2 &= \exp\Big[\frac{V_+ - V_f}{k_B T_e/e}\Big] \end{aligned} \tag{B.13}$$

or

$$(V_+ - V_f) = \ln(2) k_B T_e/e \tag{B.14}$$

Thus the triple probe provides three points on the $I - V$ probe characteristic. The electron temperature is directly measured in eV as $T_e = (V_+ - V_f)/\ln(2)$. The triple probe therefore measures three basic plasma parameters (V_f, n_e, T_e) simultaneously. Density is calculated from $I_{isat} = A e n_e C_s$

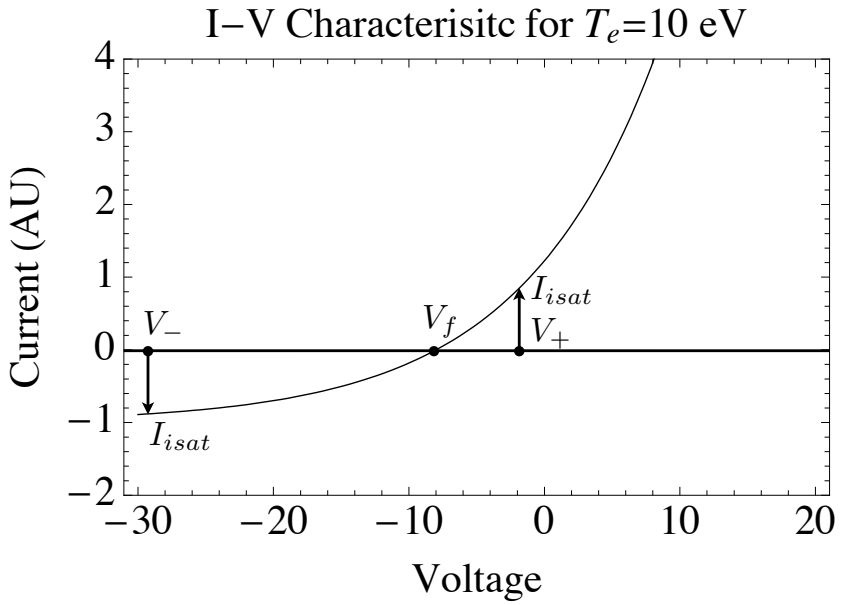

Figure B.2: A current-voltage trace for a swept langmuir probe in a plasmas with floating potential of -8 V and having T_e = 10 eV. The temperature is calculated from the difference between the floating potential and the positively biased probe tip.

Appendix C

Finite Difference For Spectral Energy Transfer

Consider the simple system

$$\frac{\partial \phi(t)}{\partial t} = a\phi(t) \tag{C.1}$$

$$\phi(t) = |\phi(t)|e^{i\Theta(t)} \tag{C.2}$$

Using the second in the first, we have

$$\frac{\partial}{\partial t}(|\phi|)e^{i\Theta} + |\phi|e^{i\Theta}\frac{\partial}{\partial t}(i\Theta) = a\phi \tag{C.3}$$

so

$$\frac{\partial |\phi|}{\partial t} = -|\phi|\frac{\partial (i\Theta)}{\partial t} + a\phi e^{-i\Theta} \tag{C.4}$$

and $|\phi| = \phi e^{-i\Theta}$.

$$\frac{\partial}{\partial t}(\phi e^{-i\Theta}) = -\phi e^{-i\Theta}\frac{\partial (i\Theta)}{\partial t} + a\phi e^{-i\Theta} \tag{C.5}$$

Taking the finite-difference form of the LHS, we have

$$\frac{\partial \phi(t) e^{-i\Theta(t)}}{\partial t} \approx \lim_{\tau \to 0} \left(\frac{\phi(t+\tau) e^{-i\Theta(t+\tau)} - \phi(t) e^{-i\Theta(t)}}{\tau} \right) \tag{C.6}$$

Therefore,

$$\begin{aligned}
\phi(t+\tau) e^{-i\Theta(t+\tau)} - \phi(t) e^{-i\Theta(t)} &= \tau \Big[- \phi(t) e^{-i\Theta(t)} \frac{\partial (i\Theta(t))}{\partial t} + a \phi(t) e^{-i\Theta(t)} \Big] && \text{(C.7)} \\
\phi(t+\tau) e^{-i\Theta(t+\tau)} &= \phi(t) e^{-i\Theta(t)} \Big[- \tau \frac{\partial (i\Theta(t))}{\partial t} + a\tau + 1 \Big] && \text{(C.8)} \\
\phi(t+\tau) &= \phi(t) e^{-i\Theta(t)} e^{i\Theta(t+\tau)} \Big[- \tau \frac{\partial (i\Theta(t))}{\partial t} + a\tau + 1 \Big] && \text{(C.9)} \\
&= \frac{a\tau + 1 - \tau \frac{\partial (i\Theta(t))}{\partial t}}{e^{-i[\Theta(t+\tau) - \Theta(t)]}} \phi(t) && \text{(C.10)} \\
&= \frac{a\tau + 1 - i[\Theta(t+\tau) - \Theta(t)]}{e^{-i[\Theta(t+\tau) - \Theta(t)]}} \phi(t) && \text{(C.11)}
\end{aligned}$$

Appendix D

Search Algorithm For Embedded Neighbors

To find neighbors in the space $\mathbb{R}^{d_E}$ in a quick way, we replace the Euclidean norm with

$$||\mathbf{x}_j - \mathbf{x}_i|| \leq r \longrightarrow ||\mathbf{x}_j - \mathbf{x}_i|| = \max_{0\leq\alpha\leq d_E-1}\{|x_{j+\alpha} - x_{i+\alpha}|\}$$

We sort the x_i such that

$$x_{\Pi(1)} \leq x_{\Pi(2)} \leq \ldots \leq x_{\Pi(n)}$$

where Π is the permutation matrix. Store Π and its inverse Π^{-1}. We find neighbors of x_i in the first embedded dimension by starting with $k = \Pi^{-1}(i)$ (or the position where Π equals i) and scan the $x_{\Pi(s)}$ for $s = k+1, k+1, \ldots$ until the distance $d = x_{\Pi(s)} - x_i$ is larger than r. Do the same for $s = k-1, \ldots$ where $d = x_i - x_{\Pi(s)}$. Store those good j's that satisfy the norm condition. Then, searching those good j's, repeat the procedure for $d = |x_{\Pi(s)+\alpha} - x_{i+\alpha}|$. This search algorithm results in the set $S_i(r)$ of j indices where a neighbor exists in a d_E-dimensional sphere.

Appendix E

Bibliography

[1] HDI Abarbanel, R Brown, JJ Sidorowich, and LS Tsimring. The analysis of observed chaotic data in physical systems. *Reviews of Modern Physics*, 65(4):1331–1392, 1993.

[2] H Aref. Integrable, chaotic, and turbulent vortex motion in two-dimensional flows. *Ann. Rev. Fluid Mech.*, 15:345–389, Jan 1983.

[3] A. Y Aydemir. Convective transport in the scrape-off layer of tokamaks. *Phys. Plasmas*, 12:062503, Jan 2005.

[4] P Bak, C Tang, and K Wiesenfeld. Self-organized criticality: An explanation of the 1/f noise. *Phys. Rev. Lett.*, 59(4):381–384, Jan 1987.

[5] Charles Baker, Stewart Prager, Mohamed Abdou, Lee Berry, Riccardo Betti, Vincent Chan, Darren Craig, Jill Dahlburg, Ronald Davidson, James Drake, Richard Hawryluk, David Hill, Amanda Hubbard, Grant Logan, Earl Marmar, Michael Mauel, Kathryn Mccarthy, Scott Parker, Ned Sauthoff, Ronald Stambaugh, Michael Ulrickson, James Van Dam, Glen Wurden, Michael Zarnstorff, and Steven Zinkle. Scientific challenges, opportunities and priorities for the u.s. fusion energy sciences program. *J. Fus. Energ.*, 24(1/2):13–114, Jun 2005.

[6] Satish Balay, Kris Buschelman, Victor Eijkhout, William D. Gropp, Dinesh Kaushik, Matthew G. Knepley, Lois Curfman McInnes, Barry F. Smith, and Hong Zhang. PETSc users manual. Technical Report ANL-95/11 - Revision 2.1.5, Argonne National Laboratory, 2004.

[7] Satish Balay, Kris Buschelman, William D. Gropp, Dinesh Kaushik, Matthew G. Knepley, Lois Curfman McInnes, Barry F. Smith, and Hong Zhang. PETSc Web page, 2001. http://www.mcs.anl.gov/petsc.

[8] Satish Balay, William D. Gropp, Lois Curfman McInnes, and Barry F. Smith. Efficient management of parallelism in object oriented numerical software libraries. In E. Arge, A. M. Bruaset, and H. P. Langtangen, editors, *Modern Software Tools in Scientific Computing*, pages 163–202. Birkhäuser Press, 1997.

[9] D. A Baver and P. W Terry. Basis function multifield bispectral deconvolution analysis. *Phys. Plasmas*, 12:042303, Jan 2005.

[10] J Beall, Y Kim, and E Powers. Estimation of wavenumber and frequency spectra using fixed probe pairs. *J. Appl. Phys.*, 53(6):3933–3940, Jan 1982.

[11] H Berk. Stability of hot electron plasmas. *Physics of Fluids*, 19(8):1255–1256, Jan 1976.

[12] R Bravenec, K Gentle, B Richards, and D Ross. Core turbulence and transport studies on the texas experimental tokamak. *Phys. Fluids B: Plasma Physics*, 4(7):2127–2135, Jan 1992.

[13] M. J Burin, G. R Tynan, G. Y Antar, N. A Crocker, and C Holland. On the transition to drift turbulence in a magnetized plasma column. *Phys. Plasmas*, 12:052320, Jan 2005.

[14] S Camargo, D Biskamp, and B Scott. Resistive drift-wave turbulence. *Phys. Plasmas*, 2(1):48–62, Jan 1995.

[15] D L Carpenter and R R Anderson. An isee/whistler model of equatorial electron density in the magnetosphere. *J. Geophys. Res.*, 97(A2):1097–1108, Jan 1992.

[16] A Chan. Noncanonical hamiltonian methods for particle motion in magnetospheric hydromagnetic waves. *J. Geophys. Res.*, 103(A9):20,501–20,513, Jan 1998.

[17] J Chiu and A Sen. Experimental determination of attractor dimension of e b turbulence. *Phys. Plasmas*, 7(11):4492–4498, Jan 2000.

[18] R Cohen and D Ryutov. Plasma convection induced by toroidal asymmetries of the divertor plates and gas puffing. *Nucl. Fusion*, 37(5):621–627, Jan 1997.

[19] R H Cohen, D D Ryutov, G F Counsell, and P Helander. Current and potential distribution in a divertor with toroidally-asymmetric biasing of the divertor plate. *Plasma Phys. Control. Fusion*, 49:1–13, Nov 2007.

[20] FJ Crossley, P Uddholm, P Duncan, M Khalid, and MG RUSBRIDGE. Experimental study of drift-wave saturation in quadrupole geometry. *Plasma Phys. Control. Fusion*, 34:235–262, 1992.

[21] Amita Das. Relaxation and self-organization in two-dimensional plasma and neutral fluid flow systems. *Phys. Plasmas*, 15(2):022308, Jan 2008.

[22] T Dudok de Wit, A Pecquet, J Vallet, and R Lima. The biorthogonal decomposition as a tool for investigating fluctuations in plasmas. *Phys. Plasmas*, 1(10):3288–3229, Jan 1994.

[23] V Demidov, S Ratynskaia, and K Rypdal. Electric probes for plasmas: The link between theory and instrument. *Review of Scientific Instruments*, 7(10):3409–3439, Jan 2002.

[24] R O Dendy and S C Chapman. Characterization and interpretation of strongly nonlinear phenomena in fusion, space and astrophysical plasmas. *Plasma Phys. Control. Fusion*, 48(12B):B313–B328, Nov 2006.

[25] P H Diamond, S-I Itoh, K Itoh, and T S Hahm. Zonal flows in plasma—a review. *Plasma Phys. Control. Fusion*, 47:R35–R161, Apr 2005.

[26] C Driscoll and K Fine. Experiments on vortex dynamics in pure electron plasmas. *Physics of Fluids B: Plasma Physics*, 2(6):1359–1366, Jan 1990.

[27] J P Eckmann, S Oliffson Kanphorst, and D Ruelle. Recurrence plots of dynamical systems. *Europhysics Letters*, 4(9):937–977, 1987.

[28] JP Eckmann, SO Kamphorst, D Ruelle, and S Ciliberto. Liapunov exponents from time series. *Phys. Rev. A*, 34(6):4971–4979, 1986.

[29] G Falkovich and K Sreenivasan. Lessons from hydrodynamic turbulence. *Physics Today*, April:43–49, Mar 2006.

[30] A Fasoli, B Labit, M Mcgrath, S. H Müller, G Plyushchev, M Podestà, and F. M Poli. Electrostatic turbulence and transport in a simple magnetized plasma. *Phys. Plasmas*, 13:055902, Jan 2006.

[31] Jeffrey Freidberg. *Plasma Physics and Fusion Energy*. Cambridge University Press, 2007.

[32] O E Garcia, J Horacek, R A Pitts, A H Nielsen, W Fundamenski, J P Graves, V Naulin, and J Juul Rasmussen. Interchange turbulence in the tcv scrape-off layer. *Plasma Phys. Control. Fusion*, 48:L1–L10, Dec 2005.

[33] D Garnier. Magnetohydrodynamic stability in a levitated dipole. *Phys. Plasmas*, 6(9):3431–3432, Jan 1999.

[34] T S Hahm, W W Lee, and A Brizard. Nonlinear gyrokinetic theory for finite-beta plasmas. *Physics of Fluids*, 31(7):1940–1948, Jan 1988.

[35] F Harris. On the use of windows for harmonic analysis with the discrete fourier transform. *Proc. IEEE*, 66(1):51–83, Jan 1978.

[36] A Hasegawa. Self-organization processes in continuous media. *Advances in Physics*, 34(1):1–42, Jan 1985.

[37] A Hasegawa, C Maclennan, and Y Kodama. Nonlinear behavior and turbulence spectra of drift waves and rossby waves. *Physics of Fluids*, 21(11):2122–2129, Jan 1979.

[38] A Hasegawa and K Mima. Stationary spectrum of strong turbulence in magnetized nonuniform plasma. *Phys. Rev. Lett.*, 39(4):205–208, Jan 1977.

[39] A Hasegawa and M Wakatani. Self-organization of electrostatic turbulence in a cylindrical plasma. *Phys. Rev. Lett.*, 59(14):1581–1584, 1987.

[40] W Horton. Drift waves and transport. *Reviews of Modern Physics*, 71(3):735–778, Jan 1999.

[41] W Horton and A Hasegawa. Quasitwodimensional dynamics of plasmas and fluids. *Chaos*, 4(2):227–251, Jan 1994.

[42] N Huang. The empirical mode decomposition and the hilbert spectrum for nonlinear and non-stationary time series analysis. *Proc. R. Soc. Lond. A*, 454(1971):903–995, Jan 1998.

[43] I. H. Hutchinson. *Principles of Plasma Diagnostics*. Cambrige University Press, 2002.

[44] R Jha, D Raju, and A Sen. Analysis of tokamak data using a novel hilbert transform based technique. *Phys. Plasmas*, 13:082507, Jan 2006.

[45] P Julian, W Washington, L Hembree, and C Ridley. On the spectral distribution of large-scale atmospheric kinetic energy. *J. Atmos. Sci.*, 27:376–387, Jan 1970.

[46] J Kesner and D Garnier. Convective cell formation in a levitated dipole. *Phys. Plasmas*, 7(6):2733–2737, Jan 2000.

[47] J Kesner, D.T Garnier, A Hansen, M Mauel, and L Bromberg. Helium catalysed d–d fusion in a levitated dipole. *Nucl. Fusion*, 44(1):193–203, Dec 2003.

[48] J Kim, R Durst, R Fonck, E Fernandez, and A Ware. Technique for the experimental estimation of nonlinear energy transfer in fully developed turbulence. *Phys. Plasmas*, 3(11):3998–4009, Jan 1996.

[49] Y Kim, J Beall, E Powers, and R Miksad. Bispectrum and nonlinear wave coupling. *Physics of Fluids*, 23(2):258–263, Jan 1980.

[50] T Klinger, F Greiner, A Latten, A Piel, T Pierre, G Bonhomme, C Arnas Capeau, G Bachet, and F Doveil. Nonlinear dynamics and chaos in gas discharge systems. *J. Phys. IV France*, 5(C6):C6–131–C6–136, Oct 1995.

[51] RH Kraichnan. Inertial ranges in two-dimensional turbulence. *Physics of Fluids*, 10(7):1417–1423, 1967.

[52] N A Krall. Stabilization of hot electron plasma by a cold background. *Physics of Fluids*, 9(4):820–821, Feb 1966.

[53] K Krushelnick and S Cowley. Physics: Enhanced: Reduced turbulence and new opportunities for fusion. *Science*, 309:1502–1503, Jan 2005.

[54] P. K. Kundu, I. M. Cohen. *Fluid Mechanics*. Academic Press, fourth edition, 2008.

[55] B Levitt. Global mode analysis of centrifugal and curvature driven interchange instabilities. *Ph.D Thesis*, Jul 2004.

[56] B Levitt, D Maslovsky, and M Mauel. Measurement of the global structure of interchange modes driven by energetic electrons trapped in a magnetic dipole. *Phys. Plasmas*, 9(6):2507–2517, Jan 2002.

[57] B Levitt, D Maslovsky, and M. E Mauel. Observation of centrifugally driven interchange instabilities in a plasma confined by a magnetic dipole. *Phys. Rev. Lett.*, 94:175002, May 2005.

[58] B Levitt, D Maslovsky, M. E Mauel, and J Waksman. Excitation of the centrifugally driven interchange instability in a plasma confined by a magnetic dipole. *Phys. Plasmas*, 12:055703, Jan 2005.

[59] E Lorenz. Deterministic nonperiodic flow. *J. Atmos. Sci.*, 20:130–141, Jan 1963.

[60] P Manz, M Ramisch, and U Stroth. Experimental estimation of the dual cascade in two-dimensional drift-wave turbulence. *Plasma Phys. Control. Fusion*, 51(3):035008, Dec 2008.

[61] P Manz, M Ramisch, U Stroth, V Naulin, and B D Scott. Bispectral experimental estimation of the nonlinear energy transfer in two-dimensional plasma turbulence. *Plasma Phys. Control. Fusion*, 50:035008, Feb 2008.

[62] D Maslovsky. Suppression of nonlinear frequency sweeping of resonant interchange modes in a magnetic dipole with applied radio frequency fields. *Ph.D Thesis*, Apr 2003.

[63] D Maslovsky, B Levitt, and M Mauel. Observation of nonlinear frequency-sweeping suppression with rf diffusion. *Phys. Rev. Lett.*, 90:185001, Jan 2003.

[64] D Maslovsky, B Levitt, and M Mauel. Suppression of nonlinear frequency-sweeping of resonant interchange modes in a magnetic dipole with applied radio frequency fields. *Phys. Plasmas*, 10(5):1549–1555, Jan 2003.

[65] D Maslovsky, M E Mauel, and B Levitt. Numerical simulation of phase-space flows in the collisionlessterrella experiment. *IEEE Trans. Plasma Sci.*, 30(1):8–9, Jan 2002.

[66] M E Mauel. Laboratory observations of wave-induced radial transport within an "artificial radiation belt". *Journal de Physique, IV*, 7(C4):307–318, Sep 1997.

[67] C Nardone. Multichannel fluctuation data analysis by the singular value decomposition method. application to mhd modes in jet. *Plasma Phys. Control. Fusion*, 34(9):1447–1455, Jan 1992.

[68] HL Pecseli and J Trulsen. On the interpretation of experimental methods for investigating nonlinear wave phenomena. *Plasma Phys. Controlled Fusion*, 35:1701–1715, 1993.

[69] F. M Poli, S Brunner, A Diallo, A Fasoli, I Furno, B Labit, S. H Müller, G Plyushchev, and M Podestà. Experimental characterization of drift-interchange instabilities in a simple toroidal plasma. *Phys. Plasmas*, 13:102104, Jan 2006.

[70] F. M Poli, M Podestà, and A Fasoli. Development of electrostatic turbulence from drift-interchange instabilities in a toroidal plasma. *Phys. Plasmas*, 14:052311, Jan 2007.

[71] C Ritz and E Powers. Estimation of nonlinear transfer functions for fully developed turbulence. *Physica*, 20D:320–334, Jan 1986.

[72] C Ritz, E Powers, and R Bengtson. Experimental measurement of three-wave coupling and energy cascading. *Physics of Fluids B: Plasma Physics*, 1(1):153–163, Jan 1989.

[73] MK Rivera, WB Daniel, SY Chen, and RE Ecke. Energy and enstrophy transfer in decaying two-dimensional turbulence. *Phys. Rev. Lett.*, 90(10):104502, Jan 2003.

[74] M Rosenbluth and C Longmire. Stability of plasmas confined by magnetic fields. *Ann. Phys.*, 1:120–140, Jan 1957.

[75] J Roth, W Krawczonek, E Powers, J Hong, and Y Kim. Inward transport of a toroidally confined plasma subject to strong radial electric fields. *Phys. Rev. Lett.*, 40(22):1450–1453, Jan 1978.

[76] K Rypdal. Onset of turbulence and profile resilience in the helimak configuration. *Phys. Rev. Lett.*, 94:225002, Jun 2005.

[77] K Rypdal and O. E Garcia. Reduced lorenz models for anomalous transport and profile resilience. *Phys. Plasmas*, 14:022101, Jan 2007.

[78] D Ryutov, P Helander, and R Cohen. On the possibility of inducing strong plasma convection in the divertor of mast. *Plasma Phys. Control. Fusion*, 43:1399–1423, Jan 2001.

[79] M. G Shats, H Xia, and H Punzmann. Spectral condensation of turbulence in plasmas and fluids and its role in low-to-high phase transitions in toroidal plasma. *Phys. Rev. E*, 71:046409, Apr 2005.

[80] L Sorriso-Valvo, R Marino, V Carbone, A Noullez, F Lepreti, P Veltri, R Bruno, B Bavassano, and E Pietropaolo. Observation of inertial energy cascade in interplanetary space plasma. *Phys. Rev. Lett.*, 99:115001, Sep 2007.

[81] Edward A Spiegel. Chaos and intermittency in the solar cycle. *Space Science Reviews*, pages 1–27, Dec 2008.

[82] X Sun, H Zhang, and L Ni. Efficient tridiagonal solvers on multicomputers. *IEEE Trans. Comput.*, 41(3):286–296, Jan 1992.

[83] P Tabeling. Two-dimensional turbulence: a physicist approach. *Physics Reports*, 362:1–62, Jan 2002.

[84] PW Terry. Inverse energy transfer by near-resonant interactions with a damped-wave spectrum. *Phys. Rev. Lett.*, 93:235004, 2004.

[85] G. R Tynan, M. J Burin, C Holland, G Antar, N Crocker, and P. H Diamond. Radially sheared azimuthal flows and turbulent transport in a cylindrical plasma. *Phys. Plasmas*, 11(11):5195, Jan 2004.

[86] GR Tynan, RA Moyer, MJ Burin, and C Holland. On the nonlinear turbulent dynamics of shear-flow decorrelation and zonal flow generation. *Phys. Plasmas*, 8:2691, 2001.

[87] M Wakatani and A Hasegawa. A collisional drift wave description of plasma edge turbulence. *Physics of Fluids*, 27(3):611–618, Jan 1984.

[88] H Xia, H Punzmann, G Falkovich, and M. G Shats. Turbulence-condensate interaction in two dimensions. *Phys. Rev. Lett.*, 101:194504, Nov 2008.

[89] H Xia and M Shats. Inverse energy cascade correlated with turbulent-structure generation in toroidal plasma. *Phys. Rev. Lett.*, 91:155001, Jan 2003.

[90] H Xia and M. G Shats. Spectral energy transfer and generation of turbulent structures in toroidal plasma. *Phys. Plasmas*, 11(2):561–571, Jan 2004.

[91] G. S Xu, B. N Wan, W Zhang, Q. W Yang, L Wang, and Y. Z Wen. Multiscale coherent structures in tokamak plasma turbulence. *Phys. Plasmas*, 13:102509, Jan 2006.

[92] T Yamada, S Itoh, T Maruta, N Kasuya, and Y Nagashima .... Anatomy of plasma turbulence. *Nat. Phys.*, 4:721–725, Jan 2008.

[93] S Zalesak. High order "zip" differencing of convective terms. *J. Comp. Phys.*, 40:497–508, Jan 1980.

[94] S T Zalesak. Fully multidimensional flux-corrected transport algorithms for fluids. *J. Comp. Phys.*, 31:335–362, Jan 1979.

[95] T Živković and K Rypdal. Experimental evidence of low-dimensional chaotic convection dynamics in a toroidal magnetized plasma. *Phys. Rev. E*, 77:037401, Mar 2008.

[96] S J Zweben, J A Boedo, O Grulke, C Hidalgo, B Labombard, R J Maqueda, P Scarin, and J L Terry. Edge turbulence measurements in toroidal fusion devices. *Plasma Phys. Control. Fusion*, 49:S1–S23, Jun 2007.

[97] S.J Zweben, R.J Maqueda, D.P Stotler, A Keesee, J Boedo, C.E Bush, S.M Kaye, B Leblanc, J.L Lowrance, V.J Mastrocola, R Maingi, N Nishino, G Renda, D.W Swain, J.B Wilgen, and The Nstx Team. High-speed imaging of edge turbulence in nstx. *Nucl. Fusion*, 44:134–153, Dec 2003.